Multi-Section InP-on-Silicon DFB Laser Diodes: Optimisations and Applications

InP-op-silicium DFB-laserdiodes met meerdere secties: optimalisaties en toepassingen

Mahmoud Shahin

UNIVERSITEIT
GENT

Universiteit Gent
Faculteit Ingenieurswetenschappen en Architectuur
Vakgroep Informatietechnologie

Promotoren:
prof. dr. ir. Geert Morthier
prof. dr. ir. Günther Roelkens

Examencommissie:

prof. dr. ir. Filip De Turck (voorzitter)	Universiteit Gent
prof. dr. ir. Geert Morthier (promotor)	Universiteit Gent
prof. dr. ir. Günther Roelkens (promotor)	Universiteit Gent
prof. dr. ir. Dries Van Thourhout (secretaris)	Universiteit Gent
prof. dr. ir. Xin Yin	Universiteit Gent
prof. dr. ir. Geert Van Steenberge	Universiteit Gent
prof. dr. ir. Guy Verschaffelt	Vrije Universiteit Brussel
prof. dr. ir. Jos van der Tol	Technische Universiteit Eindhoven

Universiteit Gent
Faculteit Ingenieurswetenschappen en Architectuur

Vakgroep Informatietechnologie
Technologiepark Zwijnaarde 126, 9052 Gent, België

Acknowledgment

This four-year-long PhD was such a unique and crazy adventure. That is right, crazy is my way of describing it. Aside from gaining significant knowledge about photonics, I learned a great deal about life as well, from everyone I met in and out of the photonics research group of Ghent University. I have had many interesting discussions over lunch or coffee, which brought yet another dimension to the way I view the world as an individual. I met a collection of people with unique personalities and talents, and among those, I made many life-time friends.

As you might expect, I will start by acknowledging my professors. The guidance of my professors was crucial for the success of this work. I had the pleasure of working with two world-renowned researchers in their fields. My main supervisor, Geert, was always available for consultation, and we worked together as a team. We have exchanged more than a thousand and five hundred emails and probably met more than a hundred times to discuss our progress. His support and contribution from my first days as a novice researcher until my thesis defense are crystal clear. I did not exchange as many emails or met as many times with my co-supervisor, Gunther, because that would have been crazy. However, his suggestions were always useful, and his feedback for all the manuscripts we wrote was critical for the quality of the final output. Thank you both for supporting and believing in me. I would also like to express my gratitude to the jury members of this thesis for providing valuable comments to improve the manuscript.

I would like to extend a word of gratitude for other researchers in the photonics research group, who in one way or another have positively influenced my progress. I would like to mention a few of them here. In the first period of my PhD, I obtained many skills and learned many techniques on laser processing and characterization by closely following *Amin*. I also received a lot of support from other researchers working on III-V/Si. *Sören* offered his advice on several occasions, as well as my colleagues *Jing* and *Sulakshna*, and others who patiently responded to my many questions in and out of the cleanroom.

Additionally, I would like to acknowledge the support of the cleanroom staff, who were always ready to assist. *Steven* was always eager to demystify the different sophisticated systems in the cleanroom, while *Muhammad* showed me many practical fabrication tips that proved indispensable in the fabrication of laser devices. Finally, *Liesbet* helped me several times with the use and interpretation of SEM/FIB measurements. It remains a mystery how many Acetone-IPA bottles did I fill during my time in the cleanroom.

I would also like to acknowledge the efforts of other technical and administrative staff in the group, *Ilse*, *Kristien*, and *Jasper*. Furthermore, I received ample support from the IDLab team, mainly from *Joris VKB*, during my complex high-speed modulation experiments. Last but not least, I worked for one year side by side with my colleague *Ma Keqi* on self-pulsation lasers during what was possibly the most enjoyable period of my PhD journey. Also, I would like to share a word of gratitude for all other collaborators and researchers who are not mentioned here for their support and encouragement.

I spent the funniest moments with my office mates, *Xiaomin*, thank you for lending me your nail clipper every day. I bet many readers already know the story behind that. Seriously now, I had many nice conversations with you. *Irfan*, thanks to you, I discovered a new dimension of humor. *Nicolas*, though we did not spend a lot of time together, I enjoyed all of our high-speed modulation experiments (i.e. agario). For once, please come to the office, and hopefully to my reception too. *Sören*, thank you for your whiteboard workshops, language tips, and funny stories! Thank you *Haolan* and *Luis* for being part of my experience!

I bet you are waiting to read your name among these lines. Please don't be disappointed if it wasn't there. You are special to me in some way if you are reading this. Anyway, I would like to mention a few more people who made a difference to me as a person. *Kristof* is the friendliest and funniest Belgian *man* I have ever met. I was also happy to meet the most original person *Nuria*. It's also cool to click with some unexpectedly crazy people like *Anita*. Since I am talking about people who made a difference to my PhD experience, I need to mention *Javad,* who provided me with a lot of support and helped in many ways during the last part of my PhD. He is one proper gentleman. I could spend hours discussing random stuff with *Saurav*, the most entertaining person in the group. Oh, sorry, is that in the trailer too?

Friday evenings weren't going to be as good without my best friends. I consider myself lucky to have made some lifetime friends here. I had the time

of my life with *Alejandro* and *Sanja*. It goes far beyond this text to describe this triangle, and given that I don't have space, I simply won't. I also had the most thought-provoking conversations with *Alessio* and the best arguments with *Margherita*. You guys are impossible to forget. Speaking about best times, I had the best coffee breaks with the one and only of a kind *Nina*. Needless to say, I had the strangest yet most enjoyable conversations with *Alexandros*. It was interesting to view life from your perspective, and you know what I'm talking about. I can't forget *Andrew* with whom we spent the best time in the middle of the African jungles, but also in the middle of the Belgian bars (that does sound kind of alcoholic though).

I got married during these four years, and my wife was the best thing that ever happened to me. *Savvinaki-mou* is my lucky charm and the secret to my happiness. Therefore, I would like to dedicate this work to her. Σ'αγαπώ. I also would like to acknowledge my parents-in-law, *Giorgos* and *Daisy* for their support, and to my brothers- and sister-in-law *Panagiotis*, *Stamatis*, and *Iw*.

Before finishing, I would like to still acknowledge the support of a few more people: *Abdul*, *Anatoly, Banafsheh, Clemens*, *Daria*, *Joanna, Jeroen*, *Mia*, *Nesreen, Omar*, and *Tanja.* If I forgot to mention someone, it's because I found this the most difficult part to write. I probably need another book telling the many stories behind my PhD. So if you are part of the story, and especially if you are reading this during my PhD presentation, then you probably need to pay more attention to the presentation? Nonetheless, I would like to thank you for all the support and contribution, no matter how small it was. Some people just smiled at me at the kitchen, which was sometimes enough to cheer me up. As for my family, I received a great deal of support from them, but I would rather acknowledge them in the Arabic script below.

هذا الكتاب اهداء مع جزيل الشكر والامتنان لوالديّ الغاليان مروان وفادية لدعمهم اللامحدود. أدامكم الله ذخراً لنا. كما واتوجه بالشكر لأختي هدى ولإخوتي محمد وراشد. الشكر كذلك لعائلتي الممتدة, الاعمام والعمات والاخوال والخالات وابنائهم وبناتهم والأجداد والجدات, وجميع من كان له الأثر الإيجابي علي من عائلتي واصدقائي. هذا الكتاب اهداء ايضاً للصغار تاليا ومروان, ربما يأتي يوم وتقرؤون هذه الكلمات وتكون لها الأثر الإيجابي عليكم لنرى منكم عظماء المستقبل.

December 2019, Ghent
Mahmoud Shahin

ديسمبر 2019، غنت
محمود شاهين

Table of Contents

List of Acronyms

A

AlSb	Aluminum-Antimony
AR	Anti-Reflective
Au	Aurum (Gold)
AWG	Arbitrary Waveform Generator

B

BER	Bit Error Rate
BHF	Buffered Hydrofluoric acid

C

CdO	Cadmium-Oxide
CW	Continuous-Wave

D

DBR	Distributed Bragg Reflector
DC	Direct Current
DFB	Distributed Feedback
DR	Distributed Reflector
DSF	Dispersion Shifted Fiber
DVS-BCB	Divinylsiloxane-Bis-Benzocyclobutene
DWDM	Dense Wavelength Division Multiplexing

E

EAM	Electro-Absorption Modulation
EDFA	Erbium-Doped-Fiber-Amplifier
EML	Externally-Modulated Laser
EOM	Electro-Optic Modulators
ESA	Electrical Spectrum Analyzer

F

FDTD	Finite-Difference Time-Domain

FDTW   Finite-Difference
Travelling-Wave
FEC   Forward Error Correction
FIB   Focused Ion Beam
FSR   Free Spectral Range

G

GaInNAs   Gallium-Indium-Nitride-
Arsenide
Ge   Germanium
GaAs   Gallium-Arsenide
GS   Ground-Signal
GSG   Ground-Signal-Ground

H

H_2O Dihydrogen Monoxide
(Water)
H2O2   Hydrogen Peroxide
H_2SO_4 Sulphuric acid
HCl   Hydrochloric acid
HD   Hard Decision
HeNe   Helium-Neon

I

ICP	Inductively Coupled Plasma
IEEE	Institute of Electrical and Electronics Engineers
InP	Indium-Phosphide
InGaAsP	Indium-Gallium-Arsenide-Phosphide
InAlGaAs	Indium-Gallium-Aluminum-Arsenide

L

LED	Light-Emitting Diode

M

MZM	Mach-Zehnder Modulator
MQW	Multi Quantum Well

N

NRZ-OOK	Non-Return-to-Zero On-Off-Keying
Ni	Nickel

NZ-DSF   Non-Zero Dispersion-
Shifted Fiber

P

PAM-4   Four-level Pulse
Amplitude Modulation
PPR   Photon-Photon
Resonance
PRBS   Pseudorandom Binary
Sequence

Q

QAM   Quadrature Amplitude
Modulation
QPSK   Quadrature Phase-Shift
Keying

R

RIE   Reactive Ion Etching
RF   Radio Frequency

S

SCH	Separate Confinement Heterostructure
SOI	Silicon-On-Insulator
SOA	Semiconductor Optical Amplifier
Si	Silicon
SMSR	Side-Mode Suppression-Ratio
SiN	Silicon Nitride
SEM	Scanning Electron Microscope

V

VCSEL	Vertical-Cavity Surface-Emitting Laser
VNA	Vector Network Analyzer

W

WDM	Wavelength-Division Multiplexing

Z

ZnO	Zinc-Oxide

Nederlandse Samenvatting

De voorbije twee decennia hebben we een ongeziene groei gekend van de vraag naar telecommunicatie, iets waartoe vroeger enkel een elite toegang had.Oorspronkelijk werden koperkabels gebruikt voor telecommunicatie. Deze werden echter snel vervangen door optische vezels, die een veel grotere bandbreedte toelaten en veel lagere propagatieverliezen hebben. Optische vezels worden nu vooral gebruikt voor lange-afstandscommunicatie (vanaf enkele tientallen km), maar ze worden alsmaar meer ook voor kortere afstanden (enkele honderden meters) overwogen. Wetenschappers hopen dat optische interconnecties ooit zelfs op chipschaal zullen gebruikt worden, maar dit blijft een grote uitdaging.

Optische interconnecties in datacenters zijn een goed voorbeeld van korte-afstandscommunicatie. Bedrijven zoals Facebook en Google moeten heel wat data verwerken in hun datacenters. Dit vereist communicatie aan hoge snelheid tussen de servers, gebruikmakend van hoge-snelheidslaserdiodes, modulatoren en fotodetectoren. Geaggregeerde datadebieten tot 800 Gbit/s of 1.6 Tbit/s per transceiver worden verwacht de standaard te worden in de nabije toekomst. Naast de bandbreedtevereisten, dienen de optische-transmissiesystemen ook een zo laag mogelijk energieverbruik te hebben.

Dit werk richt zich op het verbeteren van de performantie van de laserdiodes, één van de belangrijkste componenten in elk optisch communicatiesysteem en dus ook van de optische interconnecties in datacenters. Het doel is om compacte laserdiodes te demonsteren met hoge modulatiebandbreedte en laag vermogenverbruik.

Momenteel is er heel wat interesse in siliciumfotonica, o.a. voor de realisatie van fotonisch geïntegreerde circuiten met dewelke diverse functies kunnen uitgevoerd worden. De mogelijkheid van volumeproductie aan lage kostprijs maakt dit platform heel aantrekkelijk. Siliciumfotonica biedt tevens de mogelijkheid tot heel dichte integratie, alsmede om de volwassen fabricatietechnologie van de CMOS-elektronica te gebruiken.

Aan de andere kant heeft silicium evenwel het nadeel dat het niet geschikt is voor de realisatie van lichtbronnen, door zijn indirecte bandstructuur. Daarom moet het gecombineerd worden met III-V epitaxiale lagen. Dit kan op verschillende manieren, zoals flip-chip integratie, hetero-epitaxie en heterogene integratie (op basis van een soort hechting). Het III-V-op-silicium combineert de eerder vermelde voordelen van silicium met efficiente lichtbronnen in het III-V-membraan. De methode die in dit doctoraat gebruikt wordt voor de heterogene integratie van III-V membranen op silicium golfgeleiders is adhesieve hechting, en een SEM-foto van de doorsnede van de resulterende laser diode wordt gegeven in Fig. 1.
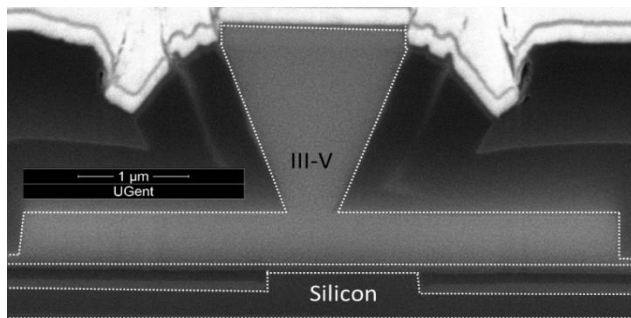

Figure 1: SEM-afbeelding van de doorsnede van een gefabriceerde III-V-op-silicium laserdiode.

De laser die we gekozen hebben om de verschillende doeleinden te verwezenlijken is de DFB (distributed feedback) laserdiode. Het is de lichtbron die reeds lang de voorkeur geniet voor optische communicatie, vanwege de stabiele monomodale werking en de hoge zijmode-onderdrukking. De lasers die in dit werk gedemonstreerd worden zijn: (1) zelf-pulserende lasers, (2) bandbreedteverhoogde lasers, (3) lasers met lage drempelstroom, (4) electro-absorptie-gemoduleerde lasers, en (5) compacte lasers.

De zelf-pulserende DFB laserdiode

De component die het eerst gedemonstreerd wordt in dit werk is de zelf-pulserende DFB laserdiode. De laser bestaat uit twee secties die van een verschillende stroom worden voorzien. Dit resulteert in twee laserlijnen waardoor de totale intensiteit op periodieke manier in de tijd varieert met de verschilfrequentie. Afstembare, hoge repetitiefrequenties kunnen op die manier bekomen worden, zoals te zien is in Fig. 2. Deze component kan gebruikt worden voor de generatie van optische microgolfdragers, welke op hun beurt nuttig zijn in radio-over-vezel-toepassingen.
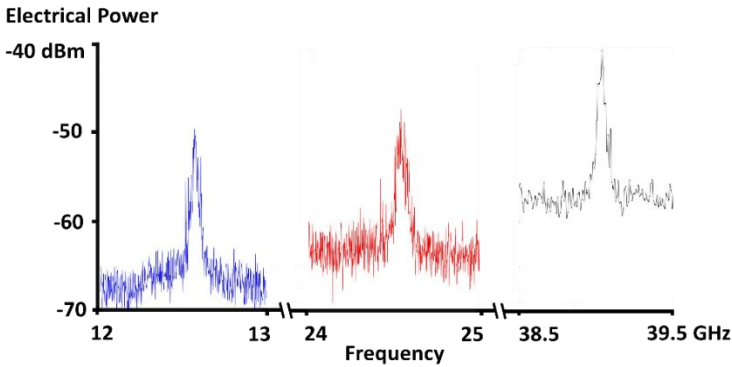
Figure 2: RF spectra van een zelf-pulserende laser met repetitiefrequenties van 12.5, 24.5 en 39 GHz.
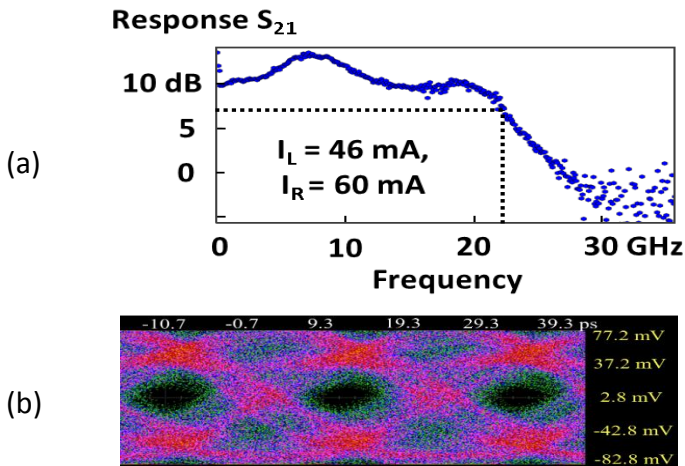

Figure 3: Een tweede resonantiepiek verschijnt in het modulatie-antwoord tengevolge van de excitatie van een zijmode (a). Dit leidt tot een hoge modulatiebandbreedte en snelheid, zoals te zien in het oogdiagram voor 45 Gb/s modulatie in (**b**).

De bandbreedteverhoogde DFB laser diode

Gebruikmakend van een soortgelijke structuur als bij de zelf-pulserende lasers, demonstreren we DFB lasers met verhoogde bandbreedte. Indien de twee lasersecties van een iets andere dc-stroom voorzien worden, verschijnt in het modulatie-antwoord een tweede piek, bovenop de resonantiepiek van de relaxatie-oscillaties. Dit is te zien in Fig. 3 (a), die het modulatie-antwoord toont als functie van de modulatiefrequentie. De tweede piek verhoogt de modulatiebandbreedte, en laat modulatie bij hogere bitsnelheden toe, wanneer één laser sectie wordt gemoduleerd. Voor het meten van het oogdiagram in Fig. 3 (b) werd de laser gemoduleerd aan 45 Gbit/s.

Een DFB laserdiode met lage drempelstroom

Gebruikmakend van de in twee secties verdeelde laserdiode demonstreren we ook DFB laserdiodes met lage drempelstroom. Daartoe wordt slechts één van de twee lasersecties gebiased en wordt de andere lasersectie gebruikt als reflector en voor de koeling. We rapporteren compacte lasers met een lage drempelstroom (van 4.5 mA, zie Fig. 4) en derhalve laag energieverbruik, terwijl een modulatiebandbreedte kan behouden blijven die gelijkaardig is aan deze van de standaard laser met één ekele sectie.
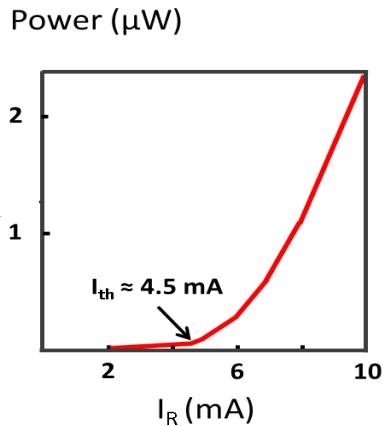
Power (µW)

Figure 4: Optisch vermogen versus geïnjecteerde stroom voor een DFB laserdiode met een lage drempelstroom van 4.5 mA.

Electroabsorptie-gemoduleerde DFB laserdiodes

De volgende component is een electroabsorptie-gemoduleerde DFB laser, met hoge modulatiebandbreedte. De taper die normaal gebruikt wordt om het licht te koppelen tussen het III-V membraan en de silicium golfgeleider wordt hier gebruikt voor de electroabsorptiemodulatie. We proberen de maximale snelheid van de modulatie te verhogen door de modulator te verkleinen en zo de capaciteit en de RC-constante te verkleinen. Dit wordt verwezenlijkt door het splitsen van de taper in twee secties, en slechts de eerste sectie te gebruiken als electroabsorptiemodulator. Gezien op die manier de oppervlakte van de modulator gereduceerd wordt, leidt dit tot een toename van de modulatiebandbreedte. Het oogdiagram in Fig. 5 illustreert de toegenomen maximale bitrate bij dergelijke modulatie; het is voor datatransmissie aan 80 Gbit/s.
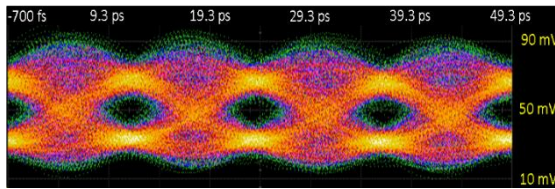
Figure 5: Oogdiagram voor datatransmissie aan 80 Gbit/s in een zgn. rug-aan-rug configuratie.

Compacte DFB laserdiodes

De laatste component is een compacte DFB laserdiode. Hier is het doel om de laser zo klein mogelijk te maken zodat ook zijn energieverbruik aanzienlijk daalt. We stellen een nieuw ontwerp voor met een korte taper, waarvan de koppelingsefficientie door middel van simulaties berekend wordt. Ook de uitdagingen en beperkingen van de fabricatie worden besproken en tenslotte worden ook de karakteristieken getoond van gefabriceerde componenten.

Figure 6: Traditioneel (lang) ontwerp gebruikt voor de taper **(a)** en in het doctoraat voorgestelde kort taper ontwerp **(b)**.

English Summary

The past two decades have witnessed unprecedented growth and demand for telecommunication, something that only the elite had access to in the past. Originally, copper cable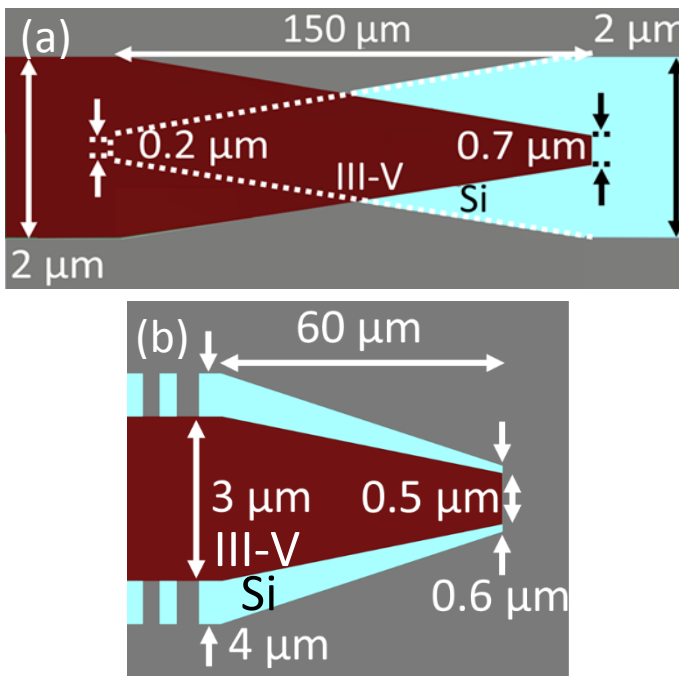s were used for telecommunication. These were quickly replaced by optical fibers that have many advantages in terms of bandwidth and loss. Optical fibers are used nowadays for long-distance communication (a few tens of km), but are quickly being introduced also for shorter distances (a few hundreds of meters). Although challenging, scientists hope that optical interconnects can penetrate even to chip level communication.

Optical interconnects in data centers are a good example of short-reach communication. Companies like Facebook and Google need to process a lot of data in their data centers. This requires high-speed communication between the servers, using high-speed lasers, modulators, and photodetectors. Aggregate data rates from transceivers as high as 800 Gbps or 1.6 Tbps are expected to become a standard soon. In addition to the bandwidth requirements, these optical systems should have as low power consumption as possible.

This work focuses on improving the performance of laser diodes, an important component of any optical communication system in data centers. The focus is to demonstrate laser diodes with high modulation bandwidth, small footprint, and low power consumption.

Nowadays, there is a lot of interest in silicon photonics to create photonic integrated circuits, in which many functionalities can be realized. Large volume production at low cost makes this platform very attractive for photonics applications. Silicon photonics also offers the possibility for dense integration, as well as the opportunity to use the mature CMOS electronics fabrication technology. On the other hand, silicon has the disadvantage of being an inefficient light source, due to its indirect bandgap. Therefore it has to be combined with III-V epitaxial layers. This can be done by various techniques such a flip-chip integration, hetero-epitaxy and heterogeneous integration. Integration of III-V on silicon combines the aforementioned

advantages of silicon, as well as the advantage of III-V semiconductors as efficient light sources. The method used in this work for the heterogeneous integration of III-V membranes on silicon waveguides is adhesive bonding, and a cross section of the resulting device is shown in Fig. 1.
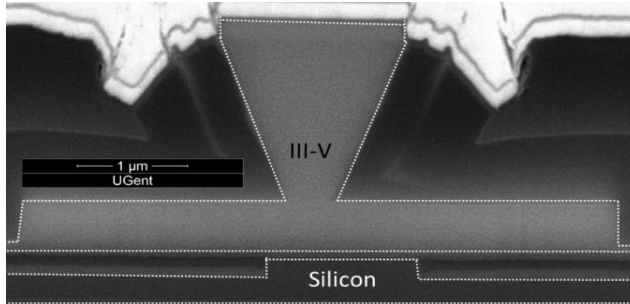

Figure 1: SEM image of a cross-section of a fabricated III-V-on-silicon laser diode

The distributed feedback laser diode is the laser of choice in our work to demonstrate lasers for different purposes. It is also the preferred optical source in optical communication due to its stable single-mode behavior, and high side-mode suppression ratio. The lasers demonstrated throughout this work are: (1) self-pulsating lasers, (2) bandwidth enhanced lasers, (3) low-threshold lasers, (4) electro-absorption modulated lasers, and (5) compact lasers.

Self-pulsating DFB laser diode

The first demonstrated device in this work is the self-pulsating DFB laser diode. The laser consists of two sections that are biased at different bias currents, resulting in two beating laser lines. High and tunable repetition frequencies were obtained, as shown by the RF spectra in Fig. 2. This device can be used for the generation of an optical microwave carrier, which is suited for radio-over-fiber applications.
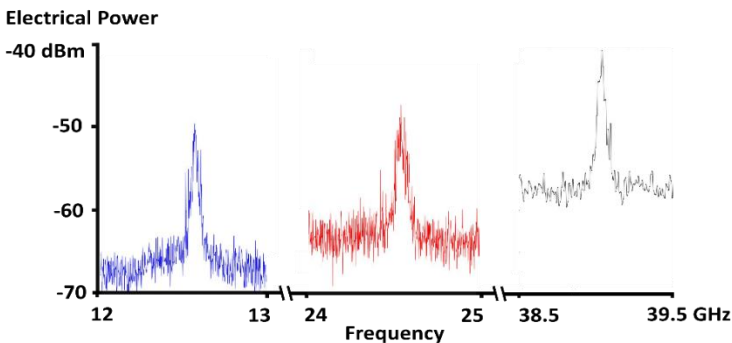

Figure 2: RF spectra of a self-pulsating laser with repetition frequencies of 12.5, 24.5 and 39 GHz.
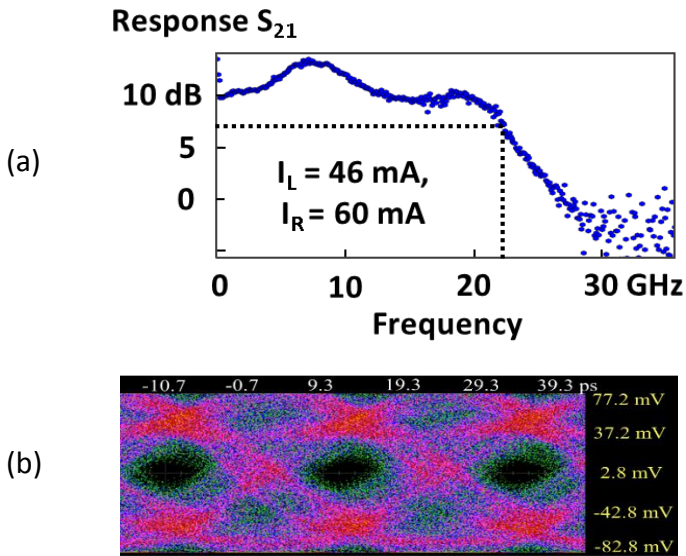
Figure 3: (a) Modulation response in which a second resonance peak appears due to the beating between the two laser lines of the two sections. (b) Eye diagram at 45 Gbps for the laser with modulation response given in (a).

Bandwidth-enhanced DFB laser diode

Using a configuration similar to the self-pulsating lasers, we demonstrate bandwidth enhanced DFB lasers. By biasing the two laser sections at certain bias currents, a second resonance peak appears in the modulation response, in addition to the relaxation oscillation frequency peak, as shown in Fig. 3 (a). This extends the modulation bandwidth, leading to higher modulation speed when directly modulating one laser section, as shown by the eye diagram at 45 Gb/s in Fig. 3 (b).

Low-threshold DFB laser diode

Using the two-section configuration, we demonstrate low-threshold DFB laser diodes. This is done by biasing only one of the two laser sections, and using the second section as a reflector and heat sink. We report compact lasers with low threshold current (Fig. 4) and therefore lower power consumption while maintaining modulation bandwidths similar to those of the standard single-section laser.

Power (μW)

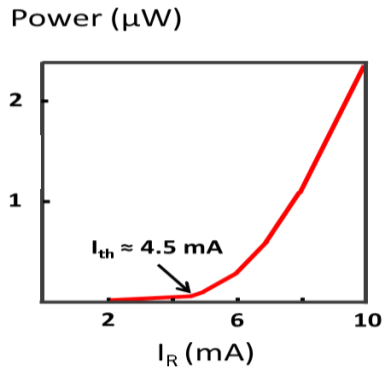**Figure 4:** Optical power vs. injected current for a low threshold current laser

Electro-absorption modulated DFB laser diode

The next device is an electro-absorption modulated DFB laser, with high modulation bandwidth. The taper used to couple light from the III-V to the silicon waveguide is used here for electro-absorption modulation. We aim to improve the high-speed performance by shrinking the modulator to reduce the capacitance and therefore the RC constant. This is done by separating the taper structure into two sections and using one of them as an electro-absorption modulator. Since the area of the modulator is reduced, the modulation bandwidth increases. The data transmission experiment shows an improvement in modulation speed as shown in Fig. 5.
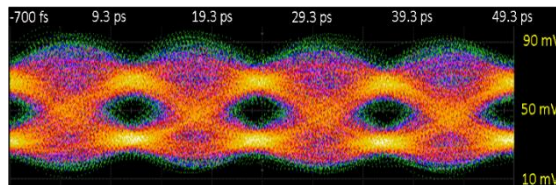
Figure 5: Eye diagram for the data transmission at 80 Gbps in back-to-back configuration

Compact DFB laser diode

The final device is a compact DFB laser diode. The aim is to shrink the laser as much as possible, such that the power consumption is reduced. We propose a new design for a short taper structure, and show its coupling efficiency through simulations. The design of the proposed device, in comparison to the previous one, is shown in Fig. 6 (a, b). This is followed by outlining the fabrication challenges and limitations. Finally, the characteristics of the fabricated device with different taper parameters are shown.
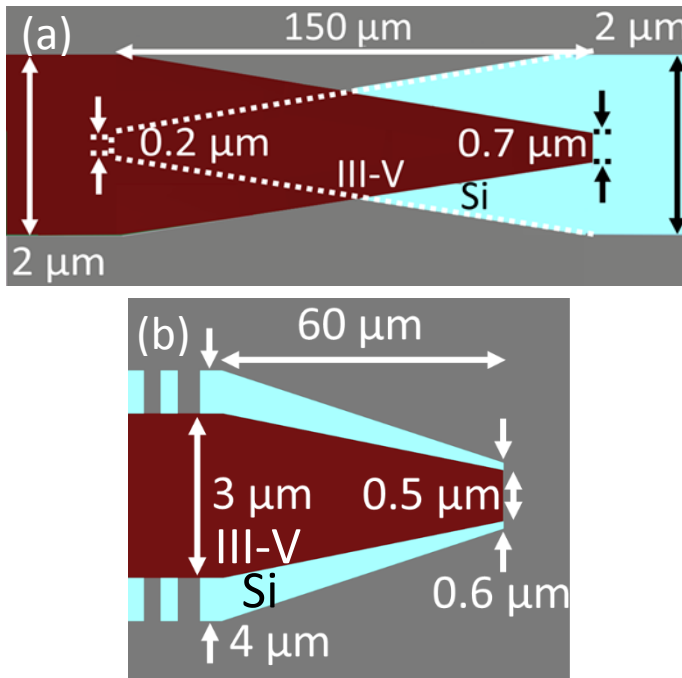
Figure 6: Previously used (long) taper design **(a)** and proposed (short) taper design **(b)**.

1

Introduction

Contents

1.1   Optical interconnects

Today, we are living in a rapidly changing period of humanity. The demand for better technologies to improve human life is exploding. Not so long ago, it was only the elite that had access to a telegraph for telecommunication, which required the knowledge of Morse code. Nowadays, almost everybody has access to inexpensive means of communication, allowing video calls across the oceans. As these technologies become part of our lives, it is no surprise that the amount of data traffic has exploded.

Until recently, telecommunication used copper cables. Nowadays, optical fibers have replaced copper cables for long distance communication. This is because of the many advantages, such as higher bandwidth, lower loss, and immunity to electromagnetic interference.

An example of short reach communication is the interconnection in data centers, like the one in Fig. 1.1 [1]. Such data centers require interconnects on

length scales of a few kilometers. Companies that store and handle huge amounts of data, such as Google or Facebook, need to spend billions of dollars to constantly maintain and improve their data center infrastructure.

Figure 1.1: Data center requiring interconnects in length scales of a few kilometers (figure from [1]).

Most data centers are already using optical fibers for communication between different servers, for their aforementioned advantages. There are a few parameters that describe the performance and determine the quality of an optical system. For example, the modulation bandwidth, which determines how much data can be sent over an optical link, is one of the most important parameters in an optical system. It is limited by the components in the system, such as the transmitter, the receiver, and the fiber infrastructure. Other important parameters are the power consumption and the footprint of these systems.
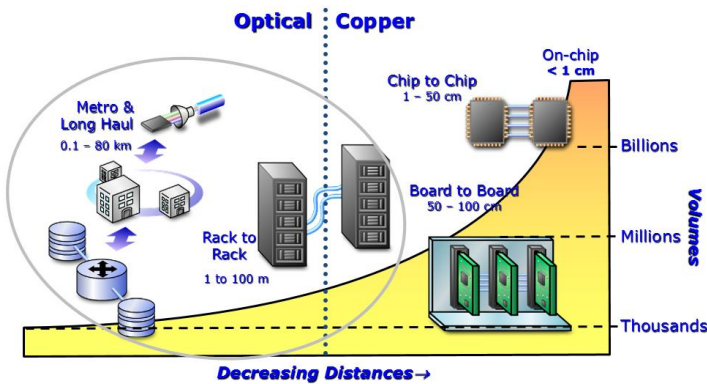

Figure 1.2: Roadmap showing how optical interconnects are replacing copper interconnects over time (figure from [2]).

Scientists hope that in the future optical interconnects can replace copper-based communication even on chip level. While this is not impossible, a lot of work still needs to be done to achieve this. For the moment, work is ongoing to improve the performance of the components on rack-to-rack and board-to-board level, as indicated in Fig. 1.2 [2].

The main wavelengths for optical communication in data centers are 850, 1310, and 1550 nm. Each wavelength is useful for a specific application. The reason why these wavelengths are chosen for optical communication is related to the loss and dispersion of the optical mode in the fiber material (SiO_2). On one hand, in the 1550 nm window, the optical loss is the lowest, as shown in Fig. 1.3. When light travels over long distances, this parameter becomes important. Therefore, for long distance communication, 1550 nm is the wavelength of choice.
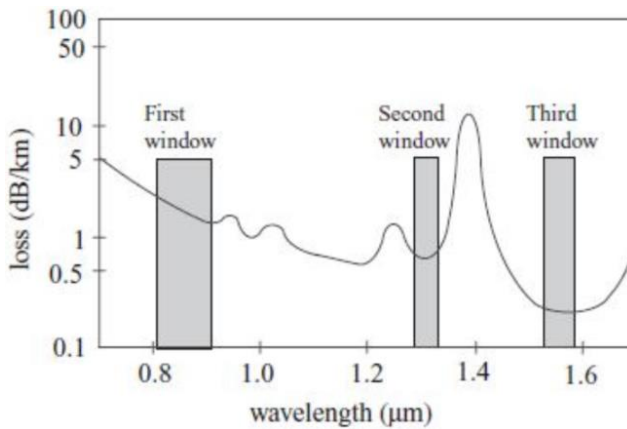
Figure 1.3: Optical loss in fibers for different wavelength windows, showing the lowest losses for the 1550 nm window (figure from [3]).

The 1310 nm window on the other hand is where normal single mode fibers exhibit zero dispersion, as shown in Fig. 1.4. Dispersion in optical fibers results in the spread of light pulses in time due to the different wavelengths traveling with different phase velocities in the fiber. The effect of dispersion becomes significant for long distances and high bitrates, when consecutive pulses can completely overlap. The attenuation is however more than that of the 1550 nm window. Therefore, this wavelength is preferred for short distances. It is also possible to overcome the problem of dispersion in the 1550 nm window using dispersion shifted fibers (DSFs). Such fibers can shift the zero-dispersion point from 1310 nm to the 1550 nm, as shown in Fig. 1.4.

Finally, the 850 nm window is the wavelength range of choice for the operation of multimode fiber optical communication, using light-emitting diodes (LEDs) and vertical-cavity surface-emitting lasers (VCSELs) as light sources. Since multi-mode fibers have larger core size, they can support more than one propagation mode. This results in modal dispersion, a distortion mechanism that occurs in multi-mode fibers due to the different propagation velocity of each

mode. Therefore, the bandwidth-distance product limit is lower, compared to single-mode fibers [4].

Dispersion coefficient ps/nm.km

Figure 1.4: Dispersion in normal fibers versus that in dispersion shifted fibers, where the zero dispersion point was shifted from the 1310 nm to the 1550 nm window.

To push the modulation speed higher, the Institute of Electrical and Electronics Engineers (IEEE) proposes certain Ether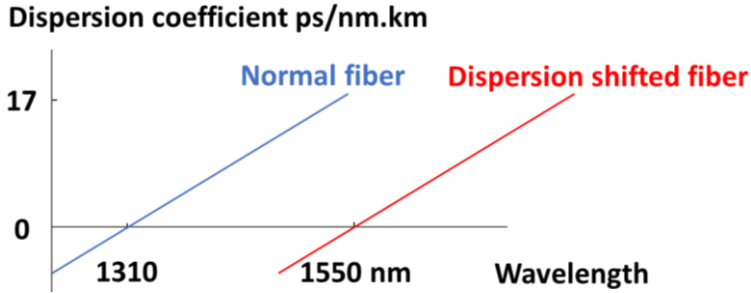net standards for optical fiber communication. Some important standards for single-mode fibers are summarized in Table 1.1. The different signals are put on different wavelengths and then multiplexed onto a single optical fiber. This is called wavelength division multiplexing (WDM). Furthermore, data rates as high as 800 Gbps and 1.6 Tbps are also expected to become IEEE standards after 2020 [5].

Table 1.1: Few IEEE Ethernet standards for single-mode fibers

Ethernet standard	Rate	Distance
IEEE 802.3bm (100GBASE-LR4)	4×25 Gbps	10 km
IEEE 802.3bs (200GBASE-LR4)	4×50 Gbps	10 km
IEEE 802.3bs (400GBASE-LR8)	8×50 Gbps	10 km

1.2   Silicon photonics

The invention of the pin photodiode [6] in 1963, and the proposal for the use of optical fibers for communication in 1964 [7–8] were important for the future of semiconductor lasers and optical fiber communication. Nowadays, optical data communication in the wavelength range of 1550 nm has already replaced traditional copper-based electrical communication for long distances. Therefore, extensive research is going on for short reach, such as data communication within data centers, or even on-chip optical communication. The transparency of silicon in the wavelength windows of 1310 and 1550 nm makes it a good candidate for efficient light guiding. To enable this, silicon photonics has been under extensive investigation by many researchers for many years.

The potential for high volume production at low cost makes this platform attractive for commercial applications. On top of that, "the field of silicon photonics offers the possibility of dense integration, and the opportunity to use the well-developed CMOS electronics fabrication technology" [9].

Silicon can be excellent for light guiding on a chip [10] because it uses the contrast of relatively high refractive index silicon (used as a waveguide core), and relatively low refractive index silicon oxide (used as a waveguide cladding). A silicon photonics chip typically consists of (1) a silicon substrate, (2) 1–3 μm of silicon oxide, (3) 220–400 nm of silicon with a width of a few hundred nm, and (4) a top cladding consisting of air or silicon oxide, as shown in Fig. 1.5. Since the structure consists mainly of silicon on top of buried silicon oxide, it is also referred to as silicon-on-insulator (SOI).
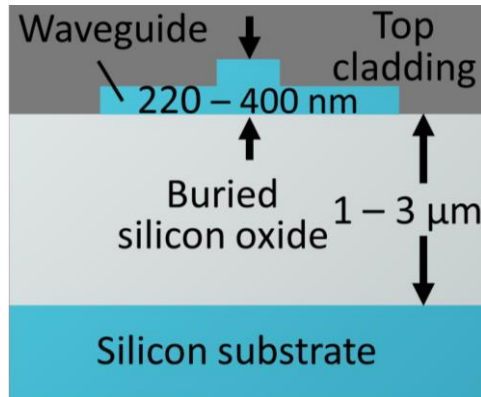
Figure 1.5: The layout of a typical silicon-on-insulator waveguide.
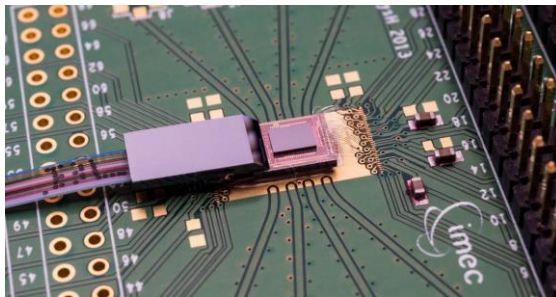
Figure 1.6: Microscopic image of a silicon photonics integrated circuit with many functionalities (figure from [11]).

Many passive and active functionalities can be realized on a grain-sized silicon photonic integrated circuit, like the one in Fig. 1.6. [11]. Examples for passive components include high-confinement low-loss waveguides and bends [12–13], high-Q micro ring resonators [14], grating couplers [15], and compact arrayed waveguide gratings [16]. Active components such as silicon-based micro ring resonator modulators [17–18] and Mach-Zehnder modulators [19] were demonstrated. Additionally, silicon-germanium-based electro-absorption modulators [20–21] and photodetectors [22], were also demonstrated. Finally, multi-channel wavelength division multiplexed micro ring modulators were demonstrated [23].

Silicon however has some disadvantages. The main drawback of silicon lies in its indirect bandgap. Generating a photon in a direct bandgap material, such as some III-V semiconductors, simply requires a transition of an electron from the conduction band to the valence band. However, in an indirect bandgap material, such as silicon, this direct transition can only happen if it is accompanied by a change of momentum (i.e. a phonon) [9]. Therefore, it is challenging to design a complete chip with an efficient light source only using silicon. One method of using the advantages of both silicon photonics as a low-cost platform, and III-V semiconductors as efficient light sources, is heterogeneous integration. The resulting device looks like the one in Fig. 1.7 [24]. This is discussed in more detail in the next section.
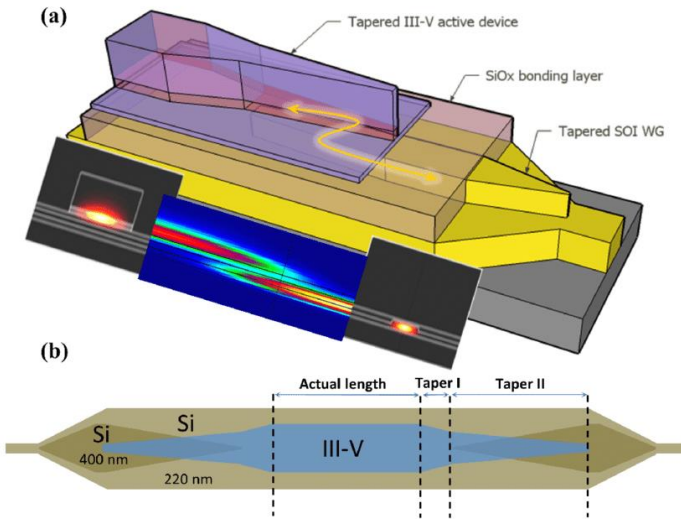
Figure 1.7: (**a**) 3D and (**b**) top view of heterogeneously integrated III-V-on-silicon laser diode (figure from [24]).

1.3   Heterogeneous III-V-on-silicon integration

As mentioned earlier, the potential of the silicon photonics platform is the high volume production at low cost. But since silicon is not an efficient light source due to its indirect bandgap [9], integration with a direct bandgap material is a necessity. A possible approach is heterogeneous III-V-on-silicon integration, where the light is first generated in the III-V waveguide, then couples down to the silicon waveguide using 230 μm long adiabatic tapers on both ends, as shown in Fig. 1.7 [24]. These tapers act as a semiconductor optical amplifier (SOA) if they are pumped. In the following subsections, we will discuss a few heterogeneous III-V-on-silicon integration techniques.

1.3.1 Integration techniques

There are several methods to achieve the integration of III-V semiconductors on silicon, such as flip-chip integration [25], hetero-epitaxial growth [26], bonding [27], and transfer printing [28]. Flip chip is advantageous because the devices can be fabricated on their native substrate. However, the integration technique is time-consuming and labour-hungry, since individual devices need to be aligned and placed with sub-micron precision. Hetero-epitaxial growth, as the name indicates, is based on growing an epitaxial layer structure of certain materials of interest on silicon. While this allows high-density integration, this technique is hindered by, amongst other things, the lattice mismatch between the epitaxial material and silicon. Bonding solves the problem of lattice mismatch by growing the epitaxial layer structure separately and integrating it at a later stage epi-side-down on top of the SOI die or wafer.
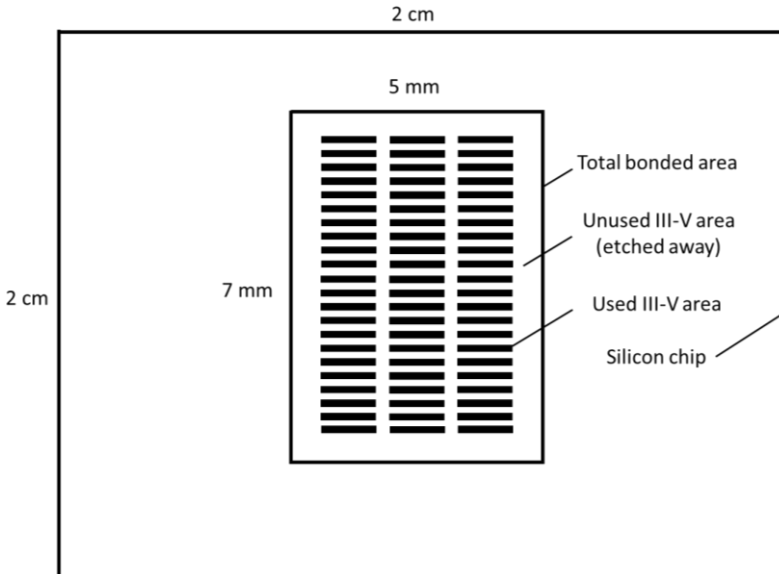
Figure 1.8: The used area of a bonded III-V die is around 30% of the total die area.

The drawback of bonding is not technical; it lies in the inefficient use of costly III-V materials. Fig. 1.8 shows the used area of a III-V die with a typical size of 5 mm $\times$ 7 mm, which is around 30%. Since the devices will be processed after die bonding, some space should be left free for metal pads, as well as on the edges to keep the devices safe. Since the price of a two-inch III-V wafer is a few thousands of USD, as opposed to a few tens of USD for a silicon wafer of the same size, efficient use of the III-V material is important. Transfer printing solves this problem, by transferring an array of preprocessed devices to the SOI. While this technology is still not as mature as bonding technologies, the prospects it offers are quite promising. As this work is aimed to improve the performance of laser devices, the mature bonding technology is chosen.

1.3.2   Adhesive bonding

Adhesive bonding for III-V on silicon integration is the preferred technology compared to other bonding technologies [29–31] because it relaxes the surface cleanliness requirements. It requires an adhesive bonding agent to be present between the two bonded dies/wafers. This agent is typically a polymer. For example, SU-8 [32], spin-on-glass [33], and divinylsiloxane-bis-benzocyclobutene (DVS-BCB) [34] can be used. DVS-BCB, or BCB for short, is usually the preferred bonding agent, due to the following factors (among others) [24]: (1) high degree of planarization, (2) excellent chemical resistance, (3) high optical clarity, and (4) low curing temperatures.

The bonding process flow is summarized in Fig. 1.9 [24, 35]. The process starts with spin coating BCB on the silicon substrate, pre-curing, and placing the III-V dies. The sample then is placed in the bonder machine, which applies pressure at high temperatures (280°C), over a duration of several hours in a vacuum chamber. All the reported results in this work are based on devices fabricated by adhesive bonding using BCB.
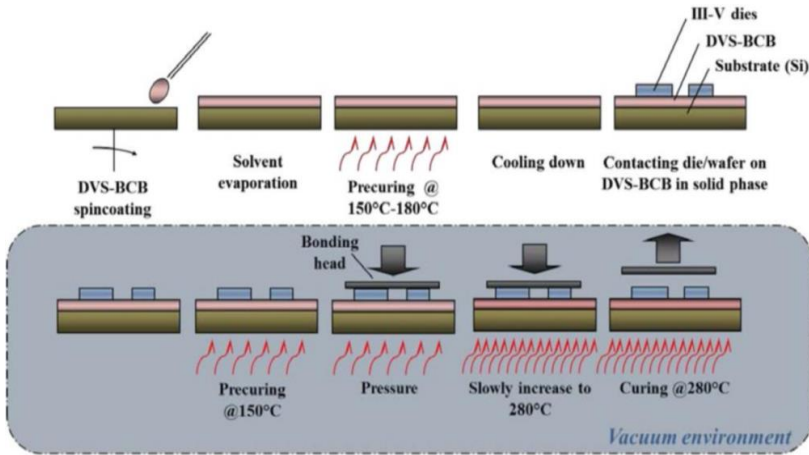
Figure 1.9: The bonding process of III-V dies on silicon substrate (figure from [24, 35]).

1.4   Modulation schemes and techniques

A characteristic of great importance for data communication is the maximum modulation speed of the transmitters. As discussed earlier, the IEEE standards for optical fiber communication are rapidly increasing in bitrate. To cope with this increase, several state-of-the-art results have been reported for both monolithic InP-based devices and heterogeneously integrated InP-on-Si laser devices. Before discussing the state-of-the-art and the performance of our devices, the commonly used modulation schemes and techniques will be discussed.

1.4.1 Modulation schemes

In general, modulation schemes can be based on amplitude, frequency or phase modulation. In this work, we use amplitude modulation for both our directly and externally modulated laser diodes. The detection of the signals can be either coherent or direct detection. In coherent detection, the carrier at the transmitter and at the receiver side should be phase-locked (or extensive digital signal processing is required when using free running lasers). This is not required in direct detection. The advantage of coherent detection is the possibility to use higher order modulation formats that offer higher spectral efficiency such as quadrature phase-shift keying (QPSK) and quadrature amplitude modulation (QAM). However, this increases the complexity of the system. For simplicity, we use direct detection.

Among other schemes, the two commonly used amplitude modulation schemes are non-return-to-zero on-off-keying (NRZ-OOK), and four-level pulse amplitude modulation (PAM-4). NRZ-OOK is the simplest two-level modulation format. It requires the highest bandwidth of the components but there are no stringent requirements on the linearity of the electronics and optics. It also provides the highest receiver sensitivity. A signal with two power or voltage levels creates a series of 1's and 0's as illustrated in Fig. 1.10 (a), which leads to an eye diagram like the one in Fig. 1.11 (a) [36]. Eye diagrams measure the quality of the transmission system by repetitively overlapping samples of the received data.
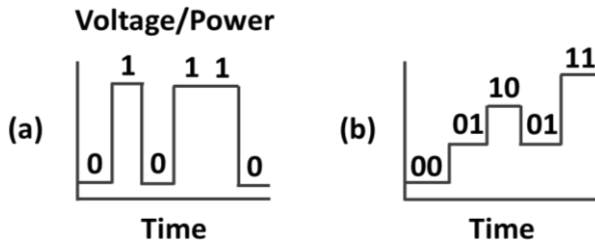
Figure 1.10: Data transmitted using (**a**) NRZ-OOK and (**b**) PAM-4 modulation schemes.
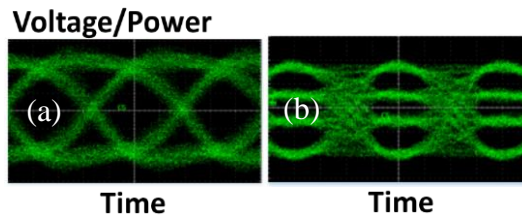
Figure 1.11: Eye diagrams of (**a**) NRZ-OOK and (**b**) PAM-4 signals (figure from [36]).

The downside of using NRZ-OOK is that it has low spectral efficiency. This means that the available bandwidth is not used efficiently. PAM-4, a four-level modulation scheme, is an alternative that provides higher spectral efficiency. This allows doubling the bitrate for the same bandwidth, at the expense of lowering the

modulation amplitude and increasing the linearity and signal-to-noise requirements on electronic circuits and photonic devices. A signal with four voltage or power levels creates a series of 00's, 01's, 10's and 11's as illustrated in Fig. 1.10 (b), which results in the eye diagram in Fig. 1.11 (b) [36].

1.4.2   Direct versus external modulation techniques

To send information over an optical link using an optical signal, one of two modulation techniques could be used. The first technique is direct modulation, in which the electrical current flowing in the optical source (i.e. the laser) is modulated by a series of 1's and 0's. As a result, the output optical signal is a series of 1's and 0's. After that, the optical signal travels in the optical link (on- or off-chip), and the reverse process happens at the receiver side, using a photodetector. Directly modulated lasers (DMLs) are simple and compact, as the presence of a modulator is not necessary. Fig. 1.12 (a) shows a simplified block diagram of the operation of a directly modulated laser diode.
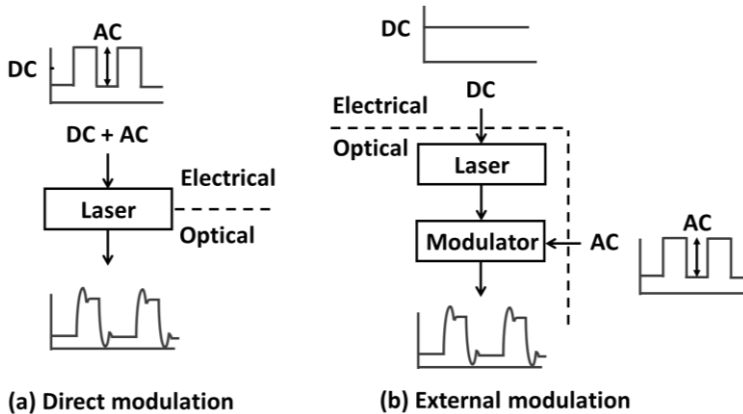
Figure 1.12: Schematic showing the basic operation of (**a**) direct modulation versus (**b**) external modulation.

Although the bandwidth of directly modulated lasers can be relatively high [37], modulation at high frequencies often comes with a large chirp. This means that not only the amplitude of the signal is modulated, but also the frequency. Some work has been done to manage this chirp [38], which is not trivial, especially at high data rates.

The second modulation technique is external modulation. This is done by introducing an (external) modulator, as shown in Fig. 1.12 (b). There are several types of modulators, such as electro-optic modulators (EOMs), and electro-absorption modulators (EAMs). Compared to direct modulation, external modulation adds some complexity to the system. However, this is sometimes necessary to improve the performance and enhance the modulation bandwidth of an optical link. A simplified block diagram showing the operation of an externally modulated laser diode is depicted in Fig. 1.12 (b).

Electro-optic modulators such as Mach-Zehnder modulators (MZMs) rely on the principle of phase modulation. In a Mach-Zehnder configuration, light is equally split into two arms. The refractive index in both arms is modulated by carrier injection or depletion in a push-pull configuration. This induces a phase difference between the two arms, which is converted to amplitude modulation at the output. Many MZMs have been demonstrated [39–42]. However, these have a high $V_\pi \cdot L_\pi$ product, where V_π is the voltage required for a π phase shift over a given length L_π.

The mechanism of electro-absorption modulation is simple: modulating the absorption of an optical signal according to an electrical signal. This technique has a bandwidth limited by the RC constant of the modulator, where C is typically the junction capacitance and R is determined by the series resistance and output impedance of the driver. As the junction capacitance decreases with decreasing the width and the length of the EA modulator, a shorter and narrower EAM will result in a higher modulation bandwidth. However, a small EAM area would limit the extinction ratio, so a compromise must be sought. Many electro-absorption-modulated lasers (EMLs) were demonstrated on different material platforms [43–45].

The main advantage of external modulation techniques is that they suffer less from frequency modulation (chirp) compared to direct modulation. On the other hand, the high insertion loss, high power consumption and circuit complexity remain disadvantages for these techniques.

1.5 Attribution of work

The choice of some design parameters (SOI, laser, and epitaxial structures) is based on work of previous PhD students, namely Dr. Amin Abbasi and Mr. Shahram Keyvaninia on standard single-section lasers. The design parameters were often tuned by the author to optimize the performance. The simulations shown in this thesis were done by the author, unless otherwise stated (e.g. citation of another work).

The fabrication was done by the author, based on the original fabrication recipe developed by Dr. Amin Abbasi and Mr. Shahram Keyvaninia. The recipe was often modified by the author, with certain steps added to perform certain processes. Technical cleanroom support was occasionally provided by cleanroom staff, namely Mr. Steven Verstuyft, Mr. Muhammad Muneeb, and Mrs. Liesbet Van Landschoot (SEM and FIB). The ebeam SOI samples were fabricated by Mr. Muhammad Muneeb, and the DUV SOI samples were fabricated by IMEC.

The characterization was mainly done by the author, with equal contribution of Mr. Keqi Ma in self-pulsation lasers. There was also occasional assistance by IDLab, namely Mr. Joris Van Kerrebrouck in high speed characterization of the electro-absorption modulator, in collaboration with Prof. Johan Bauwelinck and Prof. Peter Ossieur.

1.6   Outline

The content of this work, which consists of five chapters, is outlined below.

Chapter 1 has put this work in context and has shown its significance. The advantages of optical over electrical interconnects, and the main wavelengths of operation for optical communication were laid out. The significance of silicon photonics was discussed, leading to the advantages of heterogeneous integration of III-V-on-silicon. Finally, as this thesis contains demonstrations of high-speed devices, the main modulation schemes and techniques were introduced.

In chapter 2, we provide essential background knowledge for the understanding of this work. An overview of DFB laser diodes and other types of lasers is given. Monolithic versus heterogeneously integrated III-V-on-silicon laser diodes are compared. Moreover, basic technical knowledge of the fabrication procedure of the different devices and their material composition is presented.

Chapter 3 investigates the design and characterization of two-section DFB laser diodes. First, self-pulsation DFB laser diodes are presented. Then, we use these two-section lasers to achieve higher modulation bandwidth compared to their equivalent single-section lasers. After that, we use the same devices to show low-threshold DFB laser diodes, compared to their equivalent single-section DFB laser diodes. These devices have a potential use in radio-over-fiber systems and data communication applications.

In chapter 4, we discuss the advances in III-V-on-Si electro-absorption modulated DFB laser diodes. We show an improved design and demonstrate high-speed data transmission of 80 Gbps NRZ-OOK signals, which is beneficial for data communication applications.

Chapter 5 shows a compact III-V-on-Si DFB laser diode. This is done by design and simulation of an alternative short taper structure. The laser with the short taper structure is fabricated and measured. Finally, the challenges for such a structure are outlined.

Finally, Chapter 6 draws conclusions and discusses the future prospects of this work.

1.7   List of publications

This work has resulted in a number of publications in both international peer-reviewed journals, and international conferences. These are listed below.

1.7.1   International peer-reviewed journals

1. **M. Shahin**, J. Rahimi Vaskasi, J. Van Kerrebrouck, P. Ossieur, X. Yin, J. Bauwelinck, G. Roelkens, G. Morthier, "80 Gbps NRZ-OOK Electro-Absorption Modulation of InP-on-Si DFB Laser Diodes," IEEE Photonics Technology Letters, 31(7), pp. 533–536, (2019). (https://doi.org/10.1109/LPT.2019.2900518)

2. **M. Shahin**, K. Ma, A. Abbasi, G. Roelkens, G. Morthier, "45 Gbps Direct Modulation of Two-Section InP-on-Si DFB Laser Diodes," IEEE Photonics Technology Letters, 30(8), pp. 685–687, (2018). (https://doi.org/10.1109/LPT.2018.2811906)

3. K. Ma, **M. Shahin**, A. Abbasi, G. Roelkens, G. Morthier, "Demonstration of InP-on-Si Self-Pulsating DFB Laser Diodes for Optical Microwave Generation," IEEE Photonics Journal, 9(4), p. 1504608, (2017). (https://doi.org/10.1109/JPHOT.2017.2724840)

1.7.2 International conferences

1. G. Morthier, **M. Shahin**, J. Rahimi Vaskasi, P. Ossieur, X. Yin, J. Bauwelinck, G. Roelkens, "Towards high speed InP-on-silicon DFB lasers with low power consumption," International Conference on Optics and Electro-Optics (ICOL) (invited), India, (2019).

2. K. Van Gasse, A. Abbasi, **M. Shahin,** J. Verbist, J. Van Kerrebrouck, G. Torfs, B. Moeneclaey, J. Bauwelinck, X. Yin, G. Roelkens, G. Morthier, "Silicon photonic Radio-over-Fiber transceivers and microwave photonic up-converters," (invited), Photonics and Electromagnetics Research Symposium (PIERS), Italy, (2019).

3. **M. Shahin**, J. Rahimi Vaskasi, J. Van Kerrebrouck, A. Abbasi, K. Van Gasse, M. Muneeb, L. Breyne, P. Ossieur, X. Yin, J. Bauwelinck, G. Roelkens, G. Morthier, "Demonstration of 80 Gbps NRZ-OOK Electro-Absorption Modulation of InP-on-Si DFB Laser Diodes," Conference on Lasers and Electro-Optics (CLEO), United States, (2019).

4. **M. Shahin**, J. Van Kerrebrouck, G. Roelkens, G. Morthier, "InP-on-Si DFB Laser Diode with Distributed Reflector for Improved Power Efficiency," European Conference on Integrated Optics (ECIO), Belgium, (2019).

5. **M. Shahin**, G. Roelkens, G. Morthier, "Compact InP-on-Si DFB Laser Diodes," IEEE Photonics Society Benelux Symposium, Belgium, (2018).

6. A. Rahim, A. Abbasi, **M. Shahin**, Nuno Sequeira Andre, Andre Richter, Joris Van Kerrebrouck, K. Van Gasse, A. Katumba, Bart Moeneclaey, Xin Yin, G. Morthier, R. Baets, G. Roelkens, "50 Gb/s DMT and 120 Mb/s LTE signal transmission over 5 km of optical fiber using a silicon photonics transceiver," Advanced Photonics Congress, Switzerland, (2018).

7. G. Muliuk, K. Van Gasse, **M. Shahin**, J. Verbist, A. J. Trindade, B. Corbett, D. Van Thourhout, G. Roelkens, "4x25Gbit/s Silicon Photonics Tunable Receiver using Transfer Printed III-V Photodiodes," IEEE Photonics Conference (IPC), United States, (2018).

8. **M. Shahin**, A. Abbasi, K. Ma, G. Roelkens, G. Morthier, "Towards High Modulation Bandwidth using Two-Section InP-on-Si DFB Laser Diodes," IEEE Photonics Society Benelux Symposium, The Netherlands, (2017).

9. **M. Shahin**, K. Ma, A. Abbasi, G. Roelkens, G. Morthier, "Demonstration of Self-Pulsating InP-on-Si DFB Laser Diodes," IEEE Photonics Conference (IPC), United States, (2017).

10. G. Morthier, A. Abbasi, **M. Shahin**, J. Verbist, G. Roelkens, "High speed modulation of InP membrane DFB laser diodes," International Conference on Transparent Optical Networks (ICTON) (invited), Italy, (2016).

References

[1] Intel. URL: https://itpeernetwork.intel.com/data-centre-predictions-2017/, (2017).

[2] J. Bowers, URL: http://cadlab.ece.ucsb.edu/optical

[3] M. Wartak, "Computational photonics: an introduction with MATLAB," Cambridge University Press, (2013).

[4] Wikipedia, URL: https://en.wikipedia.org/wiki/Multi-mode_optical_fiber

[5] 802.3bm-2015 - IEEE Standard for Ethernet - Amendment 3: Physical Layer Specifications and Management Parameters for 40 Gb/s and 100 Gb/s Operation over Fiber Optic Cables, (2015).

[6] G. Dummer, "Electronic inventions and discoveries, electronics from its earliers beginnings to the present day" 3rd edition, Pergamon, (1983).

[7] J. Nishizawa et al., "Optical waveguiding structure containing materials of relatively high refractive index and relatively low refractive index," Japanese patent filed S39–64040, (1964).

[8] T. Okoshi, "Optical fibers," 1st edition, Elsevier, (1982).

[9] R. Soref, "The Past, Present, and Future of Silicon Photonics," IEEE Journal of Selected Topics in Quantum Electronics, 12(6), pp. 1678–1687, (2006).

[10] R. A. Soref and J. P. Lorenzo, "Single-crystal silicon: a new material for 1.3 and 1.6 μm integrated-optical components," Electronics Letters, 21(21), pp. 953–954, (1985).

[11] "imec: Next-generation silicon photonics," URL: https://www.imec-int.com/en/next-generation-silicon-photonics, (2019).

[12] P. Dumon, W. Bogaerts, V. Wiaux, J. Wouters, S. Beckx, J. V. Campenhout, D. Taillaert, B. Luyssaert, P. Bienstman, D. V. Thourhout, and R. Baets, "Low-loss SOI photonic wires and ring resonators fabricated with deep UV lithography," IEEE Photonics Technology Letters, 16(5), pp. 1328–1330, (2004).

[13] Y. A. Vlasov and S. J. McNab, "Losses in single-mode silicon-oninsulator strip waveguides and bends," Optics Express 12(8), pp. 1622–1631, (2004).

[14] J. Niehusmann, A. Vorckel, P. H. Bolivar, T. Wahlbrink, W. Henschel, and H. Kurz, "Ultrahigh-quality-factor silicon-on-insulator microring resonator," Optics Letters, 29(24), pp. 2861–2863, (2004).

[15] D. Taillaert, F. Van Laere, M. Ayre, W. Bogaerts, D. Van Thourhout, P. Bienstman, and R. Baets, "Grating couplers for coupling between optical fibers and nanophotonic waveguides," Japanese Journal of Applied Physics, 45(8R), p. 6071, (2006).

[16] T. Fukazawa, F. Ohno, and T. Baba, "Very compact arrayedwaveguide-grating demultiplexer using Si photonic wire waveguides," Japanese Journal of Applied Physics, 43(5B), p. L673, (2004).

[17] Q. Xu, S. Manipatruni, B. Schmidt, J. Shakya, and M. Lipson, "12.5 Gbit/s carrier-injection-based silicon micro-ring silicon modulators," Optics Express, 15(2), pp. 430–436, (2007).

[18] S. Manipatruni, R. K. Dokania, B. Schmidt, N. Sherwood-Droz, C. B. Poitras, A. B. Apsel, and M. Lipson, "Wide temperature range operation of micrometer-scale silicon electro-optic modulators," Optics Letters, 33(19), pp. 2185–2187, (2008).

[19] L. Liao, D. Samara-Rubio, M. Morse, A. Liu, D. Hodge, D. Rubin, U. D. Keil, and T. Franck, "High speed silicon Mach-Zehnder modulator," Optics Express, 13(8), pp. 3129–3135, (2005).

[20] J. Liu, M. Beals, A. Pomerene, S. Bernardis, R. Sun, J. Cheng, L. C. Kimerling, J. Michel, "Waveguide-integrated, ultralow-energy GeSi electro-absorption modulators," Nature Photonics 2, 433–437, (2008).

[21] J. Verbist, M. Verplaetse, S. A. Srinivasan, J. Van Kerrebrouck, P. De Heyn, P. Absil, T. De Keulenaer, R. Pierco, A. Vyncke, G. Torfs, X. Yin, G. Roelkens, J. Van Campenhout, J. Bauwelinck, "Real-time 100 Gb/s NRZ and EDB transmission with a GeSi electro-absorption modulator for short-reach optical interconnects," Journal of Lightwave Technology, 36(1), pp. 90–96, (2018).

[22] J. Liu, D. D. Cannon, K. Wada, Y. Ishikawa, S. Jongthammanurak, D. T. Danielson, J. Michel, and L. C. Kimerling, "Tensile strained Ge p–i–n photodetectors on Si platform for C and L band telecommunications", Applied Physics Letters, 87, p. 11110, (2005).

[23] P.P. Absil, P. De Heyn, P. Dumon, D. Van Thourhout, P. Verheyen, S. Selvaraja, G. Lepage, M. Pantouvaki, M. Rakowski, J. Van Campenhout, "Advances in silicon photonics WDM devices, Conference on Next-Generation Optical Networks for Data Centers and Short-Reach Links" (invited), p. 90100J, (2014).

[24] G. Roelkens, A. Abassi, P. Cardile, U. Dave, A. de Groote, Y. de Koninck, S. Dhoore, X. Fu, A. Gassenq, N. Hattasan, Q. Huang, S. Kumari, S. Keyvaninia, B. Kuyken, L. Li, P. Mechet, M. Muneeb, D. Sanchez, H. Shao, T. Spuesens, A. Z. Subramanian, S. Uvin, M. Tassaert, K. van Gasse, J. Verbist, R. Wang, Z. Wang, J. Zhang, J. van Campenhout, X. Yin, J. Bauwelinck, G. Morthier, R. Baets, and D. van Thourhout, "III-V-on-Silicon Photonic Devices for Optical Communication and Sensing," Photonics , 3, pp. 969–1004, (2015).

[25] T. Mitze, M. Schnarrenberger, L. Zimmermann, J. Bruns, F. Fidorra, K. Janiak, J. Kreissl, S. Fidorra, H. Heidrich, and K. Petermann, "CWDM transmitter module based on hybrid integration," IEEE Journal of Selected Topics in Quantum Electronics, 12(5), pp. 983–987, (2006).

[26] D. Fehly, A. Schlachetzki, A. S. Bakin, A. Guttzeit, and H.-H. Wehmann, "Monolithic InGaAsP optoelectronic devices with silicon electronics," IEEE Journal of Selected Topics in Quantum Electronics, 37(10), pp. 1246–1252, (2001).

[27] G. Roelkens, L. Liu, D. Liang, R. Jones, A. Fang, B. Koch, J. Bowers, "III-V/silicon photonics for on-chip and inter-chip optical interconnects," Laser & Photonics Reviews, 4(6), pp. 751–779, (2010).

[28] A. De Groote, P. Cardile, A. Subramanian, A. Fecioru, C. Bower, D. Delbeke, R. Baets, G. Roelkens, "Transfer-printing-based integration of single-mode waveguide-coupled III-V-on-silicon broadband light emitters," Optics Express, 24(13), pp. 13754–13762, (2016).

[29] B. Lee, S. Seok, K. Chun, "A study on wafer level vacuum packaging for MEMS devices," Journal of Micromechanics and Microengineering, 13(5), pp. 663–669, (2003).

[30] N. Miki and S. M. Spearing, "Effect of nanoscale surface roughness on the bonding energy of direct-bonded silicon wafers," Journal of Applied Physics, 94(10), pp. 6800–6806, (2003).

[31] C. C. Lee and R. W. Chuang, "Fluxless non-eutectic joints fabricated using gold-tin multilayer composite," IEEE Transactions on Components and Packaging Technologies, 26(2), pp. 416–422, (2003).

[32] F. J. Blanco, M. Agirregabiria, J. Garcia, J. Berganzo, M. Tijero, M. T. Arroyo, J. M. Ruano, I. Aramburu, and K. Mayora, "Novel three-dimensional embedded SU-8 microchannels fabricated using a low temperature full wafer adhesive bonding," Journal of Micromechanics and Microengineering, 14(7), 1047–1056, (2004).

[33] H. C. Lin, K. L. Chang, G. W. Pickrell, K. C. Hsieh, and K. Y. Cheng, "Low temperature wafer bonding by spin on glass," Journal of Vacuum Science and Technology B, 20(2), pp. 752–754, (2002).

[34] F. Niklaus, H. Andersson, P. Enoksson, and G. Stemme, "Low temperature full wafer adhesive bonding of structured wafers," Sensors and Actuators A: Physical, 92(1-3), pp. 235–241, (2001).

[35] S. Tanaka, T. Akiyama, S. Sekiguchu, K. Morito, "Silicon photonics optical transmitter technology for Tb/s-class I/O co-packaged with CPU," FUJUTSI Scientific and Technical Journal, 50, pp. 123–131, (2014).

[36] X. Miao, M. Bi, Y. Fu, L. Li, and W. Hu "Experimental Study of NRZ, Duobinary and PAM-4 in O-band DML-based 100G-EPON," IEEE Photonics Technology Letters, 29, pp. 1490–1493, (2017).

[37] Y. Matsui, R. Schatz, T. Pham, W. A. Ling, G. Carey, H. M. Daghighian, D. Adams, T. Sudo, and C. Roxlo , "55 GHz Bandwidth Distributed Reflector Laser," Journal of Lightwave Technology, 35(3), pp. 397–403, (2017).

[38] A. Abbasi, B. Moeneclaey, X. Yin, J. Bauwelinck, G. Roelkens, G. Morthier, "10G/28G Chirp Managed 20 km Links based on Silicon Photonics Transceivers," IEEE Photonics Technology Letters, 29(16), pp.1324–1327, (2017).

[39] X. Xiao, H. Xu, X. Li, Z. Li, T. Chu, Y. Yu, and J. Yu, "High-speed, low-loss silicon Mach–Zehnder modulators with doping optimization," Optics Express, 21(4), pp. 4116–4125, (2013).

[40] L. Yang, J. Ding, "High-Speed Silicon Mach–Zehnder Optical Modulator With Large Optical Bandwidth," Journal of Lightwave Technology, 32(5), pp. 966–970, (2014).

[41] M. Streshinsky, R. Ding, Y. Liu, A. Novack, Y. Yang, Y. Ma, X. Tu, E. Koh, S. Chee, A. Eu-Jin Lim, P. Guo-Qiang Lo, T. Baehr-Jones, and M. Hochberg, "Low power 50 Gb/s silicon traveling wave Mach-Zehnder modulator near 1300 nm," Optics Express 21(25), pp. 30350–30357, (2013).

[42] D. Patel, S. Ghosh, M. Chagnon, A. Samani, V. Veerasubramanian, M. Osman, and D. V. Plant, "Design, analysis, and transmission system performance of a 41 GHz silicon photonic modulator," Optics Express 23(11), pp. 14263–14287, (2015).

[43] M. Theurer, H. Zhang, Y. Wang, W. Chen, L. Chen, L. Zeng, U. Troppenz, G. Przyrembel, A. Sigmund, M. Moehrle, and M. Schell "2 × 56 GB/s From a Double Side Electroabsorption Modulated DFB Laser and Application in Novel Optical PAM4 Generation," Journal of Lightwave Technology, 35(4), pp. 706–710, (2017).

[44] A. Abbasi, L. A. Shiramin, B. Moeneclaey, J. Verbist, X. Yin, J. Bauwelinck, D. Van Thourhout, G. Roelkens, and G. Morthier, "III-V-on-Silicon C-band High-Speed Electro-Absorption Modulated DFB Laser," Journal of Lightwave Technology, 36(2), pp. 252–257, (2018).

[45] A. Abbasi J. Verbist, L. A. Shiramin, M. Verplaetse, T. De Keulenaer, R. Vaernewyck, R. Pierco, A. Vyncke, X. Yin, G. Torfs, G. Morthier, J. Bauwelinck, G. Roelkens, "100-Gb/s Electro-Absorptive Duobinary Modulation of an InP-on-Si DFB Laser," IEEE Photonics Technology Letters, 30(12), pp. 1095–1098, (2018).

2

Overview of DFB Laser Diodes

Contents

2.1 Introduction

Distributed feedback (DFB) laser diodes are the devices of choice in this work to realize different on-chip laser functionalities on the developed III-V-on-silicon platform. Before discussing these functionalities in detail, this chapter provides an appropriate background of the theory and technology discussed in the following chapters. We first describe the basics of lasers and laser diodes. Then, we discuss the operation and structure of DFB laser diodes. After that, we briefly describe other common types of lasers, while placing them all in the context of heterogeneous integration of III-V-on-silicon. Then, we compare monolithic III-V and heterogeneous III-V-on-silicon laser diodes. After that, we discuss the fabrication procedure of III-V-on-silicon DFB lasers. Finally, we show the three III-V epitaxial layer structures used in this work.

2.2   Introduction to lasers

The word LASER is an acronym for "Light Amplification by Stimulated Emission of Radiation". As the name suggests, lasers are devices that emit light through an amplification process called "stimulated emission". Generally, lasers consist of three main components: (1) an active (gain) medium, (2) a pumping mechanism, and (3) optical feedback, as exemplified in Fig. 2.1.
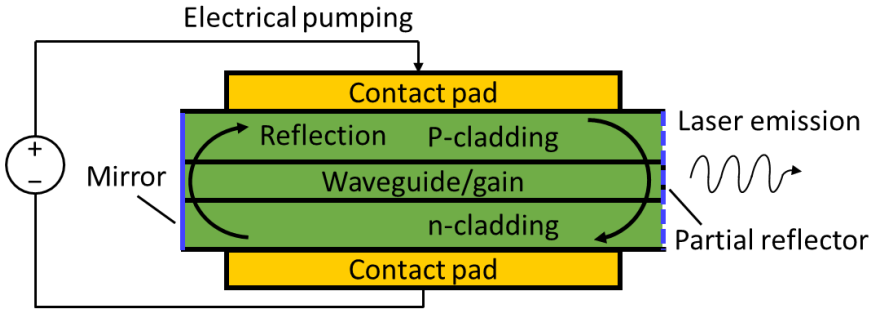

Figure 2.1: Lasers consist of three main components: an active (gain) medium, a pump mechanism, and optical feedback.

Pumping provides the energy source to generate light. This can be electrical pumping as shown in Fig. 2.1, or optical pumping using another light source. The active medium is made of materials that can generate and amplify light over a certain wavelength range. The ability of the active medium to increase the optical power is referred to as the gain of the medium. The active medium together with the optical feedback mechanism (e.g. the mirrors in Fig. 2.1) forms an oscillator. In order to extract the laser light, one of the mirrors can be designed to have a lower reflectivity than the other.

Today, many types of lasers exist for many different applications. We can classify these lasers depending on their active medium. For example, solid-state lasers use crystalline materials as their active medium. The first working laser was a solid state laser invented in 1960 by Theodore Maiman. This laser was the Ruby laser, with its active medium being Ruby (chromium-doped corundum). It operated in the visible region, with the wavelength of operation being 694.3 nm. Due to its limitations in terms of low output power, low efficiency, and its pulsed operation, other lasers started to outperform it. Other examples include gas lasers, with the active medium being a gas. The first gas laser was the famous Helium-Neon (HeNe) laser invented in 1961 by Bell Labs. This bulky laser had a continuous-wave (CW) operation at 633 nm.

Laser diodes are the lasers of choice in this work. This type of lasers is sometimes referred to as semiconductor lasers, as the active medium consists of semiconductor materials. This laser outperforms the other types of lasers in terms

of the price, compactness, and power consumption. Basics of laser diodes are discussed in more detail in the next section.

2.3   Introduction to laser diodes

2.3.1   Spontaneous and stimulated emission, and absorption

To explain the "lasing" operation in laser diodes, two important concepts must be introduced. The first concept is spontaneous emission, illustrated in Fig. 2.2 (a). Spontaneous emission occurs when an electron transits from the conduction to the valence band, which results in an emitted photon. In this case, the phase of the generated photons is random. Although the light is generated, the lasing operation has not yet started. The reverse process to spontaneous emission is absorption. In this process, an electron absorbs the energy of an incident photon, and uses it to transit from the valence to the conduction band, as shown in Fig. 2.2 (b).
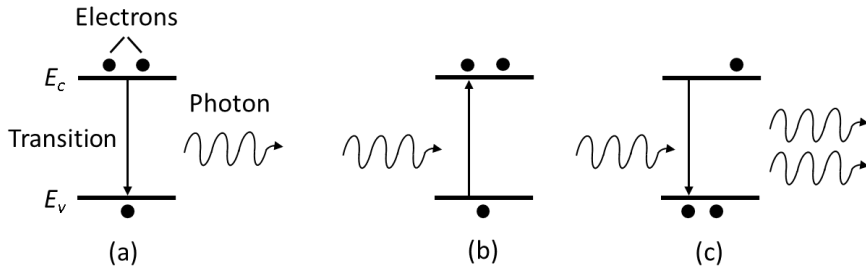

Figure 2.2: (**a**) spontaneous emission, (**b**) absorption, and (**c**) stimulated emission

One of the main properties of laser light is coherence (i.e. all photons are in-phase). This happens if the photons generated by spontaneous emission start to stimulate other transitions (i.e. from the conduction to the valence band). This is illustrated in Fig. 2.2 (c), where an input of one incident photon results in an output of two photons (the incident photon and the stimulated photon). This process is referred to as stimulated emission. The photons generated by this process have the same wavelength (frequency) and phase as the incident photons, which is the origin of light coherence in lasers. The bandgap energy E_g is defined as the difference between the conduction band E_c and the valence band E_v energy levels, as given by (2.1). The photon energy, and consequently the wavelength (frequency) of this photon is also determined by the bandgap, as given by (2.1).

$$E_g = E_c - E_v \cong h\nu \qquad (2.1)$$

where h is Planck's constant, and ν is the frequency of the photon. The frequency is related to the wavelength λ and speed of light c by:

$$\nu = c/\lambda \qquad (2.3)$$

It is important to note that the occurrence of stimulated emission does not mean the lasing action has started yet. To achieve lasing, the optical gain should compensate the internal and cavity losses. This point is referred to as the lasing threshold, and the corresponding gain is referred to as the threshold gain g_{th}, expressed by:

$$g_{th} = a_0 + \frac{1}{2L}\ln(\frac{1}{R_1 R_2}) \qquad (2.4)$$

Internal loss   Cavity loss

where a_0 is the internal loss, R_1 and R_2 are the mirror reflectivities, and L is the length of the active medium. The second term represents the cavity loss.

2.3.2   Direct and indirect band structures

As was shown in Fig. 2.2, the transition of an electron from the conduction to the valence band produces a photon. There are two types of band structures: direct and indirect. If the electrons at the bottom of the conduction band and the holes at the top of the valence band have the same momentum, i.e. they can recombine without the need of momentum change, then the band structure is direct. On the other hand, if the recombination requires a momentum change, then the band structure is indirect. To give some examples, Fig. 2.3 illustrates the direct band structure of InP (left), and the indirect band structure of silicon (right) [1].

There are two types of carrier recombination: radiative and non-radiative recombination. Depending on the band structure, one recombination mechanism can be more dominant than the other. In radiative recombination, an electron in the conduction band recombines with a hole in the valence band, resulting in a photon emission. This can be either spontaneous or stimulated emission. However, sometimes a non-radiative recombination occurs, such as recombination through defect or trap levels (Shockley-Read-Hall), or when the energy released by electron hole recombination is transferred to another electron (Auger recombination). Another non-radiative recombination mechanism is surface recombination. In this mechanism, trap states at the surface act as a non-radiative recombination center. Non-radiative recombination mechanisms are dominant in materials with indirect bandgap structures. On the other hand, radiative recombination is easier and more efficient in materials with direct band structures. This is because in an indirect band structure, recombination requires a lattice vibration (phonon), which makes light generation inefficient.

Fig. 2.4 shows group II to VI materials of the periodic table. Group IV contains indirect band structure materials, such as Silicon (Si) and Germanium (Ge). By combining elements in group III and V, one can get direct bandgap materials. An example is Indium-Phosphide (InP) or Gallium-Arsenide (GaAs). Direct bandgap materials offer the possibility to make active devices such as lasers and

photodiodes. Depending on the bandgap energy levels of the material, the emission wavelength and thus the application can differ. It is worth mentioning that not all III-V materials are direct bandgap. For example, Aluminum-Antimony (AlSb) is an indirect bandgap material. Combining II-VI materials can also result in direct bandgap materials, such as Zinc-Oxide (ZnO) and Cadmium-Oxide (CdO) [2].
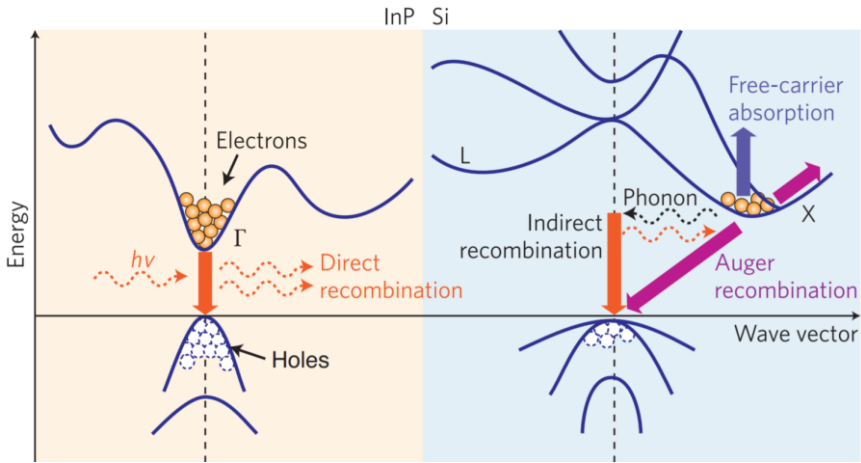

Figure 2.3: Energy band diagrams of InP direct band structure (left) and silicon indirect band structure (right) (figure from [1]).

Figure 2.4: The periodic table showing group II to group VI materials, which contains many direct and indirect bandgap materials.

2.3.3   The PN junction

We have introduced the concept of spontaneous and stimulated emission. Laser diodes use the concept of stimulated emission for the generation of light. We have also introduced direct and indirect bandgap materials, and how the former has more efficient light generation properties. Using this knowledge, we will introduce the structure of a laser diode: The PN junction.

A PN junction brings n- and p-doped semiconductor materials together to form a junction. The n-doped material contains an excess concentration of electrons, while the p-doped contains an excess concentration of holes. Holes can be defined here as the absence of an electron. The concentration of electrons is expressed by the Fermi levels E_f in Fig. 2.5 (a, b), where the Fermi level is higher in an n-doped material than in a p-doped material. We have previously introduced E_c and E_v as the energies of the conduction and the valence bands, respectively. E_i is defined as the intrinsic Fermi level, for an undoped material, with an equal electron and hole concentrations. Bringing the p- and n-doped materials together would result in the PN junction shown in Fig. 2.5 (c) with a built-in potential (V_{bi}). The junction formed when two semiconductor materials with the same bandgap are brought together is referred to as a homojunction, as shown in Fig. 2.5 (c). On the other hand, if the bandgaps were different, then it is referred to as a heterojunction or a heterostructure, as illustrated later in Fig. 2.7.

Looking at the PN junctions under different bias conditions helps to understand the working mechanism. Let's consider the two cases of zero and forward bias shown in Fig. 2.6 (a, b). Under zero bias, the electron in the n-type material cannot make it to the p-type material due to the built-in potential, as seen in Fig. 2.6 (a). Therefore, forward biasing the junction is necessary. Fig. 2.6 (b) shows the forward biasing of a PN-junction in which the electrical current starts to pass through the junction, and the electrons start to recombine with the holes. E_{fn} represents the electron concentration in the n-type, while E_{fp} represents the electron concentration in the p-type.
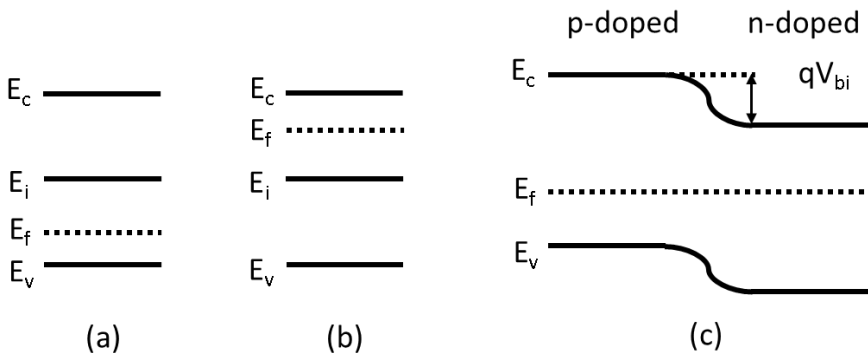

Figure 2.5: (**a, b**) p- and n-doped materials, with the Fermi levels indicating the concentration of electrons and holes, (**c**) shows the PN junction and its built-in potential.
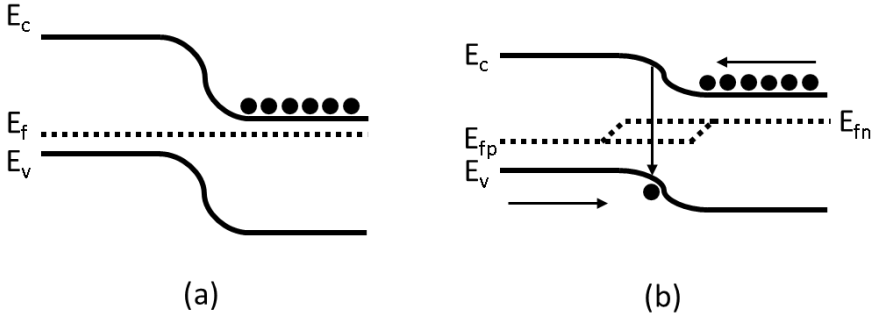
Figure 2.6: PN junction under (**a**) zero bias, and (**b**) under forward bias

Although PN junctions are useful, the commonly used junctions for most photonic applications are PIN junctions. The energy diagrams of PN and PIN junctions are shown in Fig. 2.7 (a, b). The difference between the two is the undoped intrinsic region between the heavily doped p- and the n- type regions in PIN junctions. This creates a longer region (with a smaller bandgap in the case of a heterojunction) in which the electrons and holes can recombine to generate photons. When PIN junctions are formed by two heterojunctions, they are referred to as double heterojunctions. A special type of double heterojunction is a quantum well, in which only certain energy levels are allowed inside the well. The energy diagram of a quantum well is shown in Fig. 2.7 (c).

Figure 2.7: The energy diagram of (**a**) a PN heterojunction, (**b**) a PIN double heterojunction and (**c**) a quantum well double heterojunction

Figure 2.8: Various photonic applications of PIN junctions

PIN junctions can be used for different applications, depending on the bias conditions, as shown in the current-voltage characteristics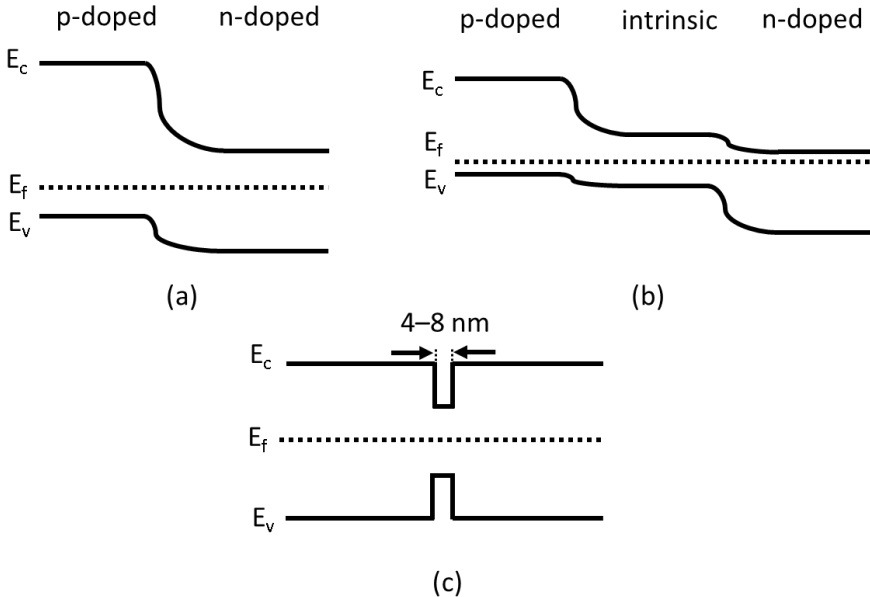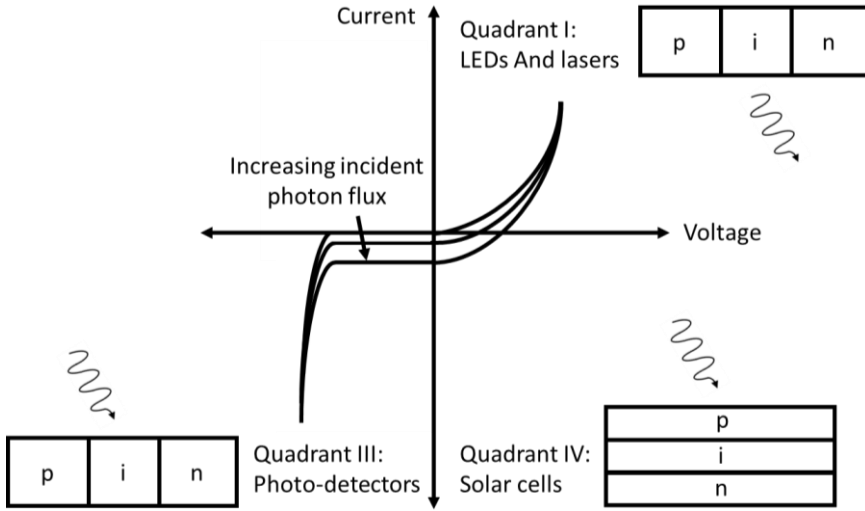 in Fig. 2.8. If the junction is forward biased in quadrant I, then it can be used as an LED or as a laser diode. In this case, injected carriers are used to produce photons. This is the quadrant that our devices operate at.

If the junction is reverse-biased (quadrant III) with a negative voltage, then it can be used as a photodetector. Here, the opposite happens: photons are used to generate carriers. With more incident light, the achieved reverse current increases. Finally, forward-biased junctions can be used in quadrant IV as solar cells, where energy is produced by incident light.

2.3.4   Bulk versus multi quantum wells

We have briefly introduced III-V materials. These materials can be put in different structures. Bulk III-V materials are the simplest form of materials used as an active medium. In such a material, a potential well confines the electrons and holes, and a photon is generated when a transition of an electron from the conduction to the valence band happens. The energy of this photon E was already discussed in the previous section. Lasers with bulk materials exhibit high threshold currents due to the moderate gain levels [3]. This results in low output power, and poor performance at high temperatures. The widely used III-V structures that overcome the issues of bulk III-V structures are multi quantum wells (MQWs).

Fig. 2.9 shows a comparison between the band structures of InGaAsP (a) bulk and (b) MQWs. Bulk III-V materials are comprised of one potential well, as shown in Fig. 2.9 (a). MQWs, on the other hand, are comprised of multiple potential wells separated by multiple barriers. Moreover, the potential well in a

QW is typically thinner than in bulk materials, with quantum well and barrier thicknesses of 4–8 nm and 7–15 nm, respectively. If the thickness of the well is smaller than the De Broglie wavelength of the electrons and holes (which is proportional to the momentum of the electrons and holes), then the kinetic energies of the electrons are quantized in the wells [3]. The transition then happens between the different sub-bands of electrons and holes. The energy levels and therefore the bandgap can be engineered by controlling the width of the well.

However, light confinement in such a thin structure is an issue. Separate confinement heterostructures (SCHs) shown in Fig. 2.9 (b) are used to improve light confinement. Like quantum wells, SCHs have high refractive indices compared to the other surrounding materials, and thus by sandwiching the quantum wells, effective light confinement is achieved.
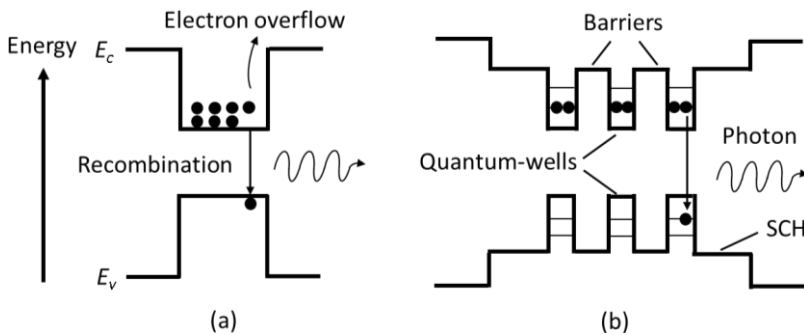

Figure 2.9: Band structures of InGaAsP (**a**) bulk and (**b**) multi quantum wells

2.3.5   Multi quantum wells for 1.3 and 1.55 μm

For telecommunication applications in the 1.3 and 1.55 μm windows, there are three widely used III-V MQW materials: (1) Indium-Gallium-Arsenide-Phosphide grown on an Indium-Phosphide substrate (InGaAsP/InP), (2) Indium-Gallium-Aluminum-Arsenide grown on an Indium-Phosphide substrate (InAlGaAs/InP), and (3) Gallium-Indium-Nitride-Arsenide grown on a Gallium-Arsenide substrate (GaInNAs/GaAs).

The first parameter to investigate is the energy or potential depth of the quantum wells. This indicates the uniformity and leakage of the electrons and holes during the injection. Since the mass of the electrons is much smaller than that of the holes, we normally focus more on the conduction band offset ΔE_c. Fig. 2.10 shows a comparison between the band structures of the three investigated materials. InAlGaAs has a higher conduction band offset (0.27 eV) compared to InGaAsP (0.1 eV), with GaInNAs having the highest one (0.4 eV). Large conduction band offset results in a better confinement effect on the injected electrons [4]. This is explained by the increased momentum that an electron needs to escape the potential well if the conduction band offset is high. This results in better temperature characteristics for GaInNAs and InAlGaAs, due to the reduction of electron current leakage. Electron current leakage is the dominant form of leakage

in comparison to hole current leakage, due to the higher electron mobility. Low electron leakage and high electron uniformity are desired to get a high gain.
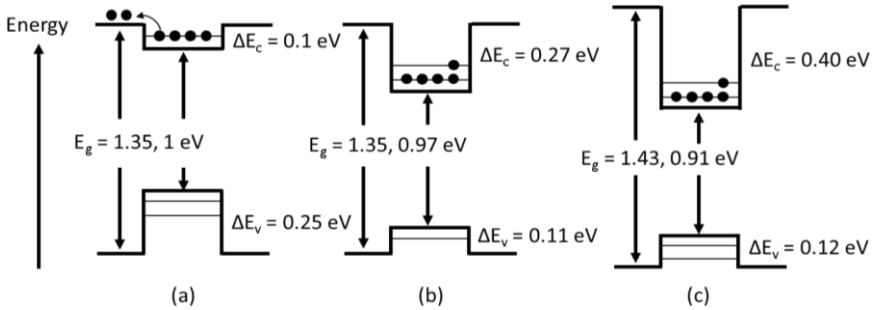
Figure 2.10: Band structures showing the conduction and valence band offsets (ΔEc, ΔEv) of (**a**) InGaAsP/InP, (**b**) InAlGaAs/InP, and (**c**) GaInNAs/GaAs quantum wells [4]

The second parameter to discuss is the characteristic temperature T_o, a figure of merit for the temperature stability. This is defined by the empirical expression in (2.5), where $I_{th}(T)$ is the threshold current at a certain absolute temperature T. One of the parameters that the characteristic temperature depends on is the conduction band offset ΔE_c [5]. Fig. 2.11 shows a comparison between the characteristic temperatures of the three aforementioned materials [5]. GaInNAs proves to be the best in terms of temperature stability. However, it is very difficult to extend its emission wavelength beyond 1.3 μm while also maintaining good laser properties. Both InGaAsP and InAlGaAs operate well in the 1.3 and 1.55 μm windows, with the temperature stability of InAlGaAs being higher than that of InGaAsP due to the higher conduction band offset ΔE_c [5].

$$I_{th}(T) = I_{th}(0)\, e^{\frac{T}{T_0}} \tag{2.5}$$

Figure 2.11: The characteristic temperature T_o versus the conduction band offset ΔE_c showing the outstanding temperature stability in GaInNAs [5]

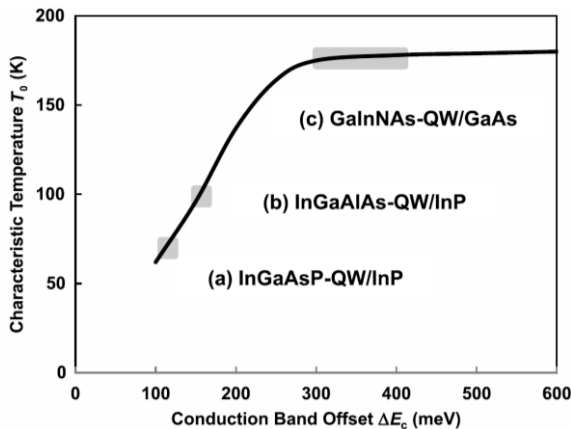To sum up, GaInNAs shows the best performance among the three MQW materials. However, it is difficult to extend its emission wavelength beyond 1.3 μm. Both InGaAsP and InAlGaAs are mature in terms of production [4]. InAlGaAs seems to be the most suitable material: due to its deep wells, and high characteristic temperature T_o. Special care should be taken during the fabrication of InAlGaAs, due to the oxidization of aluminum, which can create trap states.

2.4   DFB laser diodes

This section discusses the operation and structure of distributed feedback (DFB) lasers, by comparing them to the structure of the most basic type of laser: the Fabry-Perot laser.

2.4.1   Fabry-Perot laser diodes

The very basic type of laser is the Fabry-Perot (FP) laser. The laser consists of an active medium to provide optical gain and two highly reflective mirrors on each end to provide optical feedback. The optical output can be taken from either side by slightly reducing the reflectivity of its mirror.

Fig. 2.12 (a) shows the structure and operation of a FP laser. The laser has a multimode behaviour, because (1) many modes are supported by the cavity, and (2) many modes have enough gain to resonate. The wavelength of the supported FP modes λ that satisfies the phase condition for constructive interference is dependent on the cavity length L, as given by:

$$m\lambda = 2L\, n_e \tag{2.5}$$

where n_e is the effective index of the waveguide, $2L$ is the roundtrip distance, and m is an integer number. Based on (2.5), the separation between two modes referred to as the free spectral range (FSR) $\Delta\lambda_{FSR}$, can be defined by (2.6), where n_g is the group index.

$$\Delta\lambda_{FSR} = \frac{\lambda^2}{2L\, n_g} \tag{2.6}$$

In optical communication, and for the use of Dense Wavelength-Division multiplexing (DWDM), only one wavelength per channel is permitted. Therefore, single-mode lasers are preferred. As mentioned earlier, to make a single-mode FP laser, the separation between the two modes in Fig. 2.12 (a) needs to be very large, such that only one mode falls under the gain spectrum. From (2.6), a large FSR requires a short cavity. However, a short cavity may not be able to provide enough optical gain unless the reflections are high. Therefore, a FP laser is not a good candidate for use in an optical communication system. In contrast, DFB laser diodes fulfill the requirements of single mode operation and are thus a strong candidate for DWDM.
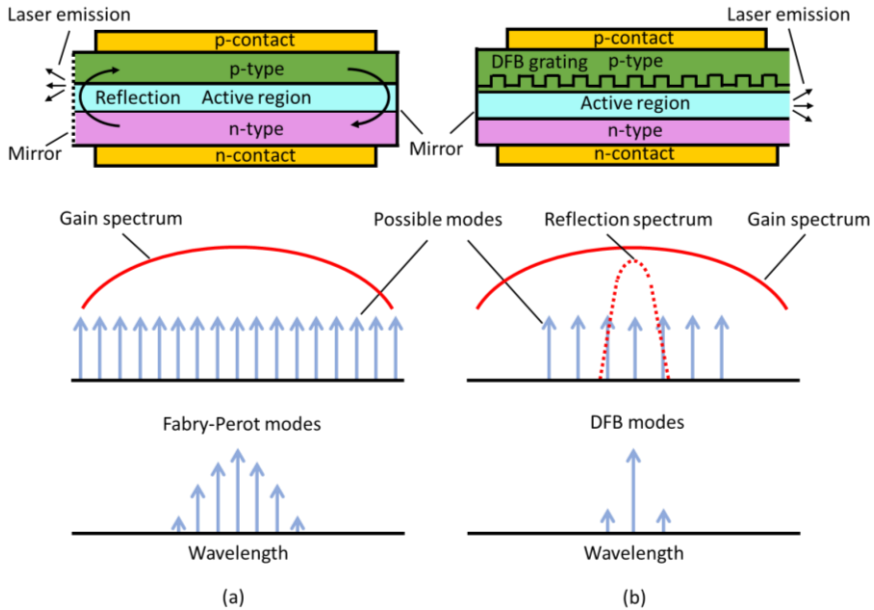
Figure 2.12: The structure, simplified operation and spectrum of (**a**) Fabry-Perot and (**b**) DFB lasers.

2.4.2 DFB laser diodes

DFB lasers were first proposed in [6–7], first optically [8–9] and then electrically pumped [10–11]. They are popular for a number of reasons. First, their ease of fabrication, due to the grating being on top of the active region. Additionally, their stable single-mode behavior, and their high side-mode suppression ratio (SMSR) make them the preferred optical source for optical communication. DFB lasers with more than 45 dB SMSR were demonstrated [12], indicating high spectral purity. Moreover, they are made of a horizontal cavity (as opposed to the vertical cavity in VCSELs), which makes their integration with other components on-chip possible. To understand how a DFB laser works, a comparison between its operation, structure, and spectrum is made to that of a FP laser, as illustrated in Fig. 2.12 (b).

In a DFB laser, the FP mirrors are replaced by a periodic structure along the cavity. This periodic structure introduces a periodic change in the effective index, which causes partial (distributed) reflections at each index step in the cavity. These reflections create forward and backward propagating waves (feedback) that interfere constructively and destructively, depending on the wavelength. In some cases, one side is covered by a high reflective coating to increase the feedback into the laser.

The periodic structure used is the so-called DFB grating, shown in Fig. 2.12 (b). The period of the grating Λ is usually in the order of a few hundred

nanometers, and it defines the wavelength of operation, also called the Bragg wavelength λ_B, as given by (2.7). m is an integer number which defines the order of diffraction. For example, for $m = 1$, the grating is called a first order grating. Shifting the Bragg wavelength can be done by changing the period of the grating and/or the effective index n_e.

$$m\lambda_B = 2\,n_e\Lambda \qquad (2.7)$$
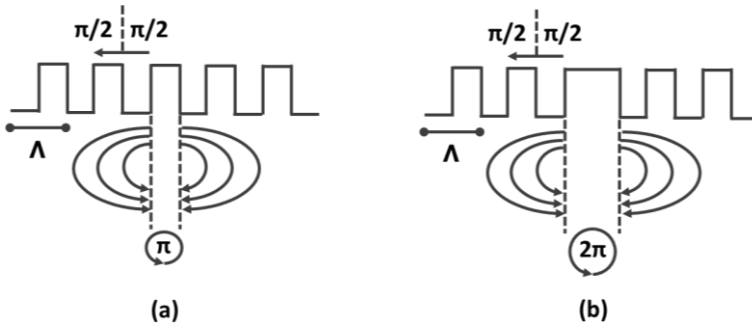
Figure 2.13: A π phase-shift in the middle grating in (**a**) prevents multiple of 2π round trip. Adding an extra $\lambda/4$ (π) phase shift in (**b**) solves this problem [13].
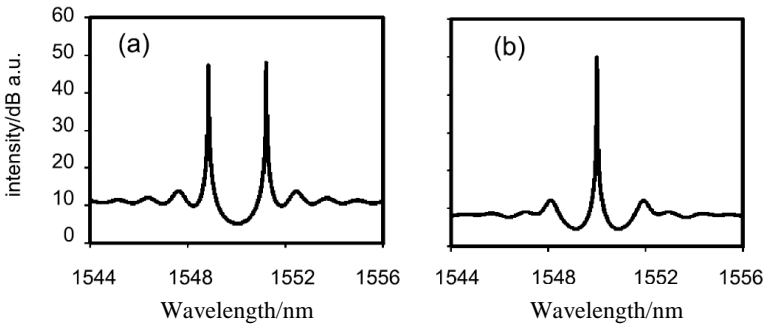
Figure 2.14: Spectra at threshold (**a**) without and (**b**) with $\lambda/4$ phase shift [3].

The DFB spectrum in Fig. 2.12 (b) was simplified. In reality, fabricating a grating like the one in Fig. 2.13 (a) [13] would result in two modes around the Bragg wavelength (Fig. 2.14 (a) [3]) (assuming anti-reflective coated facets). The two modes have the same intensity level due to having the same threshold gain. There is no mode at the Bragg wavelength because the roundtrip phase is not a multiple of 2π (due to the π phase shift in the middle). To ensure a single-mode behavior at the Bragg wavelength (Fig. 2.14 (b) [3]), a $\lambda/4$ phase shift is placed in the middle of the cavity, like the one in Fig. 2.13 (b). This introduces a π phase shift, which would make the roundtrip a multiple of 2π. Other higher order modes are visible at the edge of the spectrum in Fig. 2.14 (b), but they have a higher threshold gain than the main mode.

While adding a phase shift can help to obtain single-mode behavior, it results in a non-uniform power across the cavity, resulting in spatial hole burning. Some research suggests that introducing multiple phase shifts across the cavity helps to maintain a uniform power, which helps to obtain single-mode behavior [14–15].

2.5   III-V-on-silicon laser diodes

In the previous chapter, we discussed the heterogeneous III-V-on-silicon integration methods. Before these methods existed, devices such as laser diodes were made using only III-V materials, and were referred to as monolithic III-V laser diodes. These were fabricated and used for many years before III-V-on-silicon laser diodes. While III-V-on-silicon can use the advantages of silicon such as high volume production at low cost, the technology to fabricate monolithic III-V laser diodes remains more mature.

In the previous section, we have discussed the operation and structure of FP and DFB laser diodes. There are however other common types of laser diodes. For example, vertical-cavity surface-emitting lasers (VCSELs), and distributed Bragg reflector (DBR) lasers. In this section, we briefly describe these, while placing all four types of lasers in the context of heterogeneously integrated III-V-on-silicon lasers, as shown in Fig. 2.15.

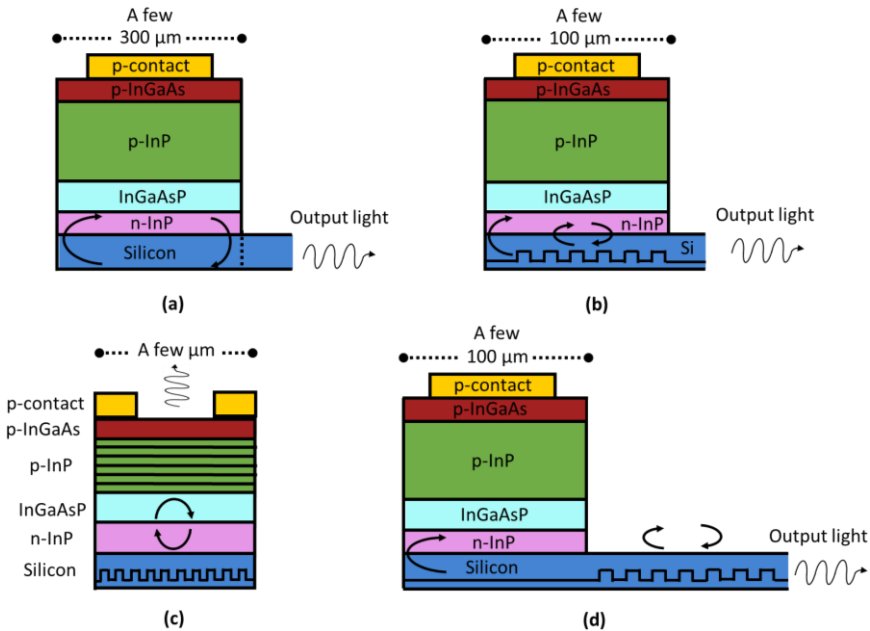**Figure 2.15:** Most common types of heterogeneously integrated III-V-on-silicon lasers, (**a**) Fabry Perot laser, (**b**) Distributed feedback laser, (**c**) Vertical-cavity surface-emitting laser, and (**d**) Distributed Bragg reflector laser.

The difference between the FP and the DFB laser in 2.12 (a, b) and 2.15 (a, b) is the presence of the grating in the silicon. This introduces a compromise between having a high gain (if the optical mode is confined to the active region) and a high reflection (if the optical mode is confined to the grating region). In both the FP and the DFB laser shown in Fig. 2.15 (a, b), a highly reflective mirror is placed on the left side, to increase the optical feedback into the cavity.

Fig. 2.15 (c) shows the schematic of VCSELs, very common type of lasers in data centers. They are very popular and attractive due to their very low threshold currents, and high power efficiency. As shown in Fig. 2.15 (c), and as suggested by the name, the laser is a vertical resonator. In the configuration shown in Fig. 2.15 (c), highly reflective mirrors are placed both on the top and on the bottom of the cavity. As VCSELs emit light vertically, they are not well suited for integration with other components in a photonic integrated circuit. VCSELs also used to have lower SMSR than DFB lasers, but nowadays there are demonstrations with more than 30 and 50 dB SMSR [16–17].

Finally, Fig. 2.15 (d) shows DBR laser diodes, which are similar to DFBs. However, the gratings are now present outside of the active region. This type of grating is useful for wavelength tuning.

There have been many III-V-on-silicon laser diode demonstrations in the past years. For example, transmission of 10 Gbps using microdisk lasers [18]. There were also demonstrations of direct and electro-absorption modulation of DFB lasers with modulation speed of 56 Gbps [19]. Wavelength tunable DFB lasers with tuning range of 8 nm were also demonstrated [20]. Mode-locked lasers with repetition rates of 1 GHz were reported in [21]. Quantum dot DFB lasers operating at 1.3 µm with continuous wave lasing up to 100°C were also recently reported in [22]. Finally, VCSELs operating at 850 nm and with a modulation speed of 25 Gbps were also demonstrated [16].

2.6 Monolithic versus heterogeneous III-V-on-Si

As already discussed in chapter 1, state of the art monolithic III-V devices have superior performance over III-V-on-silicon devices. This is because such devices have been around for longer, so the technology is more mature. Hereunder, we briefly show the driver for III-V-on-silicon integration, but also discuss the challenges.

2.6.1 Index contrast and optical confinement

The refractive index contrast Δn betweem the core and cladding of the waveguide, and the optical confinement to the waveguide are two interrelated key factors to reduce the losses and create small footprint devices. For example, the index contrast between the core (silicon, $n = 3.5$) and cladding (silicon oxide, $n = 1.5$) in a silicon platform is around 2.0 at 1550 nm. This results in very strong optical confinement to the silicon waveguide, which allows low-loss compact

devices. This is not the case in monolithic III-V devices, where the index contrast in an InP/InGaAsP waveguide is below 0.5 at 1550 nm.

2.6.2   Grating coupling coefficient

The grating coupling coefficient κ is a measure of the coupling strength between the forward and backward propagating waves, and is given by [23]:

$$\kappa = 2 \left(\frac{n_{eff,unetched} - n_{eff,etched}}{\lambda_B} \right) \sin(m\pi D) \tag{2.8}$$

where $n_{eff, unetched}$ and $n_{eff, etched}$ are the effective indices in the unetched and etched regions of the grating, respectively, and D is the grating duty cycle. Due to the high index contrast in III-V-on-silicon devices compared to the monolithic ones, κ is higher. In monolithic III-V devices, κ can be in the order of 150 cm^{-1} [24], while it can be as high as 1500 cm^{-1} for III-V-on-silicon [25].

The grating coupling coefficient influences the direct modulation bandwidth. For example, in a DFB laser, the higher the overlap between the light and the grating, the higher the feedback, the lower the threshold current, and the higher the modulation bandwidth. This is governed by:

$$(2\pi f_r)^2 = \Gamma \frac{dG}{dN} \frac{(I - I_{th})}{qdwL} \tag{2.9}$$

where f_r is the relaxation oscillation frequency, Γ is the optical confinement factor, dG/dN is the differential gain, I and I_{th} are the injected and threshold current, respectively, q is the elementary charge, d, w, and L are the thickness, width, and length of the active region.
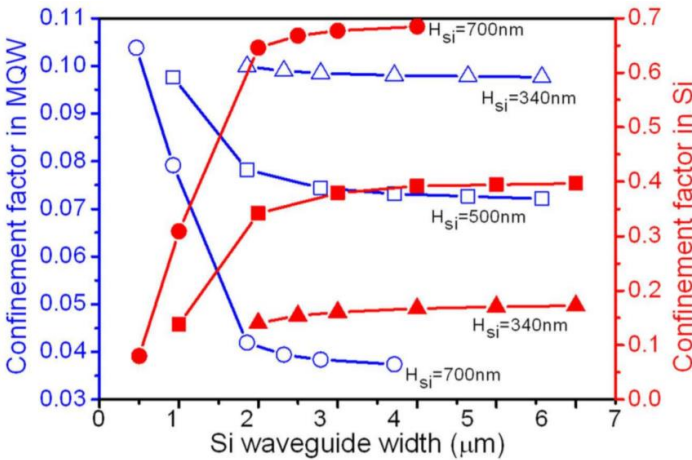

Figure 2.16: Confinement factor to the MQW (blue, hollow) and to the silicon waveguide (red, bald) as a function of the silicon waveguide width and thickness (figure from [26]).

Although a high coupling coefficient is desired by confining the light to the grating layer, confinement to the gain region is important to get enough optical gain. In a III-V-on-silicon laser, the confinement factor to the MQW and the silicon waveguide can be tuned by e.g. changing the silicon waveguide width, as illustrated in Fig. 2.16 [26]. There, a compromise must be sought between optical gain and feedback.

The internal loss of a laser is another important parameter to take into account when designing the optical confinement factor. To understand this, let's introduce the internal quantum efficiency η of a laser, which is proportional to the internal loss α_0 and the mirror (i.e. grating) loss α_{mirror}, as given by:

$$\eta \sim \frac{\alpha_{mirror}}{\alpha_0 + \alpha_{mirror}} \tag{2.10}$$

There are different mechanisms responsible for the internal loss. The first mechanism is scattering loss on the sidewalls of the III-V, which is mainly due to the fabrication. Another mechanism is the intervalence band absorption (IVBA), in which an emitted photon is reabsorbed by an electron transitioning between two valence sub-bands. The third mechanism is metal absorption. As metal contacts absorb light, they should be placed sufficiently far from the optical mode. However, metal contacts need to be as close as possible to decrease the series resistance.

We have shown that if the light is confined in III-V waveguides, it undergoes different internal loss mechanisms. The optical losses in silicon waveguides, on the other hand, are very low. Therefore, a compromise between optical gain in III-V waveguides and low loss in silicon waveguides is sought.

2.6.3 Thermal challenges

There remains one main challenge for demonstrated III-V-on-silicon devices: heating. In such devices, a layer of 10–100 nm of divinylsiloxane-bis-benzocyclobutene (DVS-BCB), or BCB for short, is used to bond the III-V to the SOI. The SOI consists of a 2 µm thick buried oxide (BOX) layer, which sits below the 400 nm silicon waveguide. Both are carried on a thick silicon substrate layer, as shown in the cross section in Fig. 2.17. The thermal conductivities for these materials are 1.1 and 0.3 W/m·K, respectively, which are poor. Therefore, they prevent heat from sinking into the silicon substrate. On the other hand, as there is no BCB or buried oxide layer in monolithic InP devices, the heat can leak more easily into the InP substrate, which has a thermal conductivity of 68 W/m·K.

The effect of heating is evident, especially in short III-V-on-silicon devices. Heating can limit the maximum output optical power. Our most power efficient laser [27] still has lower output optical power compared to the monolithic laser in [28] (2.9 versus 4.5 mW at I = 35 mA). This is the case even though the laser in [28] is three-fold shorter than the one in [27] (50 versus 150 µm), which normally causes faster thermal roll-off.
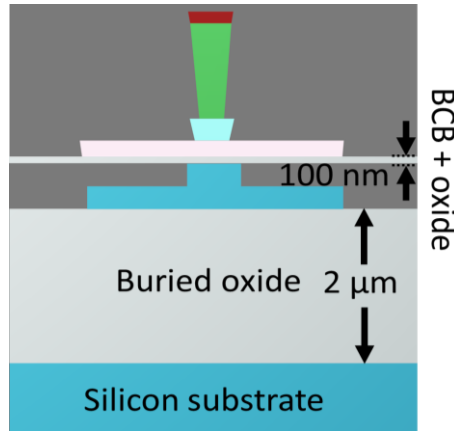
Figure 2.17: Cross section of the laser structure showing possible heat sink challenges due to the thick buried oxide layer

2.7 Fabrication of III-V-on-silicon DFB laser diodes

2.7.1 Process flow

For a good understanding of this work, the technology behind the presented devices needs to be discussed. As discussed in chapter 1, the potential of silicon photonics for high volume production at low cost makes it attractive for commercial applications. However, efficient light generation cannot be achieved using only silicon, due to its indirect bandgap [29]. The need for light sources on silicon has triggered an extensive investigation of III-V-on-silicon integration [1]. The technology of such a platform is based on integrating III-V epitaxial layer structures on top of patterned SOI waveguide circuits. As discussed in chapter 1, adhesive bonding relaxes the cleanliness requirements compared to direct bonding, solves the issue of the lattice mismatch in hetero-epitaxial growth, and allows high density integration compared to the flip-chip technique. Therefore, adhesive bonding is the technique of choice in this work.

The fabrication procedure is standard and well established in the photonics research group [12, 20, 30]. The SOI fabrication normally takes place at IMEC (e.g. the devices shown in chapter 3). We can also fabricate SOI circuits ourselves using electron beam lithography (e-beam or EBL) at Ghent University (e.g. the devices shown in chapter 4). The silicon waveguides and gratings are patterned on a 400 nm thick silicon wafer, with a 180 nm etch step. Bonding and post-processing took place in our cleanroom facilities. The process flow is illustrated in the schematic in Fig. 2.18 (a–i). The fabrication starts by bonding an InP-based die (7 mm^2) comprising the epitaxial layer structure epi-side-down onto an SOI die (2 cm^2), as shown in Fig. 2.15 (a, b). The typically used adhesive bonding agent to 'glue' the epi die on top of the SOI is BCB. Given that the SOI surface does not contain particles of the size of the bonding layer (10–100 nm), a bonding yield close to 100% can be achieved.
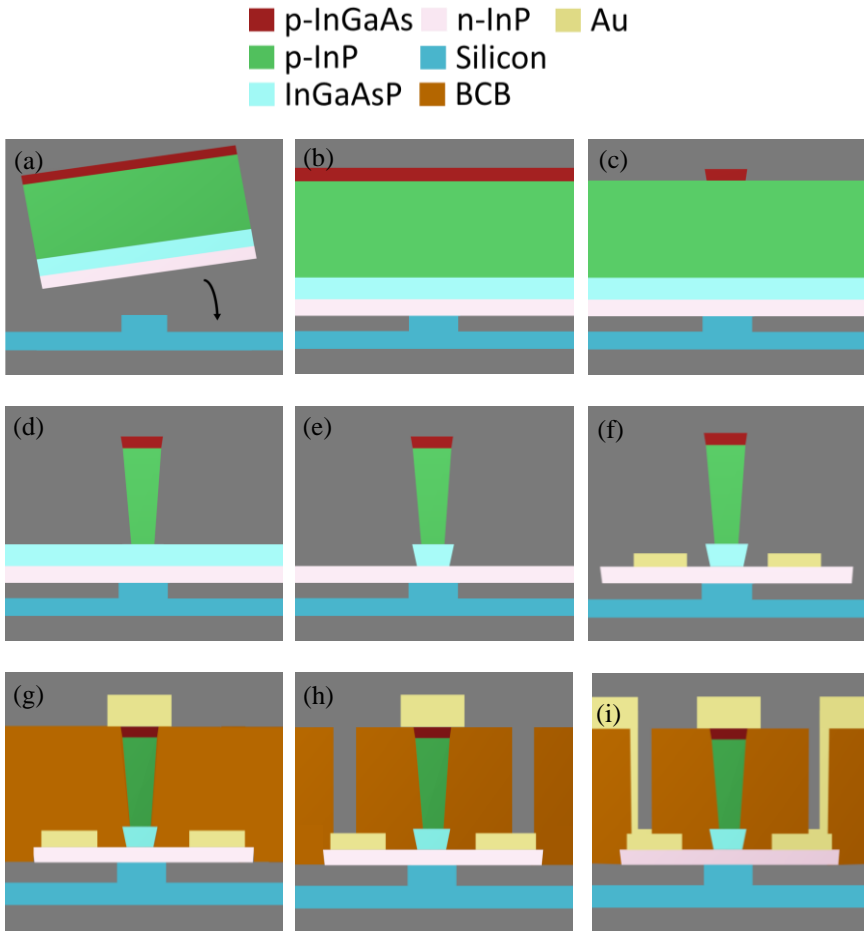
Figure 2.18: Cross-section schematic summarizing the process flow, starting from (**a, b**) bonding, going through (**c–f**) etching the different layers, (**g**) BCB planarization, (**h**) etching the openings (vias), and finally ending with (**i**) contact pads deposition.

After bonding, the layers are etched one after another, to create the pattern shown in Fig. 2.18 (f). This is done using a few iterations of Silicon Nitride (SiN) deposition and photolithography to create hard masks (SiN) and soft masks (photoresists), in combination with some steps of dry and wet etching. First, the thick InP substrate (not shown) is removed, using HCl:H$_2$O (1:3). Then, the p-InGaAs layer is etched using inductively coupled plasma (ICP) dry etching, as shown in Fig. 2.18 (c). Then, the p-InP layer is etched using HCl:H$_2$O (1:1), as shown in Fig. 2.18 (d). After that, the InGaAsP layer is etched using a combination of ICP and H$_2$SO$_4$:H$_2$O$_2$:H$_2$O (1:1:20), as shown in Fig. 2.18 (e). Care should be taken to remove the whole InGaAsP layer and reach a clean n-InP interface, to have a successful n-contact metal deposition. Finally, the n-InP layer is etched using HCl:H$_2$O (1:1) to create the island shown in Fig. 2.18 (f), to separate different devices and to open the grating couplers. N-contacts containing

Ni:Ge:Au (30 nm : 20 nm : 50 nm) are deposited at this step on the n-InP, as shown in Fig. 2.18 (f).

Once the devices are patterned, planarization using SiN and BCB is done. The BCB is etched back to the level of the first layer (p-InGaAs). Then, p-contacts are deposited, as shown in Fig. 2.18 (g). These consist of Ti:Au (40 nm:150 nm). Once that is done, openings (vias) through the BCB are patterned and etched by reactive ion etching (RIE), as shown in Fig. 2.18 (h). In the end, final metal contact pads that connect to the n- and p-contacts are deposited, as shown in Fig. 2.18 (i). The 3D view of the device is shown in Fig. 2.19, without showing the BCB and final contacts for simplicity.
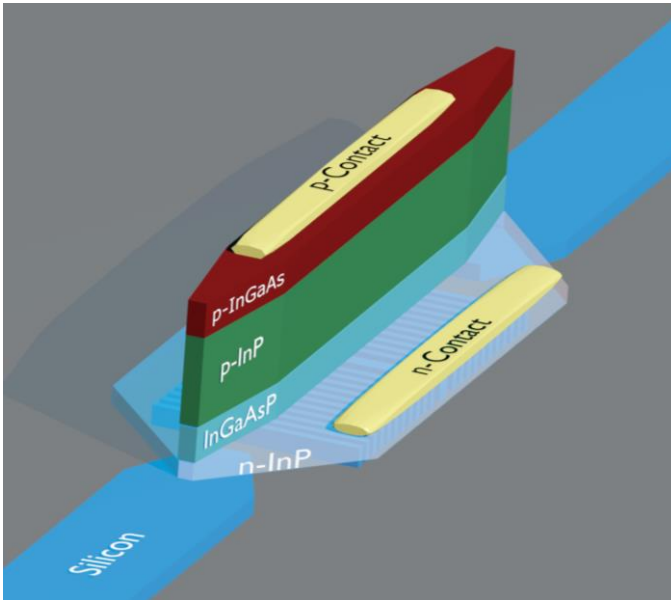
Figure 2.19: Schematic showing the 3D view of the laser structure.

The top view of an actual working device, as well as a cross section image using a scanning electron microscope (SEM) and focused ion beam (FIB) are shown in Fig. 2.20 (a, b). By largely removing the planarizing oxide on top of the silicon, a very thin bonding layer of around 10 nm is obtained. It is important to point out that the V-shape in Fig. 2.18 (f), and in Fig. 2.20 (b) is a result of the crystal orientation dependent wet-etching of p-InP, which gives an angle to the structure. Fortunately, this helps with the optical confinement in the III-V/silicon waveguide. The unfortunate mistake of a 90° rotation of the III-V sample before bonding would result in a pyramid shape crystal etching, which would result in lower optical confinement and poor performance. It is also worth mentioning that there are two sacrificial layers (not shown) on both sides of the epi, to protect the layers from contamination. These are required to be removed directly before fabrication.

Figure 2.20: Schematic showing (**a**) the top view and (**b**) the cross section image of an actual device using SEM and FIB.
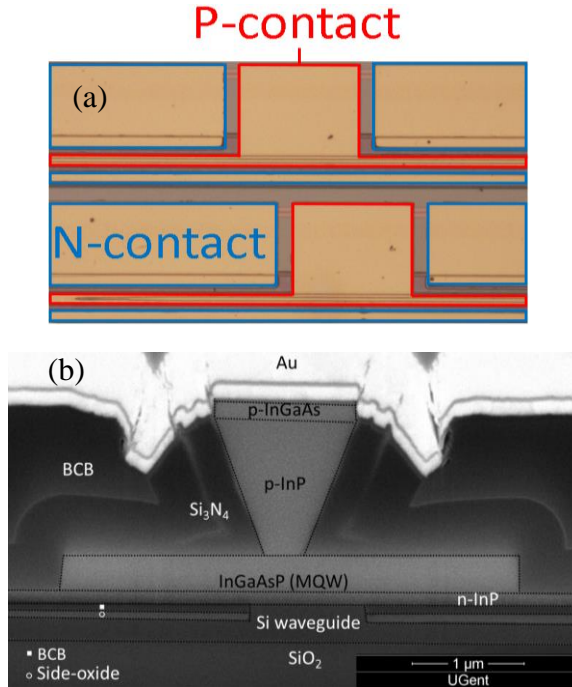
Moreover, it is noticeable that in the actual device (Fig. 2.20 (b)), the quantum wells are wide, unlike in the schematic in Fig. 2.18 (e). Both wide and narrow quantum wells have advantages and disadvantages. The wide quantum wells are useful to reduce the surface recombination at the side walls in case of InGaAsP quantum wells. In case of InAlGaAs, wide quantum wells are useful to reduce the optical losses caused by the oxidation of the side-walls. No surface treatment is required for wide quantum wells, which makes the fabrication easier. The disadvantage is the increased device volume, which increases the threshold current and reduces the modulation bandwidth.

On the other hand, narrow quantum wells are advantageous because they reduce the device volume, which decreases the threshold current and increases the modulation bandwidth. However, in aluminium-containing quantum wells, it is essential for the side walls to be carefully treated.

Wide InGaAsP layers consisting of six QWs are used in chapter 3 to investigate two-section lasers, due to the ease of fabrication. On the other hand, narrow InAlGaAs layers consisting of eight QWs are used in chapter 4, because they have more QWs and a higher conduction band offset.

2.7.2   Optical design and fabrication issues

To understand the operation of our DFB laser diodes, it is essential to look at the mode profile shown in the cross section in Fig. 2.21. This shows a hybrid mode between the silicon and the III-V waveguides. The optical mode is defined by the effective index n_{eff} of the waveguide structure. This optical mode experiences both optical feedback (DFB gratings) and optical gain (quantum wells), but also optical loss due to e.g. sidewall roughness. Using double adiabatic tapers (i.e. both in the III-V and in the silicon waveguides), the optical mode shown in Fig. 2.21 (in the middle of the taper) can be coupled down to the 400 nm thick silicon waveguide. The top and side views, along with the cross section are shown in Fig. 2.22 [31–33]. After coupling to the silicon waveguide, the light couples to an optical fiber using surface grating couplers.
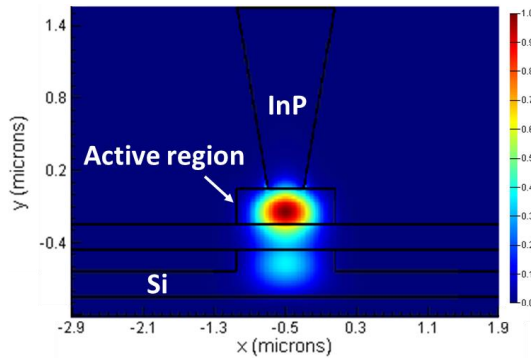

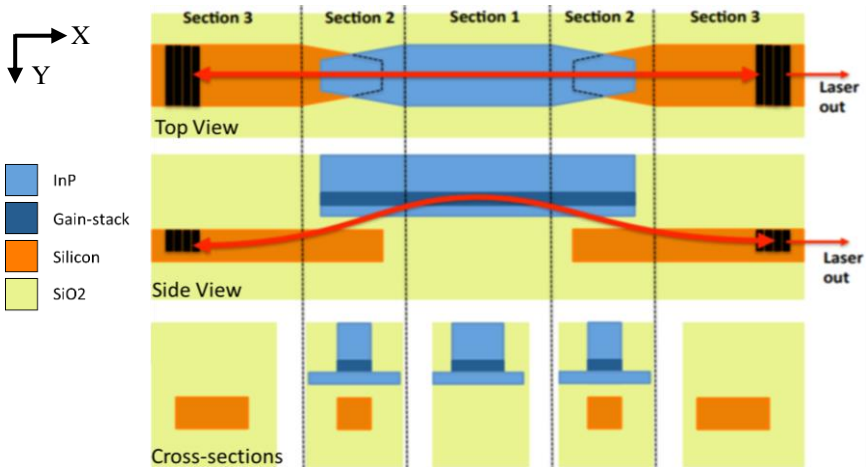**Figure 2.21:** The mode profile taking into account the V-shape

Figure 2.22: Double adiabatic tapers used to couple the light from the III-V waveguide to the silicon waveguide (figure from [31]).

The light confinement to the quantum well layer and to the silicon are referred to as the confinement factor Γ_{QW} and Γ_{Si}, respectively. The bonding thickness (10–100 nm) plays a role in determining these two quantities, and thus determining the performance of the device, as shown in Fig. 2.23 [12] for a rectangular III-V mesa. Large BCB thickness results in high confinement to the MQW, while small BCB thickness results in high confinement to the silicon waveguide.
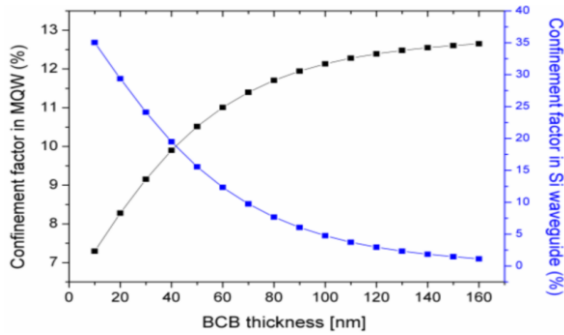
Figure 2.23: Simulation showing the confinement factor in the quantum well Γ_{QW} and in the silicon waveguides Γ_{Si} versus the BCB bonding thickness (figure from [12]).

The quality of the taper (in Fig. 2.24), especially at the tip, is very important for maximum light coupling from the III-V to the silicon waveguides. A good taper looks like the one in Fig. 2.24 (a), where the colors are uniform. Throughout the fabrication process, tapers can be damaged, bent or split (Fig. 2.24 (b–d)), or even completely peeled off. This is usually a result of issues in the lithography and etching processes.
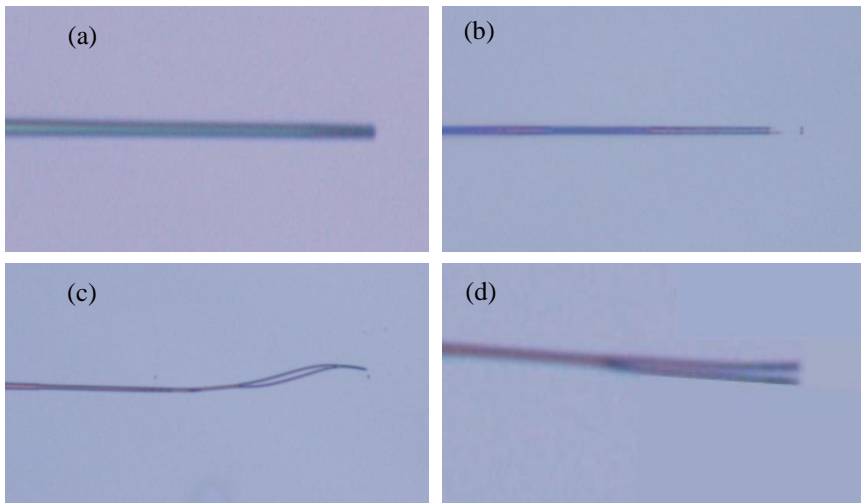
Figure 2.24: Microscopic image showing (**a**) a good taper with uniform colors, (**b**) a damaged taper, (**c**) a bent taper, and (**d**) a split taper.
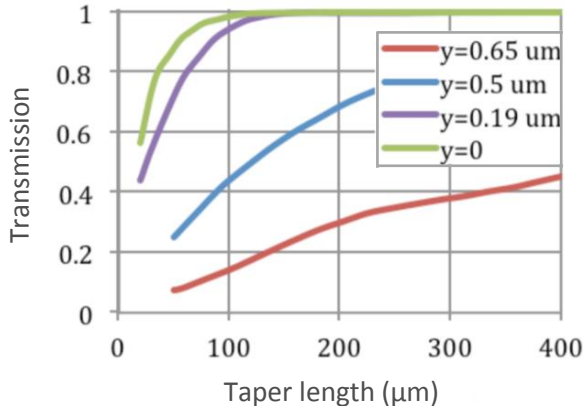
Figure 2.25: Simulation showing the effect of taper misalignment on the optical output power for different taper lengths with a 500 nm taper tip and 80 nm bonding thickness (figure from [32]).

Taper damage is not the only concern during fabrication. Lateral misalignment between the III-V and the silicon waveguides is a challenging parameter to control during fabrication. A misalignment of around 200 – 300 nm is common during the optical lithography process. The effect of this misalignment is illustrated in the simulation in Fig. 2.25 [32], by showing the transmission as a function of the taper length for different misalignment values (denoted as y). This was done for a taper tip width of 500 nm and bonding thickness of 80 nm. High misalignment results in lower optical output power, especially for short taper lengths. Moreover, there is an ongoing work to minimize the effect of misalignment and allow up to 1 µm alignment tolerance using a novel taper design, while still being compact (225 µm) by [34].

Throughout the thesis, a taper length of 180 µm is often used. However, Fig. 2.25 predicts that for a bonding thickness of 80 nm and a misalignment of 190 nm, it is possible to get 100% transmission for a taper length of less than 150 µm. This is attempted in chapter 4, where a 150 µm taper is fabricated for electro-absorption modulation.

2.8   III-V epitaxial layer structures used in this work

Three epitaxial layer structures were used in this work. The first one has an active medium of InGaAsP (6 quantum wells), and is used in chapter 3. The second one has an active medium of InAlGaAs (8 quantum wells), and is used in chapter 4. The third one is similar to the second one, but it contains 10 InAlGaAs quantum wells instead of 8, and is used in chapter 5.

The InAlGaAs stacks were more suitable for the demonstration of high-speed electro-absorption modulated DFB laser diodes (chapter 4) due to their superior performance compared to InGaAsP (as discussed in section 2.3), and the higher number of quantum wells.

On the other hand, the InGaAsP stack was used to develop new devices based on two-section laser structures (chapter 3), due to its ease of fabrication. The normalized photoluminescence spectrum of the InGaAsP (6 quantum wells) stack and the InAlGaAs (8 quantum wells) stack are shown in Fig. 2.26 (a, b). The parameters of the three layer stacks are summarized in Table 2.1–3.
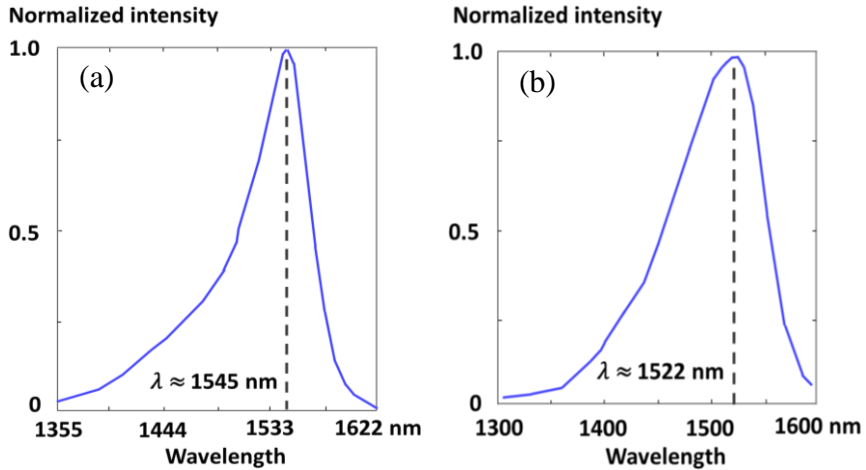
Figure 2.26: Normalized photoluminescence spectrum of (**a**) InGaAsP (6 quantum wells) and (**b**) InAlGaAs (8 quantum wells) epitaxial layer structure.

Table 2.1: InGaAsP/InP epitaxial layer structures used for the two-section DFB laser diodes in Chapter 3

Layer	Layer type	Periods	Material	PL wavelength (μm)	Thickness (nm)	Doping (cm⁻³)	Doping type
15	Sacrificial	-	InP	-	200	-	NID
14	Sacrificial	-	InGaAs	-	200	-	NID
13	n-cladding	-	InP	-	190	$1.0 \cdot 10^{18}$	n
12	SCH	-	InGaAsP	1.17	100	-	NID
11	MQW (well)	6	InGaAsP	1.55	7	-	NID
10	MQW (barrier)	7	InGaAsP	1.17	9	-	NID
9	SCH	-	InGaAsP	-	100	-	NID
8	p-cladding	-	InP	-	500	$5.0 \cdot 10^{17}$	p
7	p-cladding	-	InP	-	1000	$2.0 -> 5.0 \cdot 10^{17}$	p
6	Transition	-	InGaAsP	-	10	$> 3.0 \cdot 10^{18}$	p
5	Transition	-	InGaAsP	-	10	$> 3.0 \cdot 10^{18}$	p
4	p-contact	-	InGaAs	-	200	$> 1.5 \cdot 10^{19}$	p
3	Sacrificial	-	InP	-	200	-	NID
2	Etch-stop	-	InGaAs	-	200	-	NID
1	-	-	InP	-	50	-	NID
Substrate	-	-	InP	-	-	-	NID

Table 2.2: InGaAlAs/InP epitaxial layer structures used for the electro-absorption modulated DFB laser diodes in Chapter 4

Layer	Layer type	Periods	Material	PL wavelength (μm)	Thickness (nm)	Doping (cm⁻³)	Doping type
14	Sacrificial	-	InP	-	10	$1.5 \cdot 10^{18}$	n
13	Sacrificial	2	InP	-	7.5	$1.5 \cdot 10^{18}$	n
12	Sacrificial	2	InGaAsP	1.17	7.5	$1.5 \cdot 10^{18}$	n
11	n-cladding	-	InP	-	200	$1.5 \cdot 10^{18}$	n
10	SCH	-	InGaAsP	1.17	50	$0.0 \sim > 1.5 \cdot 10^{18}$	n
9	MQW (well)	8	InGaAlAs	1.5xx	8	-	NID
8	MQW (barrier)	9	InGaAlAs	1.10	10	-	NID
7	SCH	-	InGaAsP	1.17	50	-	NID
6	p-cladding	-	InP	-	2000	$1.0 - > 1.5 \cdot 10^{18}$	P
5	Transition	-	InGaAsP	1.17	20	$6.0 \cdot 10^{18}$	P
4	p-contact	-	InGaAs	-	200	$2.0 \cdot 10^{19}$	p
3	Sacrificial	-	InP	-	300	-	NID
2	Etch-stop	-	InGaAs	-	300	-	NID
1	-	-	InP	-	50	-	NID
Substrate	-	-	InP	-	-	-	NID

Table 2.3: InGaAlAs epitaxial layer structures used for the compact DFB laser diodes in Chapter 5

Layer	Layer type	Periods	Material	PL wavelength (μm)	Thickness (nm)	Doping (cm^{-3})	Doping type
16	Sacrificial	-	InP	-	100	-	NID
15	Etch stop	-	InGaAs	-	100	-	NID
14	n-cladding	-	InP	-	150	$2.0 \cdot 10^{18}$	n
13	Interface layer	-	As-P	-	5	$2.0 \cdot 10^{18}$	n
12	Transition	-	InAlGaAs	-	25	$1.0 \cdot 10^{18}$	n
11	SCH	-	InAlGaAs	1.1x	25	-	NID
10	MQW (well)	10	InGaAlAs	1.5xx	6	-	NID
9	MQW (barrier)	11	InGaAlAs	1.1x	10	-	NID
8	SCH	-	InGaAlAs	1.1x	25	-	NID
7	Transition	-	InGaAsP	-	25	-	NID
6	p-cladding	-	InP	-	500	$5.0 \cdot 10^{17}$	p
5	p-cladding	-	InP	-	1000	$1.0 \cdot 10^{18}$	p
4	p-contact	-	InGaAs	-	100	$1.0 \cdot 10^{19}$	p
3	p-contact	-	InGaAs	-	100	$>1.0 \cdot 10^{19}$	p
2	Sacrificial	-	InP	-	150	-	NID
1	Etch-stop	-	InGaAs	-	150	-	NID
Substrate	-	-	InP	-	-	-	NID

2.9   Conclusion

In this chapter, the basic concepts of laser operation and fabrication were discussed. First, we have outlined the basics of DFB laser diodes. Then, monolithic III-V and heterogeneously integrated III-V-on-silicon laser diodes were described. After that, a comparison between different types of laser diodes was given. Finally, the fabrication procedure and the epitaxial layer structures used in this work were summarized.

References

[1] D. Liang and John E. Bowers, "Recent progress in lasers on silicon," Nature Photonics, 4, pp. 511–517, (2010).

[2] M. Isshiki and J. Wang, "Wide-Bandgap II-VI Semiconductors: Growth and Properties." In: S. Kasap and P. Capper, Springer Handbook of Electronic and Photonic Materials, (2017).

[3] N. Grote, M. Mohrle, and M. Ortsiefer, "Laser components," In: H. Venghaus, N. Grote, "Fiber Optic Communication: Key devices," Springer, (2017).

[4] X. Li, "Optoelectronic devices," Cambridge University Press, (2009).

[5] M. Kondow, K. Uomi, A. Niwa, T. Kitatani, S. Watahiki, and Y. Yazawa, "GaInNAs: A novel material for long-wavelength-range laser diodes with excellent high-temperature performance," Japanese Journal of Applied Physics, 35, pp. 1273–1275, (1996).

[6] H. Kogelnik and C. V. Shank. "Stimulated emission in a periodic structure," Applied Physics Letters, 18(4), pp. 152–154, (1971).

[7] H. Kogelnik and C. V. Shank, "Coupled-wave theory of distributed feedback lasers," Journal of Applied Physics, 43(5), pp. 2327–2335, (1972).

[8] M. Nakamura, A. Yariv, H. W. Yen, S. Somekh, and H. L. Garvin, "Optically pumped GaAs surface laser with corrugation feedback," Applied Physics Letters, 22(10), pp. 515–516, (1973).

[9] C. V. Shank, R. V. Schmidt, and B. I. Miller, "Double-heterostructure GaAs distributed-feedback laser," Applied Physics Letters, 25(4), pp. 200–201, (1974).

[10] D. R. Scifres, R. D. Burnham, and W. Streifer, "Distributed-feedback single heterojunction GaAs diode laser," Applied Physics Letters, 25(4), pp. 203–206, (1974).

[11] M. Nakamura, K. Aiki, J.Umeda, A. Yariv, H.W. Yen, and T.Morikawa, "GaAs- Ga1-x AlxAs double-heterostructure distributed-feedback diode lasers," Applied Physics Letters, 25(9), pp. 487–488, (1974).

[12] A. Abbasi, "High speed directly modulated III-V-on-Silicon DFB lasers," Doctoral thesis, Ghent University, (2016).

[13] G. Morthier and P. Vankwikelberge, "Handbook of distributed feedback laser diodes" Artech house, (2014).

[14] G. P. Agrawal, J. E. Geusic, and P. J. Anthony, "Distributed feedback lasers with multiple phase-shift regions," Applied Physics Letters, 53(3), pp. 178–179 (1988).

[15] Y. Shi, X. Chen, Y. Zhou, S. Li, L. Li, and Y. Feng, "Experimental demonstration of the three phase shifted DFB semiconductor laser based on Reconstruction-Equivalent-Chirp technique," Optics Express, 20(16), (2012).

[16] S. Kumari, "GaAs VCSEL Integration on SiN Waveguide Circuits: Design, Technology and Devices," Doctoral thesis, Ghent University, (2016).

[17] D. M. Kuchta, T. N. Huynh, F. E. Doany, L. Schares, C. W. Baks, C. Neumeyr, A. Daly, B. Kogel, J. Rosskopf, and M. Ortsiefer, "Error-free 56 Gb/s NRZ Modulation of a 1530-nm VCSEL Link," Journal of lightwave technology, 34(14), pp. 3275–3282, (2016).

[18] G. Morthier, T. Spuesens, P. Mechet, G. Roelkens, D. Van Thourhout, "InP microdisk lasers integrated on Si for Optical Interconnects," IEEE Journal of Selected Topics in Quantum Electronics , 21(6), p. 1500610, (2015).

[19] A. Abbasi, B. Moeneclaey, J. Verbist, X. Yin, J. Bauwelinck, G.-H. Duan, G. Roelkens, G. Morthier, "Direct and electro-absorption modulation of a III-V-on-silicon DFB laser at 56 Gbps," IEEE Journal of Selected Topics in Quantum Electronics, 23(6), p. 1501307, (2017).

[20] S. Dhoore, "Heterogeneously Integrated III-V-on-Silicon Wavelength-Tunable DFB and DBR Lasers," Doctoral thesis, Ghent University, (2018).

[21] K. Van Gasse, L. Bogaert, L. Breyne, J. Van Kerrebrouck, S. Dhoore, C. Op de Beeck, A. Katumba, C.Y. Wu, H. Li, J. Verbist, A. Rahim, A. Abbasi, B. Moeneclaey, Z. Wang, H. Chen, J. Van Campenhout, X. Yin, B. Kuyken, G. Morthier, J. Bauwelinck, G. Torfs, G. Roelkens, "Analog radio-over-fiber transceivers based on III-V-on-silicon photonics," IEEE Photonics Technology Letters, 30(21), pp.1818–1821, (2018).

[22] S. Uvin, S. Kumari, A. De Groote, S. Verstuyft, G. Lepage, P. Verheyen, J. Van Campenhout, G. Morthier, D. Van Thourhout, and G. Roelkens, "1.3 um InAs/GaAs quantum dot DFB laser integrated on a Si waveguide circuit by means of adhesive die-to-wafer bonding," Optics Express, 26(14), pp. 18302–18309, (2018).

[23] L. A. Coldren, S. W. Corzine, and M. L. Mashanovitch, Diode lasers and photonic integrated circuits, 218, (John Wiley & Sons, 2012).

[24] G. Zhao, J. Sun, Y. Xi, D. Gao, Q. Lu, and W. Guo, "Design and simulation of two-section DFB lasers with short active-section lengths," Optics Express, 24(10), pp. 10590–10598, (2016).

[25] S. Matsuo and T. Kakitsuka, "Low-operating-energydirectly modulated lasers for short-distance optical interconnects," Advances in Optics and Photonics 10(3), pp. 567–643, (2018).

[26] X. Luo, Y. Cao, J. Song, X. Hu, Y. Cheng, C. Li, C. Liu, T-Y. Liow, M. Yu, H. Wang, Q. J. Wang, P. G-Q Lo, "High-throughput multiple dies-to-wafer bonding technology and

III/V-on-Si hybrid lasers for heterogeneous integration of optoelectronic integrated circuits," Frontiers in Materials, 2(28), (2015).

[27] M. Shahin, J. Van Kerrebrouck, G. Roelkens, G. Morthier, "InP-on-Si DFB Laser Diode with Distributed Reflector for Improved Power Efficiency," European Conference on Integrated Optics (ECIO), (2019).

[28] Y. Matsui, R. Schatz, T. Pham, W. A. Ling, G. Carey, H. M. Daghighian, D. Adams, T. Sudo, and C. Roxlo, "55 GHz Bandwidth Distributed Reflector Laser," Journal of Lightwave Technology, 35(3), pp. 397–403, (2017).

[29] R. Soref, "The past, present, and future of silicon photonics," IEEE Journal of Selected Topics in Quantum Electronics, 12(6), pp. 1678–1687, (2006).

[30] G. Roelkens, A. Abbasi, P. Cardile, U.D. Dave, A. De Groote, Y. De Koninck, S. Dhoore, X. Fu, A. Gassenq, N. Hattasan, Q. Huang, S. Kumari, S. Keyvaninia, B. Kuyken, L. Li, P. Mechet, M. Muneeb, D. Sanchez, H. Shao, T. Spuesens, A. Subramanian, S. Uvin, M. Tassaert, K. Van Gasse, J. Verbist, R. Wang, Z. Wang, J. Zhang, J. Van Campenhout, Y. Xin, J. Bauwelinck, G. Morthier, R. Baets, D. Van Thourhout, "III-V-on-silicon photonic devices for optical communication and sensing," Photonics (invited), 2(3), pp. 969–1004, (2015).

[31] M. Lamponi, S. Keyvaninia, C. Jany, F. Poingt, F. Lelarge, G. de Valicourt, G. Roelkens, D. Van Thourhout, S. Messaoudene, J.M. Fedeli, G.H. Duan, "low-threshold heteroogeneously integrated InP/SOI laser with a double adiabatic taper coupler," Photonics Technoloy Letters, 24(1), pp. 76–78, (2012).

[32] D. Van Thourhout, S. Keyvaninia, G. Roelkens, M. Lamponi, F. Lelarge, J.-M. Fedeli, S. Messaoudene, G. D. Duan, "Optimization of taper structures for III-V on silicon lasers," International Conference on Solid State Devices and Materials, pp. 524–525, (2012).

[33] S. Dhoore, S. Uvin, D. Van Thourhout, G. Morthier, G. Roelkens, "Novel adiabatic tapered couplers for active III-V/SOI devices fabricated through transfer printing," Optics Express, 24(12), pp. 12976–12990, (2016).

[34] B. Haq, G. Roelkens, "Alignment-tolerant taper design for transfer printed III-V-on-Si devices," European Conference on Integrated Optics (ECIO), p. T.Po2.1, (2019).

Two-section DFB laser diodes

In this chapter, we report on the design, fabrication, and characterization of III-V-on-silicon two-section DFB laser diodes, and how their specific characteristics were employed for three different functions. These are: (1) self-pulsating lasers, (2) bandwidth-enhanced lasers, and (3) low-threshold lasers.

Contents

3.1 Introduction

A big part of this work is aimed at the development of heterogeneously integrated III-V-on-silicon two-section DFB laser diodes for different functions. This type of lasers is interesting because of the ability to bias the laser sections independently from the other. This leads to the possibility of controlling the lasing and reflection condition in each section, and use the device for different functions. The design, fabrication, and characterization of two-section lasers were first done for self-pulsating laser diodes. The beating of the laser lines, among other mechanisms, can be useful to generate an optical microwave carrier at a certain frequency determined by the beating laser lines. This can be used in microwave photonics, applied in e.g. radio-over-fiber systems. The same laser configuration with different biasing can be used for bandwidth enhancement of direct modulation of the equivalent standard single-section laser configuration, using the

photon-photon resonance. Finally, by biasing only one section, and using the other section as a reflector, the laser threshold and power consumption can be lowered. The experimental findings for each function are described in detail in the next sections.

Before that, it would be useful to point out the fabrication differences from the standard laser fabrication procedure summarized in chapter 2 [1–3]. Initially, the proposed devices are fabricated as a standard single-section DFB laser. Later, by the end of the fabrication process, an isolation etch takes place, by wet etching the top p-InGaAs contact layer using H_2SO_4:H_2O_2:H_2O (1:1:18), and dry etching 200–500 nm of the p-InP layer using ICP. Fig. 3.1 shows the top view of a 14 μm long etched electrical isolation between two laser sections with different III-V width (hereafter called mesa width). The devices presented in this chapter are based on the InGaAsP/InP epitaxial layer stack presented in chapter 2.
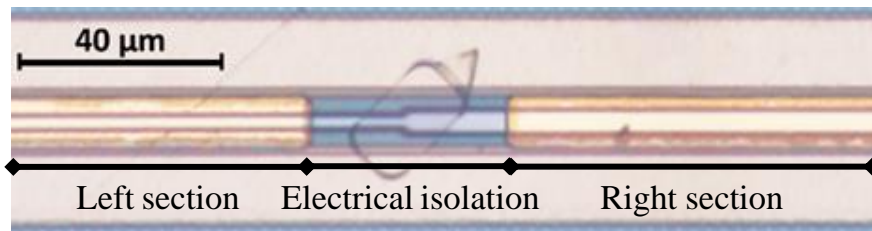

Figure 3.1: Top view of a two-section laser diode with different mesa widths, showing a 14 μm long electrical isolation

The laser diodes for each of the three functions will be discussed in the following three sections. Each time, the literature will be reviewed first, followed by the design parameters, and the experimental results. Finally, a summary of the research findings, and a comparison to the state of the art are given.

3.2   Self-pulsating DFB laser diodes

The increased importance of radio-over-fiber systems has triggered a lot of interest in optical microwave signals [4–5]. One way to generate such signals is by using self-pulsating laser diodes. In this section, we demonstrate self-pulsating two-section DFB laser diodes on the III-V-on-silicon platform. The chapter starts with a review of the literature and a discussion of the state of the art. Then, the design of the laser structure is discussed. After that, the static laser characteristics are shown, followed by the characteristics of the free-running (unlocked) self-pulsation. Finally, locking the self-pulsation to an external RF signal is discussed.

3.2.1 Literature review and state-of-the-art

Self-pulsating DFB laser diodes have been described in literature since the early 1990s. At that time, these were mainly used for all-optical clock extraction or recovery. Two-section DFB laser diodes for 5 GHz [6], 10 GHz [7], 20 GHz [8], and 40 GHz [9] clock recovery were successfully demonstrated. Theoretically, self-pulsations with repetition frequencies up to 200 GHz are theoretically possible [10], although it is challenging to experimentally verify. These demonstrations were all based on monolithic III-V laser diodes.

Nowadays, the increased importance of radio-over-fiber systems has generated a strong interest in the generation of optical microwave or millimeter wave carriers [4]. These are sinusoidal waves with a sub-nanosecond period. There are a few approaches for the generation of such optical signals: mode-locked lasers, self-pulsating lasers, and external modulation. Self-pulsating DFB lasers have the advantage that their repetition frequency is not fixed by the cavity length as in mode-locked lasers. The repetition frequency or frequency separation Δv between two modes in mode-locked lasers is given by:

$$\Delta v = \frac{c}{2L\,n_g} \tag{3.1}$$

where c is the speed of light, n_g is the group index of the laser mode, and L is the optical cavity length.

The repetition rate in mode-locked lasers is highly dependent on the optical cavity length. Obtaining a high repetition rate is easily done by fabricating a small laser. However, obtaining low repetition rates is more challenging, since a very long laser cavity is required. For example, a monolithic InP and a heterogeneously integrated InP-on-silicon mode-locked laser with repetition rates of 2.5 and 1 GHz, respectively, were demonstrated in [11–12]. However, the cavities were as long as 33 and 37.4 mm, respectively. Although long cavities are not desired, they are easy to achieve in silicon using spiral waveguides [12]. The real disadvantage here is that the repetition rates are fixed and cannot be changed.

On the other hand, the repetition rate in self-pulsating laser diodes does not depend on the cavity length. Also, the repetition rate can be continuously tuned as will be explained throughout this chapter. Both self-pulsating and mode-locked lasers can be locked to a weak RF signal. Using this locking, an optical RF signal with very narrow linewidth could be generated with minimal RF power [13]. Finally, direct and external modulation can also be used to generate such a signal. However, the bandwidth of direct modulation is limited, while external modulation adds an extra insertion loss and increases the complexity of the system.

DFB lasers that consist of two or three sections are common for the demonstration of self-pulsating lasers [14–16]. Self-pulsations are mainly

attributed to three mechanisms [17–18]: spatial hole burning, beating-type oscillations, and dispersive self-Q-switching.

Spatial hole burning refers to a perturbation in the carrier concentration. This mechanism was discussed several times in the literature [19–22]. The change in carrier concentration would induce a gain and refractive index difference throughout the laser. When the loss of the laser mode at a certain wavelength increases, mode hopping occurs. This means that another laser mode with less loss starts to operate. After some recovery time, the loss of the original mode decreases, and the laser hops back to the original mode. This repetition causes a train of pulses with a certain repetition rate. One noticeable effect of this mechanism is (longitudinal) multi-mode behavior. The repetition rate of self-pulsations due to spatial hole burning is limited by the relaxation oscillation frequency and is therefore limited to just several GHz [19].

The second mechanism for generating self-pulsations is to cause the beating of two laser modes [17]. This mechanism relies on simple beating between two DFB modes that are spectrally close to each other, to generate a beat frequency equal to the separation between the modes. High repetition frequencies up to 100 GHz were obtained in the literature [17].

The third mechanism is self-Q-switching [23–25]. In this case, the stop-bands of the two laser sections should overlap, such that one section acts as a reflector for the lasing mode of the other section. This is illustrated in Fig. 3.2 [17], in which the lasing wavelength of one section lies on the negative reflection slope of the other section. At this point, the threshold of the lasing mode is strongly dependent on the wavelength of operation, since the different wavelengths have different reflectivities at the negative slope. If the reflectivity is high, the photon density increases, while the carrier density decreases. This causes an increase in the refractive index which redshifts the lasing wavelength, and switches the laser off. When the laser is off, the photon density decreases, while the carrier density increases. This causes a decrease in the refractive index, which blueshifts the lasing wavelength, allowing the laser to operate again. The repetition of this process creates a train of short pulses.
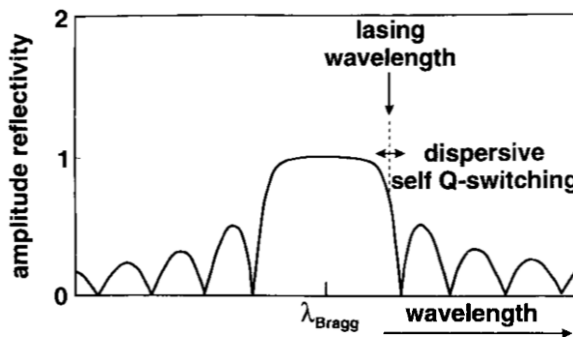

Figure 3.2: Illustration showing the self-Q-switching mechanism that happens when the lasing mode of one section lies on the negative reflection slope of the other section [17].

Table 3.1 summarizes the characteristics of each mechanism. Spatial-hole-burning oscillations are characterized by their multi-mode behavior, with limited pulsation frequencies. Beating is also characterized by its multi-mode behavior, but with the possibility of high pulsation frequencies. Finally, self-Q-switching is usually characterized by the overlapping of two stop-bands, single mode behavior, and the possibility of high repetition frequencies.

Table 3.1: Summary of self-pulsation mechanisms and their properties

Self-pulsation type	Mode	Frequencies	References
Spatial hole burning	Multi-mode	Low (< few GHz)	[19–21]
Beating	Multi-mode	High (> few GHz)	[18]
Self-Q-switching	Single-mode	High (> few GHz)	[17, 23–25]

So far, all reported self-pulsating laser diodes were implemented as monolithic III-V laser diodes. In this work, we report on the design, fabrication, and characterization of self-pulsating heterogeneously integrated III-V-on-SOI two-section DFB laser diodes. We demonstrate tunable repetition frequencies over a broad range by variation of current and temperature. Finally, we also report on the locking of the self-pulsation to a low power electrical RF signal, which can be used for the generation of optical microwave carriers with very narrow linewidth.

3.2.2 Design

In the beginning, we were aiming to exploit the self-Q-switching mechanism. For that, the proposed lasers require two sections with different Bragg wavelengths, which can be implemented through different modal effective indices. In principle, changing one parameter in one section compared to the other can induce such an effect. For example, the period of the grating or the mesa width of the III-V laser structure. We choose to design the two sections with different mesa widths [26], since the available SOI chips did not have DFBs with different grating periods within one laser cavity. If the widths are chosen correctly, the stop-bands of the two sections overlap. This has the potential to induce the self-Q-switching effect shown in Fig. 3.2. Fig. 3.3 (a–c) shows the 3D, top and side view of the proposed structure. The two sections are electrically isolated by etching the top p-InGaAs layer and part of the p-InP layer. Tuning the current into the laser sections can be used to shift the stop-bands.

We will investigate two laser devices (Laser A and laser B), with slightly different mesa widths. The mesa width for the right and left sections, respectively, are: Laser A: 4, 2 µm, Laser B: 4, 2.5 µm. The choice of these parameters was based on the optical mode simulation of the structure in Fig. 3.4 (a). This simulation shows the relationship between mesa width and effective index in Fig. 3.4 (b). For example, the choice of Laser A (4, 2 µm) would give $\Delta n_e \approx 0.01$. The difference between the Bragg wavelengths of the two sections $\Delta\lambda$ with grating period of Λ is given by:

$$\Delta\lambda = 2\Delta n_e \Lambda \tag{3.2}$$

For example, for $\Lambda = 240$ nm and $\Delta n_e \approx 0.02$, $\Delta\lambda \approx 4$ nm. Since the stop-bands of similar lasers were reported to be 4 nm [27–28], this design would make it possible for the stop-bands to overlap, which induces self-Q-switching. To gain an insight into the behavior of the laser with different parameters, Laser B, having slightly different mesa widths (4, 2.5 µm), is also investigated. The width of the quantum well, n-InP and silicon waveguide are 9, 50 and 1.75 µm, respectively.
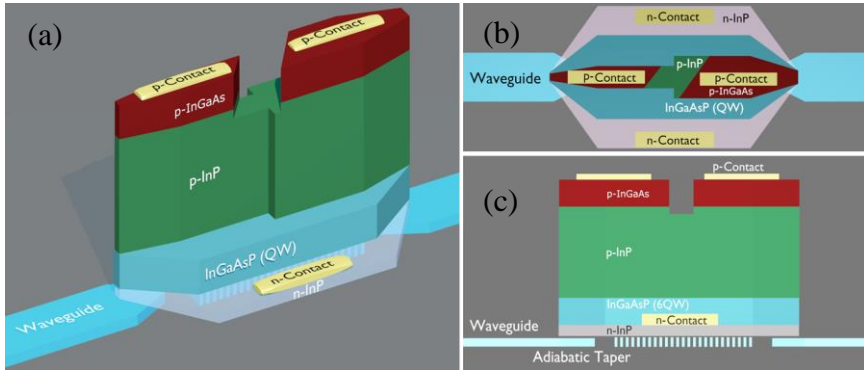

Figure 3.3: (**a**) 3D, (**b**) top, and (**c**) side view of a two-section DFB laser, with different mesa widths, electrically isolated by dry etching.
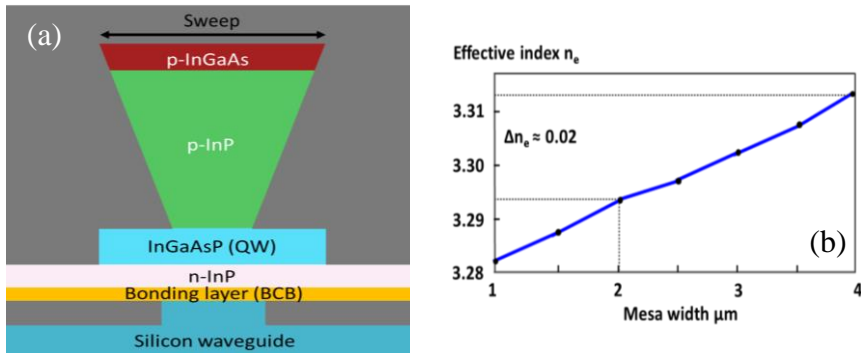

Figure 3.4: Optical mode simulation of the structure in (**a**), showing (**b**) the effective index versus the mesa width. $\Delta n_e \approx 0.02$ is estimated for Laser A with mesa widths (4, 2 µm).

The mesa width value in Fig. 3.4 refers to the mesa width at the top p-InGaAs layer. As previously discussed, the crystal dependent etching of p-InP gives an angle (V-shape) to the structure. Fig. 3.5 shows an SEM image of the cross section after using FIB of an actual laser structure.
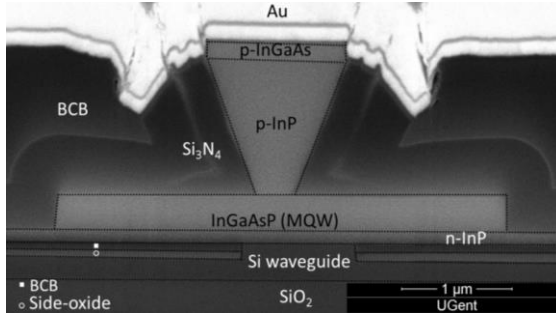
Figure 3.5: SEM image of the cross section of the fabricated device obtained using FIB, showing the V-shape caused by crystal orientation dependent p-InP wet etching.

In the proposed device, each section has a length of 460 μm. This includes a 230 μm long DFB section acting as a laser, and a 230 μm long pumped taper acting as an amplifier. The grating defined in the silicon waveguide layer is 180 nm etched, has a period of 240 nm, and has a duty cycle of 50%. Finally, a quarter-wave (λ/4) phase shift is placed in the middle of the cavity.

3.2.3 Static laser characteristics

The demonstrated lasers have a threshold current of 2×12 mA (i.e. 12 mA in each section). Fig. 3.6 shows the output power coupled out from the left grating coupler versus the current in the left section I_L (a) and in the right section I_R (b) for Laser B (Laser A shows a similar trend). The current into the other section is fixed at 10 or 50 mA. The series resistance is around 10 Ω, slightly lower (9 Ω) for the wider right section and slightly larger (11 Ω) for the narrower left section. The resistance between the two sections is measured to be 13 kΩ.

The illustrated power curves correspond to power measurements in the waveguide, extracted from the left grating coupler. The grating coupler loss is around 8 dB near 1550 nm. The grating coupler loss is determined by sending an optical signal at the desired wavelength over a straight waveguide with two grating couplers (input and output grating couplers). In Fig. 3.6 (a), the current is injected into the narrow left mesa section. Although lasing already occurs for $I_R = 50$ mA, the left section acts as a reflector/absorber, and no light is detected from the left grating coupler before biasing the left section. The lower threshold current in the red curve is attributed to the high current in the right section $I_R = 50$ mA.

Fig. 3.6 (b) shows different behavior. Since the light is detected from the left side, the optical power levels at low I_R values are already high for $I_L = 50$ mA, compared to $I_L = 10$ mA. It can also be seen that the blue curves show an upward trend in the optical power compared to the red curves under high injected currents. This can be associated with heating, due to high injected current, which decreases the output optical power.

To analyze the operation of such lasers, the first step is to run a two-dimensional sweep (i.e. to sweep I_R and I_L), to find the current combinations that allow self-

pulsation operation. This is done first for Laser B. In this case, we have found that at the current combination $I_L = 32$ mA and $I_R = 35$ mA, a self-pulsation signal at 40 GHz is generated (to be shown in the next section). The second step is to use these current combinations and plot the individual stop-band spectrum of each section. This is done by biasing one section close to threshold (12 mA), while the other section is biased at the respective self-pulsation current. For example, for the 40 GHz self-pulsation signal, the following current combinations are considered: (1) $I_L = 32$ mA, $I_R = 12$ mA and (2) $I_L = 12$ mA, $I_R = 35$ mA. Fig. 3.7 (a) shows the optical spectrum, where the 5 nm stop-bands of the right and left section (hereby denoted as SB_R and SB_L, respectively) are almost overlapping.
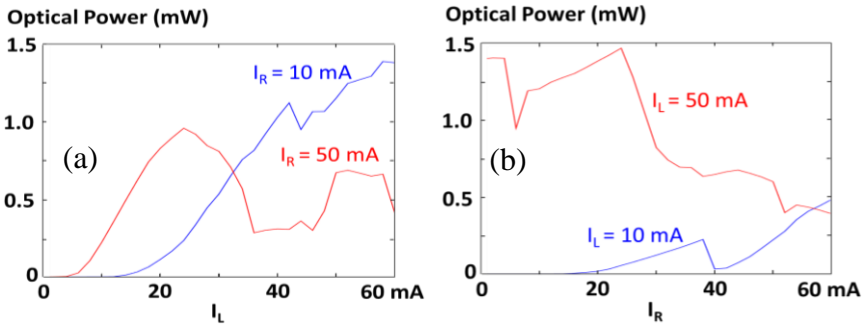

Figure 3.6: Optical output power in the waveguide (left grating coupler) versus the current into (**a**) the left section I_L and (**b**) the right section I_R for Laser B. The current into the other section was fixed at 10 or 50 mA.
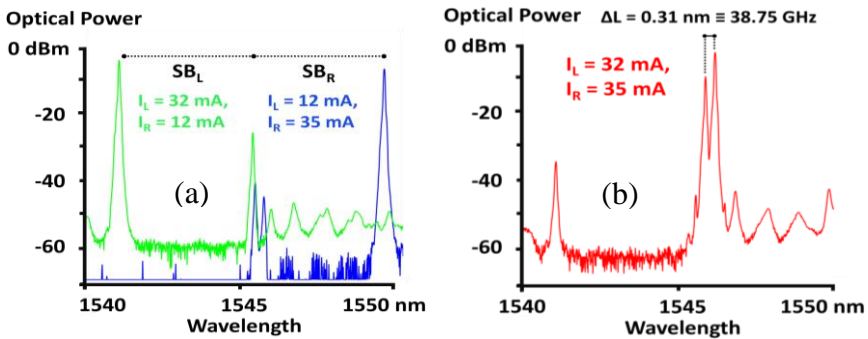

Figure 3.7: Optical spectra (power in the waveguide) showing (**a**) the 5 nm stop-bands (SB_L and SB_R) in laser B, for the left and right section, respectively, are almost overlapping, when the other section is biased close to threshold, and (**b**) two peaks spaced by 0.31 nm are produced, which corresponds to 38.75 GHz.

If biased by the current combination that allows the overlapping of the two stop-bands, two laser lines spaced by 0.31 nm appear in Fig. 3.7 (b). This corresponds to a beat frequency of 38.75 GHz (to be shown in the next section). Since the stop-band overlap of the lasers is visible, the mechanism of operation of this laser is suspected to be self-Q-switching. However, it is noticed that both lasers are lasing,

whereas self-Q-switching (shown in Fig. 3.2) has only one laser section lasing, and the other one is biased close to transparency and acts as a reflector. Due to the complex structure, determining the mechanism of operation is not trivial.

As discussed earlier, stop-band manipulation is not the only mechanism to generate self-pulsation signals. Self-pulsation can also occur in the presence of any two peaks spaced by a certain wavelength, without having the stop-bands of the two sections to overlap. This was referred to previously as beating-type self-pulsations. The optical spectra in Fig. 3.8 (a, c) are for Laser A, for two different current combinations (I_L = 45 mA, I_R = 19 mA) and (I_L = 43 mA, I_R = 23 mA). In those situations, two laser lines are generated, spaced by 0.096 and 0.204 nm, which corresponds to the generation of self-pulsation signals at 12 and 25.5 GHz, as shown in Fig. 3.8 (b, d).
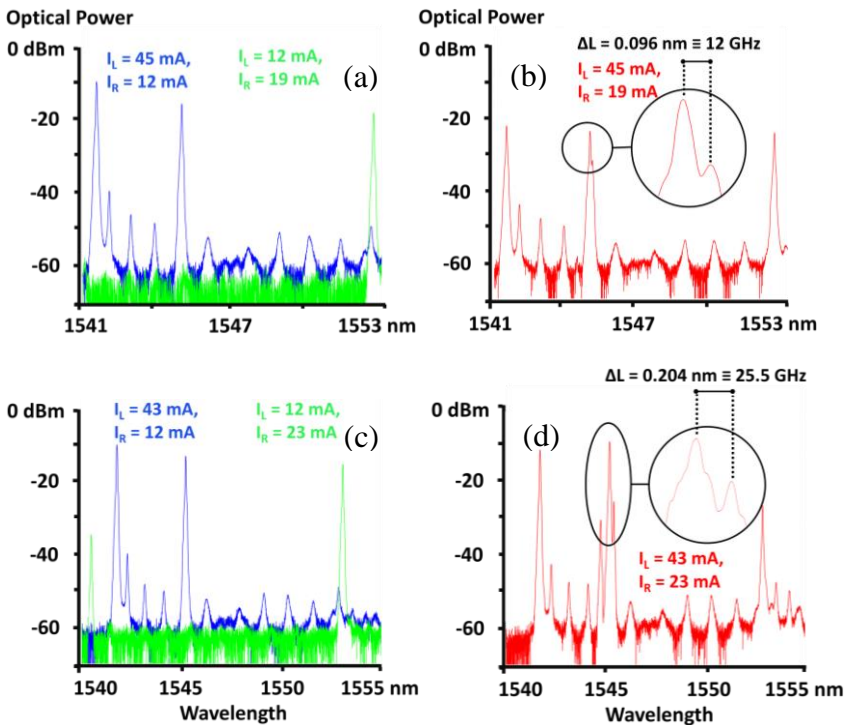

Figure 3.8: Optical spectra showing (**a, c**) beating-type self-pulsations in Laser A with a multi-mode behavior leading to (**b, d**) the generation of two laser lines spaced by 0.096 and 0.204 nm, which corresponds to self-pulsation signals with repetition rates of 12.5 and 25.5 GHz. The optical power shown is the power in the waveguide.

Since (1) the stop-bands of the two laser sections are not visible, (2) the laser exhibits a multi-mode behavior, and (3) the pulsation frequencies are high (> few GHz), the mechanism of operation is beating, according to Table 3.1. Using an optical filter, the unwanted modes can be easily filtered out.

3.2.4 Unlocked self-pulsation characteristics

In this section, the self-pulsation characteristics of the lasers are described. The measurement setup used in this experiment is depicted in Fig. 3.9. Both laser sections are DC biased, with the possibility of superimposing an RF signal to one of them. The output is fed to a Keopsys CEFA-C-HG C-band erbium-doped fiber-amplifier (EDFA) which raises the average optical power to 0 dBm. Later, the optical signal is converted to an electrical signal using a Discovery photodetector. The electrical signal is finally fed to an Agilent N9010A EXA electrical spectrum analyzer (ESA).
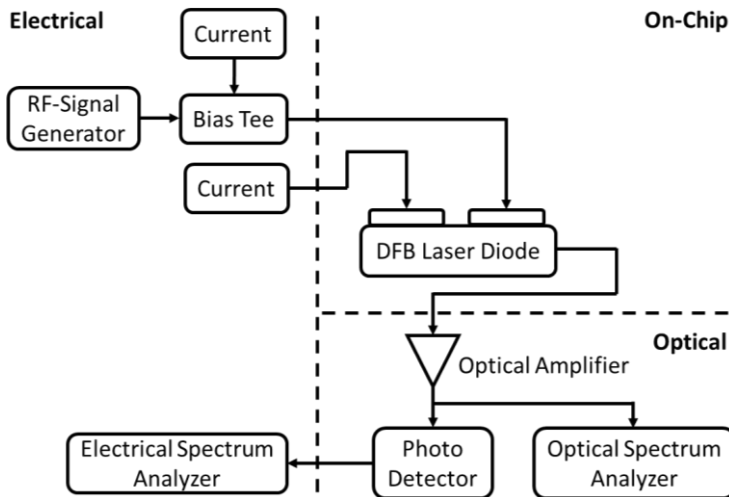

Figure 3.9: Block diagram of the setup used in the self-pulsation characterization.

First, we investigate the characteristics of the unlocked self-pulsation, i.e. without an applied (superimposed) RF signal. We start by showing the possibility of obtaining self-pulsation operation at different frequencies. In the next section, the locking of the self-pulsation signal is attempted, by introducing a locking RF signal.

As shown in Fig. 3.10, Laser A exhibits self-pulsation behavior with frequencies of 12.5, 25 and 40 GHz, with a spectral width of 40 MHz (measured by the ESA), and a signal-to-noise ratio of 15 dB. It is possible to continuously tune the repetition frequency by tuning the injected current in each section, or by tuning the temperature of the stage. The low electrical power level in Fig. 3.10 can be explained by the fact that it is equal to the optical power squared (e.g. −40 dBm electrical power translates to −15 dBm optical power, assuming photodetector responsivity of 0.7 A/W). Moreover, the 8 dB grating coupler losses are included in the power measurement.

We investigate these dependencies for both lasers. Fig. 3.11 (a) shows the measured repetition frequency when varying the current in the right section while keeping the current in the left section at 43 mA in Laser A. The spectra recorded by the ESA are shown in Fig. 3.11 (a'), in which the self-pulsation peaks move to higher frequencies with higher injected current I_R. The repetition frequency can be tuned over a range of 25 GHz by tuning the current. The opposite trend is shown in Fig. 3.11 (b) when increasing the current in the left section. Fig. 3.11 (b') shows the spectra for this case. By increasing the current, the separation between the two laser lines (in Fig. 3.8 (b, d)) is reduced (increased) in Fig. 3.11 (b) (Fig. 3.11 (a)), which reduces (increases) the beating frequency.
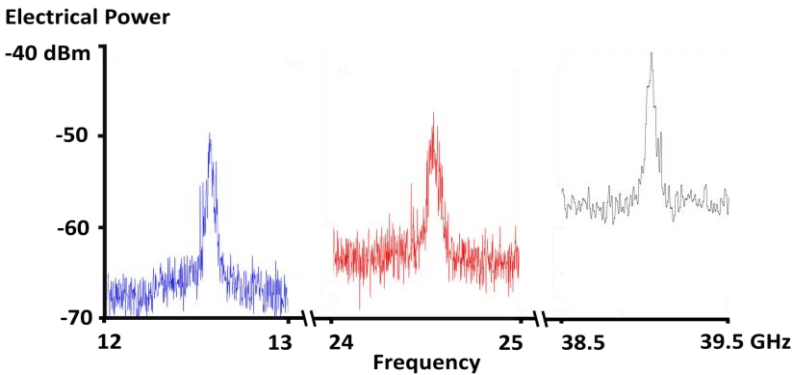

Figure 3.10: RF spectra of the self-pulsations in Laser A at around 12.5, 24.5 and 39 GHz.

Fig. 3.12 (a, b) shows the current scan for Laser B, in which the repetition frequency decreases first and increases again as the scan current increases. This is shown in the spectra in Fig. 3.12 (a', b'). In this case, tuning the repetition frequency by changing the current is done over a range of 6 GHz. The tuning behavior can be explained by beating as follows. At first, the spacing between the two laser peaks is reduced, until the peaks are almost overlapping, and then the spacing is increased again. The peaks never overlap completely, and thus a frequency of zero is never obtained. This can be explained by thinking about the two laser sections as two coupled oscillators which cannot have the exact same frequency, as explained in detail in [29].

This measurement was done while keeping the substrate temperature at 15 °C. The variation of the repetition frequency with current can also be due to a shift of the Bragg wavelengths in both sections due to Joule heating. This leads to the next factor that controls the repetition frequency: the temperature. The temperature of the sample holder (which is assumed to be close to the substrate temperature) was used to tune the repetition frequency over a 7 GHz range. The dependence of the repetition frequency on the sample holder temperature is shown in Fig. 3.13 (a), in which a repetition frequency tuning from 35 – 42 GHz can be observed for Laser B. The spectra are also shown in Fig. 3.13 (b). It is noticeable that the amplitude of the peaks decreases with increasing temperature. This is expected since heating normally reduces the output power of the laser.
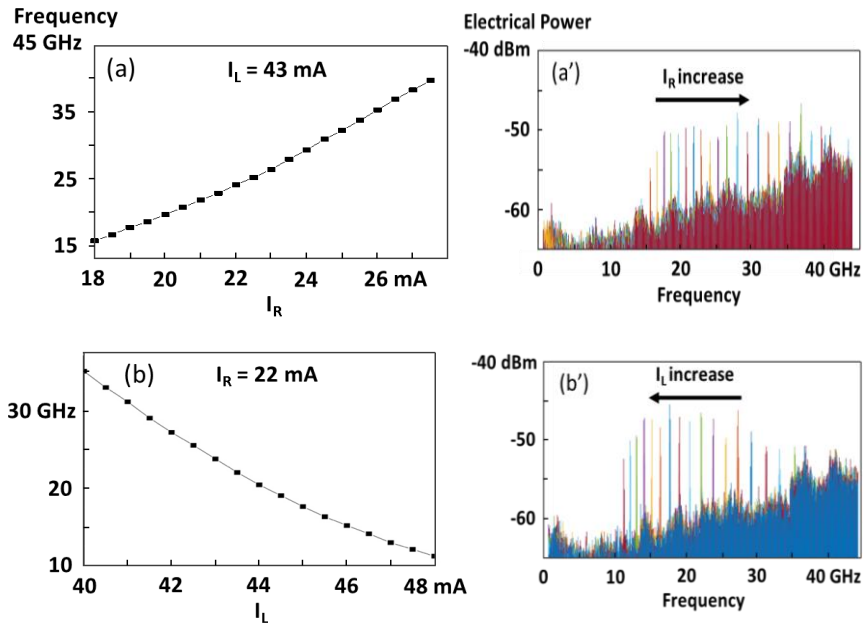
Figure 3.11: Variation of the repetition frequency over 25 GHz by tuning the current in the right (**a**, **a'**) or left (**b**, **b'**) laser section for Laser A.
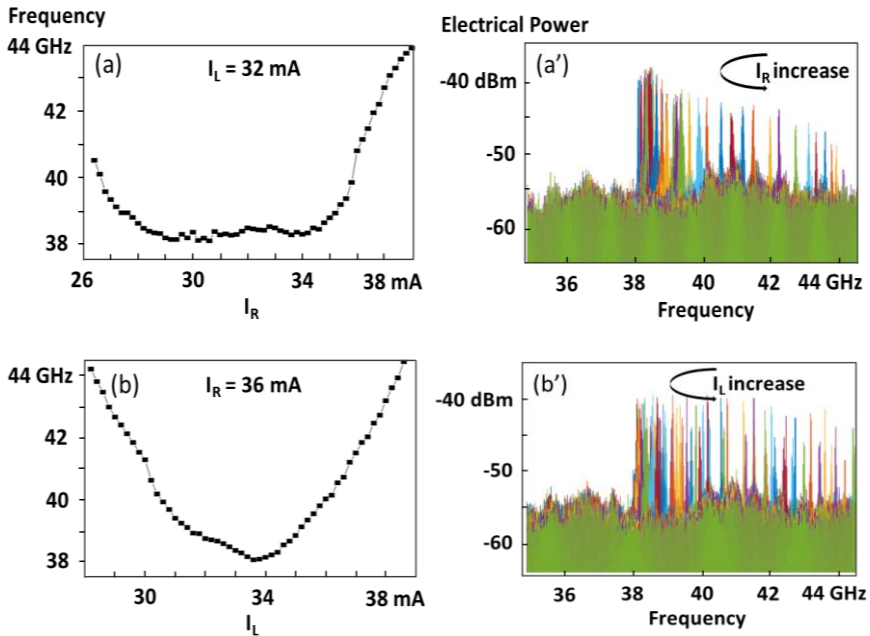

Figure 3.12: Variation of the repetition frequency over 6 GHz by tuning the current in the right (**a**, **a'**) or left (**b**, **b'**) laser section for laser B.
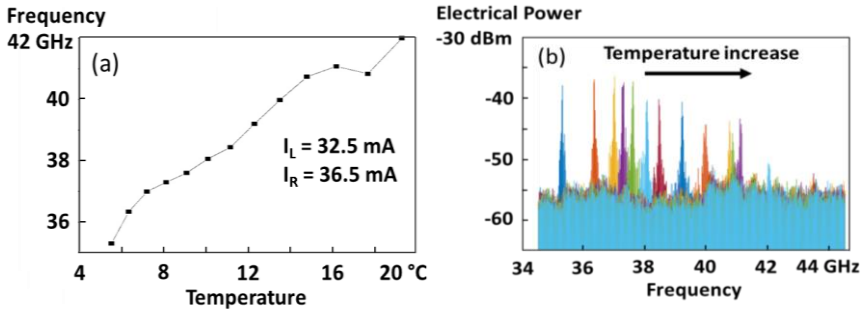
Figure 3.13: (**a**) Tuning the substrate temperature changes the repetition frequency over a 7 GHz range (Laser B), (**b**) the shift in the self-pulsation peak from 35 − 42 GHz.

3.2.5 Locking the self-pulsation to an RF signal

In this section, an RF signal is used to lock the self-pulsation signal. The RF signal is applied to the right section of Laser A in this measurement, but similar results can be achieved when the RF signal is applied to the left section. The electrical spectrum in Fig. 3.14 (a) shows the RF locking signal and the self-pulsation peak. The spectral linewidth of the self-pulsation peak is 40 MHz (Fig. 3.14 (b)). Initially (i.e. without locking), the self-pulsation peak is not stable and can fluctuate over a few 100 MHz due to fluctuations in current and/or temperature.

The RF signal power decreases further away from the repetition frequency. This is because away from the repetition frequency, the modulation response has a weaker or no resonance. An RF signal with an electrical power of −7 dBm and a phase noise of −83 dBc is generated using a Rohde & Schwarz SMR40 RF signal generator and applied to the laser using a Cascade GS probe with a 100 μm pitch. After locking, it is observed that the spectral linewidth of the laser was reduced significantly from 40 MHz to less than 10 Hz (Fig. 3.14 (c, d)). It is expected that the locked self-pulsation signal has the same linewidth as the generated RF signal, as shown in [31].

For the signal to be locked, it should be within a range of around 300 MHz around the natural repetition frequency. Increasing the RF power widens the locking range. The minimum RF power that must be applied to the laser to generate a stable locked signal with a spectral linewidth below 10 Hz is −17 dBm, substantially lower than the 2 dBm reported in [13].

We summarize hereby the benefits of locking the self-pulsation signal to an RF signal. Firstly, locking stabilizes the self-pulsation signal. Without an RF locking signal, the repetition frequency continuously fluctuates within a range of around 300 MHz. Secondly, locking reduces the spectral linewidth significantly. In our case, the spectral linewidth before locking was 40 MHz. After locking, the spectral linewidth is drastically reduced to less than 10 Hz. Finally, locking can be done using an RF input electrical signal as weak as −17 dBm, with the opportunity to transmit this signal over an optical link.
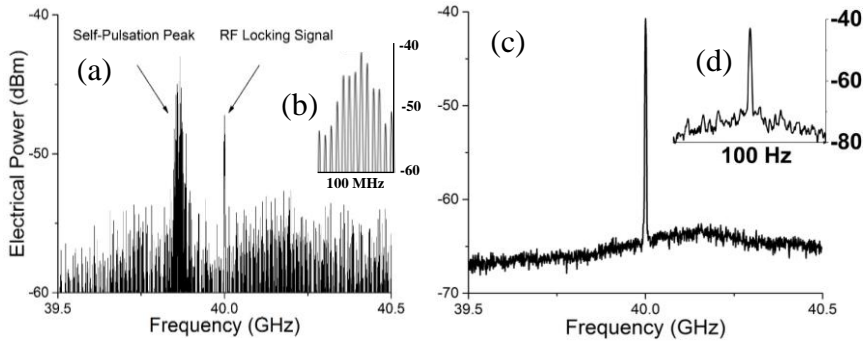
Figure 3.14: The self-pulsation signal with a spectral width of 40 MHz is shown in (**a, b**) along with a locking RF signal of −7 dBm at 40 GHz. A locked self-pulsation signal is shown in (**c**) with a spectral width of below 10 Hz in (**d**).

As mentioned, the RF input electrical signal in Fig. 3.14 has a power of −7 dBm. However, the ESA shows a signal with a power of −47 dBm. This discrepancy is due to a few factors. First, the impedance mismatch between the probe (50 Ω) and the device (≈ 10 Ω), which means a 66% reflection. Second, the losses throughout the electrical/optical link, such as the grating coupler losses, losses in the RF cables and RF probe.

The main advantage that our device has over mode-locked lasers is the tunability. Moreover, as mentioned earlier, obtaining low frequencies is challenging with mode-locked lasers, since long cavities are needed. Although not reported here, obtaining low self-pulsation frequencies of less than 3 GHz is also possible using some of our devices.

Similarly to this work, tunability was also demonstrated in other monolithic InP self-pulsating laser diodes [13]. The tunability range was between 20 and 60 GHz. In our case, since a high-speed photodiodes with a bandwidth higher than 40 GHz is expensive and not available, we could not demonstrate self-pulsation frequencies higher than 40 GHz.

3.3 Bandwidth-enhanced DFB laser diodes

In the previous section, the beating between two laser lines was employed to generate self-pulsations using two-section laser diodes. It was previously reported that two-section laser diodes can also be used to enhance the bandwidth of standard single-section DFB laser diodes [32–34]. Tuning the bias condition, one can shift the operation from the self-pulsation regime to the bandwidth enhancement regime, and vice versa.

In this section, we demonstrate an improvement to our standard single-section DFB laser diode using this approach. We discuss the theory of operation and review the relevant literature. Finally, we present the laser characteristics.

3.3.1 Literature review and state-of-the-art

Classical single section InP-on-Si DFB laser diodes are limited by their relaxation oscillation frequency. Fortunately, there are some advanced laser designs that improve the modulation bandwidth substantially. The exploitation of a photon-photon resonance (PPR) is one of the techniques used to enhance the modulation bandwidth [32–33, 35]. In this technique, the existence of a second longitudinal mode (Fig. 3.15 (a)) close to the main laser mode (Fig. 3.15 (b)) enhances the bandwidth to beyond the beat frequency [36]. For example, the exploitation of a PPR using an external cavity made by the grating couplers helped to improve the 3 dB modulation bandwidth from 8 to 34 GHz in [35]. The transmission of 56 Gbps NRZ was verified.
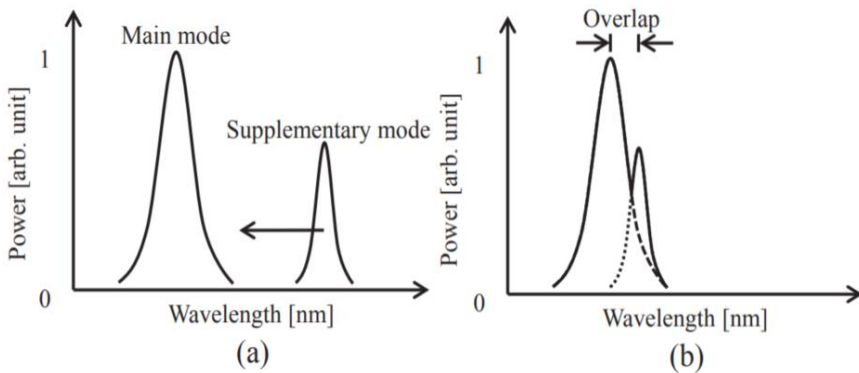

Figure 3.15: Photon-photon resonance is exploited by bringing the second longitudinal mode in (**a**) close to the main mode, to enhance the bandwidth beyond the beat frequency in (**b**) [36].

In [32], a monolithic InP distributed reflector (DR) laser was fabricated to exploit the same effect. The structure consisted of a DFB section and a DBR section. A 3 dB modulation bandwidth of 55 GHz and transmission of 112 Gbps PAM-4 were shown. A similar modulation enhancement of 57.4 GHz was predicted for a two-section DFB laser diode in [34].

To understand the bandwidth enhancement mechanism, and the distinction from the self-pulsation mechanisms, we discuss the finite-difference traveling-wave (FDTW) simulations in Fig. 3.16 [33]. In these simulations, two DBR lasers, and a phase tuning section are considered. Fig. 3.16 (a–c) show the round-trip gain (on the left axis in blue) and round-trip phase (on the right axis in red) around the Bragg frequency for phase shift $\Phi_s = 0, \pi, \pi/2$, respectively. Moreover, Fig. 3.16 (a–c) show the main cavity mode (the red circle), the relevant side mode (the green circle), and other modes (the blue dots). The three scenarios show how tuning the phase section and changing the frequency (wavelength) and thus the roundtrip gain of the main and side mode changes the small signal modulation response (S_{21}), as shown in Fig. 3.17 (a–c).
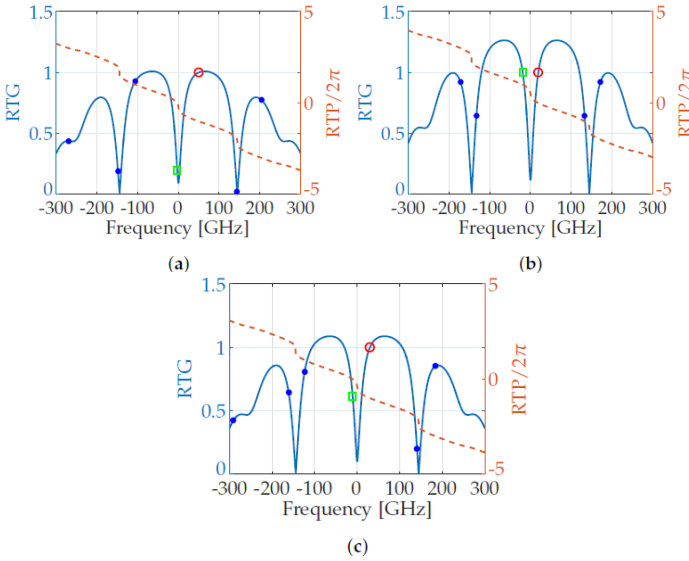
Figure 3.16: Round-trip gain (left axis in blue) and round-trip phase (right axis in red) around the Bragg frequency (wavelength), for different phase shifts (**a**) $\Phi_s = 0$, (**b**) $\Phi_s = \pi$, and (**c**) $\Phi_s = \pi/2$. The main cavity mode (the green circle), side mode (the red circle), and other modes (blue dots) are indicated [33].

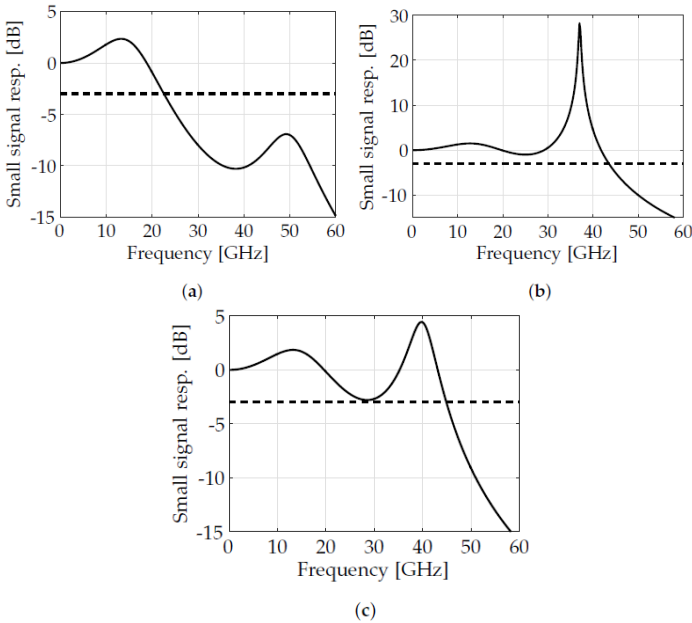**Figure 3.17:** Small-signal modulation response (S_{21}) for different phase shifts (**a**) $\Phi_s = 0$, (**b**) $\Phi_s = \pi$, and (**c**) $\Phi_s = \pi/2$ showing the different responses corresponding to the different scenarios in Fig. 3.16 [33].

In the first scenario shown in Fig. 3.16 (a), the side mode has a very low gain. This is the case in which there is no bandwidth enhancement, which corresponds to the small-signal modulation response shown in Fig. 3.17 (a). In the second scenario shown in Fig. 3.16 (b), the side mode has as much gain as the main mode. This produces a self-pulsation signal, which is the result of the distorted S_{21} response in Fig. 3.17 (b). In the third and last scenario shown in Fig. 3.16 (c), the side mode has a lower gain than the main mode. This results in an enhancement in the modulation bandwidth at the frequency equal to the frequency separation between the main mode and the side mode (38 GHz), as shown in the S_{21} response in Fig. 3.17 (c).

In summary, the regime of operation can shift between the normal laser modulation regime, the bandwidth enhancement regime, and the self-pulsation regime, depending on the location of the main and side modes, and their round-trip gain. The existence of a phase tuning section makes it easier to operate the device in different regimes.

3.3.2 Design

A two-section DFB laser diode, with the same configuration as Laser A in the previous section was used in this experiment. The only difference was that the period of the grating was 241 nm, which slightly redshifts the lasing wavelength compared to the lasers shown in the previous section.

As shown in Fig. 3.16 (c), depending on the location of the main and side modes, the modulation bandwidth can be enhanced. A phase tuning section can be useful to change the phase of the light in the cavity and thus change the operation of the device. For simplicity, we propose a design using a two-section DFB laser, and we scan the injected current through all possible current combinations. The results shown below are the best obtained results, among many other lasers. In our experiment, the right section is modulated while the left laser output is considered. This gave a higher modulation bandwidth than modulating the left section. We hypothesize that this is because the left section can act as a reflector (more feedback), and as an amplifier (more power), which enhances the performance further.

3.3.3 Static laser characteristics

The optical output power in the waveguide versus bias current behavior for the device is similar to the one reported in section 3.2. Fig. 3.18 (a) shows the optical spectrum (before filtering) when the bias currents are $I_L = 48$ mA and $I_R = 60$ mA, which produces the highest 3 dB modulation bandwidth found while performing a sweep. In Fig. 3.18 (b), the two beating modes with significantly different power levels (after filtering) with a separation of 20 GHz (≈ 0.15 nm) are observed. This is different than Laser B shown in Fig. 3.7 (b), which cannot be used for bandwidth enhancement, since the laser lines are of comparable power, which would result in strong response around the beating frequency and self-pulsation, as shown in the previous section and also as shown in Fig. 3.16–17 (b).

As the bonding layer thickness is very small (less than 10 nm), the silicon grating coupling is strong. The stop-band of each laser section is not clearly identified in Fig. 3.18 (a), but from section 3.2, we have seen that the stopbands are around 5 nm, with the extracted coupling coefficient κ being ≈ 150 cm^{-1}. This high coupling coefficient, and the high currents in comparison to the ones used in section 3.2 for self-pulsation, could be the source of the multi-mode behavior observed in the spectrum. Therefore, a possible solution to eliminate such modes is to lower the coupling coefficient (i.e. by increasing the bonding thickness) which in turn reduces the stop-band of each section and excites fewer modes.
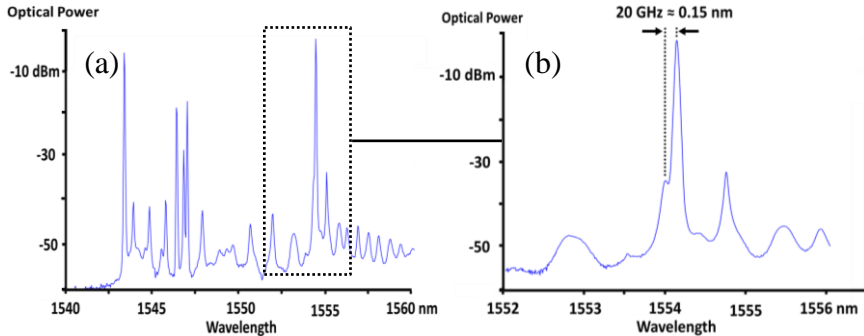

Figure 3.18: Optical spectrum (power in the waveguide) of the laser at I_L = 48 mA, I_R = 60 mA (**a**) before filtering and (**b**) after filtering at the receiver side. The spacing between the main mode and the side mode is about 0.15 nm, which corresponds to 20 GHz.

Moreover, a quarter-wave (λ/4) phase shift is placed in the middle of the cavity to ensure single-mode operation for DFB laser diodes [37–39]. Our device has indeed a λ/4 phase shift in the middle. However, since the middle of the cavity lies between the two laser sections, and since each section can be considered as an independent laser source, placing multiple phase shifts as proposed in [40–41] along the laser cavity could be a more suitable solution to guarantee single-mode operation.

3.3.4 Dynamic laser characteristics

A small-signal modulation experiment is done by constructing the setup depicted in Fig. 3.19. An Agilent N5247A vector network analyzer (VNA) was used to provide electrical signals up to 67 GHz. The signal is superimposed on a positive bias, using a 45 GHz bias Tee, and the signal is applied to the right laser section using a Cascade GS probe with a 100 μm pitch. A Keopsys CEFA-C-HG C-band EDFA was used to boost the optical output signal and compensate for any losses in the optical link. For example, the loss from the grating coupler is about 8 dB around 1550 nm. The amplifier is followed by a Santec optical tunable filter (OTF-350) with a bandwidth of 1 nm to suppress the amplified spontaneous emission from the EDFA.
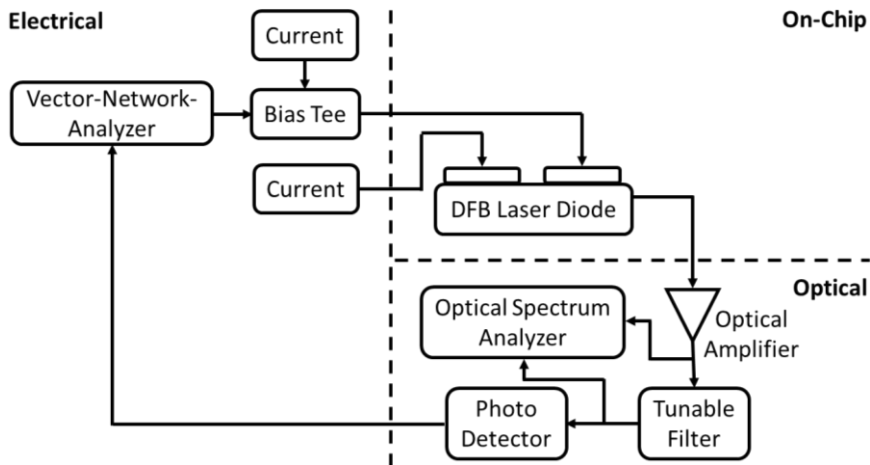
Figure 3.19: Block diagram of the small-signal modulation experiment setup

For our experiment, the laser line at 1555 nm (Fig. 3.18 (a)) is filtered out with a tunable filter that has a bandwidth of 5 nm (Fig. 3.18 (b)). Moreover, the filter also serves to eliminate the other modes, which improves the quality of the eye diagram at the receiver side. An alternative could be to integrate an on-chip optical filter. Making this device single-mode (as discussed, by reducing the coupling coefficient or using multiple phase shifts) and having high output power (e.g. less grating coupler losses) removes the necessity for the amplifier and the filter.

A 3 dB modulation bandwidth of 10 GHz can be observed in Fig. 3.20 (a) at $I_L = 46$ mA, and $I_R = 50$ mA. This relaxation oscillation frequency is comparable to the one in the previously demonstrated devices [28, 35]. By tuning I_R to 60 mA, a second resonance appears around 20 GHz. This improves the total 3 dB modulation bandwidth to 23 GHz, more than a factor of 2. The resonance peak at 20 GHz results from the beating between the two laser lines, with the side mode sufficiently weaker than the main mode, as shown in Fig. 3.18 (b). These lines are separated by around 20 GHz (≈ 0.15 nm). There is an agreement between the beating modes and the S_{21} response in our case (Fig. 3.18 (b), Fig. 3.20 (b)) and in [33] (Fig. 3.16–17 (c)).
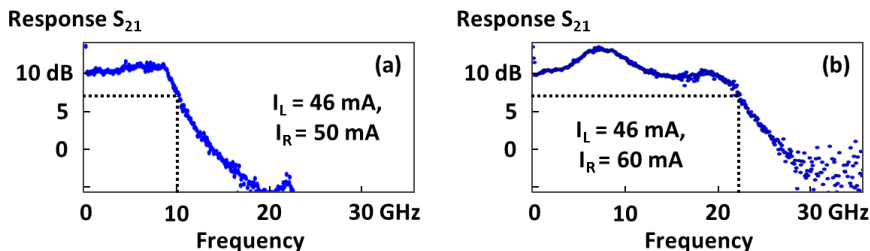

Figure 3.20: S_{21} response showing a 3 dB modulation bandwidth of (**a**) 10 GHz and (**b**) 23 GHz for the indicated bias current combinations.

As shown in section 3.2, it is possible to tune the separation between the laser lines, which controls the frequency at which the second resonance occurs, and fine-tunes the S_{21} response. However, for the second resonance to enhance the bandwidth, the gap between it and the relaxation oscillation frequency should be minimal, such that the drop in the response in between would still be within 3 dB. Therefore, the enhancement is still partially limited by the relaxation oscillation frequency.

As mentioned in [33], there are different regimes in which the laser can operate. If the laser is operating in the self-pulsation regime, it won't be possible to use it for bandwidth enhancement, and vice versa. This is confirmed in our experiment, as there was no self-pulsation behavior found while the laser was operating in the bandwidth enhancement regime shown in Fig. 3.20 (b). Here, we want to show that by tuning the injected current values around the neighborhood of the bandwidth-enhancement regime, it is possible to shift the operation regime to the self-pulsation regime. To do that, the injected current combination I_R and I_L to obtain 3.19 (b) was changed from (46 mA, 60 mA) to (34 mA, 48 mA) to obtain the self-pulsation behavior in Fig. 3.21. The repetition rate in Fig. 3.21 is around 20 GHz, identical to the 20 GHz bandwidth enhancement peak in Fig. 3.20 (b).
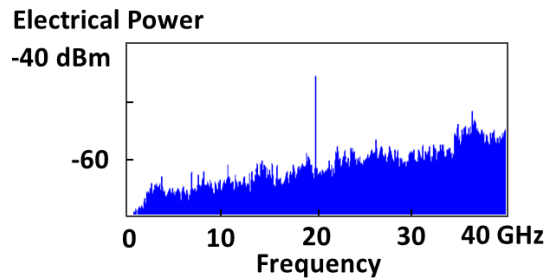

Figure 3.21: Electrical output power in the self-pulsation regime at I_L = 34 mA and I_R = 48 mA showing a self-pulsation signal at 20 GHz

Data transmission experiments were conducted to investigate the large-signal modulation of the laser, after constructing the setup depicted in Fig. 3.22. This was done using a Keysight M8195A arbitrary waveform generator (AWG), a Discovery photodetector, and a Keysight DSAZ634A real-time oscilloscope. Transmission of 45 Gbps (NRZ-OOK) using a pseudorandom binary sequence (PRBS) data with a pattern length of 2^7-1 shows an open eye diagram, in Fig. 3.23. The voltage swing applied to the right section of the laser is about 2.2 V_{pp}. The bias conditions were: I_L = 46 mA and I_R = 50 mA, resulting in −5 dBm output power in single mode fiber.

We observe a discrepancy between the I_R used to obtain the best S_{21} response (23 GHz at I_R = 60 mA), and the one used to obtain the highest bitrate in the large-signal modulation experiment (45 Gbps at I_R = 50 mA). The S_{21} response for both cases was shown in Fig. 3.20 (a, b). This can be justified by the fact that the two experiments were done over different time periods, under different

conditions and with different setups. For example, temperature variations due to the use of different temperature controllers could influence the results.
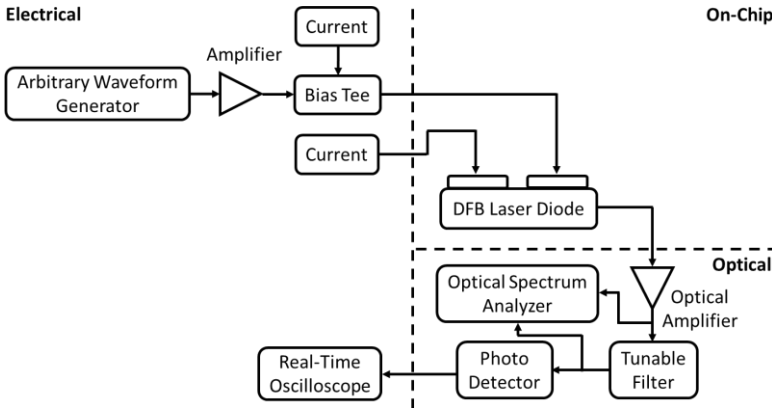

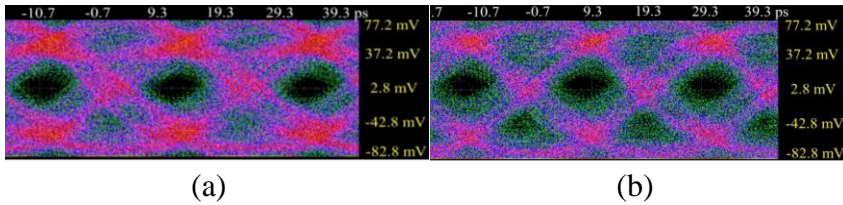**Figure 3.22:** Block diagram of the large-signal modulation setup

Figure 3.23: Eye diagrams for 45 Gbps NRZ sub-HD-FEC transmission (**a**) back-to-back and (**b**) with 2 km NZ-DSF, for a pattern length of 2^7-1.

A root-raised-cosine filter with a roll-off factor $\alpha = 0.5$ is used to shape the eye diagrams. Fig. 3.23 shows the eye diagram for a back-to-back configuration, followed by the eye diagram after transmission over a 2 km long non-zero dispersion-shifted fiber (NZ-DSF). The used Corning fiber had a dispersion D of 5 ps/nm·km.

If we assume no chirp, a maximum bitrate B_{max} of 70 Gbps can be achieved, as given by (3.3) [42] solely based on the fiber dispersion characteristics. Normally, direct modulation induces chirp to the signal, which would reduce the achieved bit rate in comparison to the theoretical one. In (3.3), L is the length (2 km) and β_2 is called the group velocity dispersion parameter (-6.4 ps^2/km), which tells how much an optical pulse broadens due to the propagation inside an optical fiber, as given by (3.4).

$$B_{max} \leq \frac{1}{4\sqrt{|\beta_2|L}} \tag{3.3}$$

$$D = -\frac{2\pi c}{\lambda^2}\beta_2 \tag{3.4}$$

The bit error rate (BER) versus received power measurement for this laser is shown in Fig. 3.24. 45 Gbps transmission for word lengths of 2^7-1 and 2^{15} with a BER lower than the 7% hard-decision forward error correction (HD-FEC) limit of $3.8 \cdot 10^{-3}$ is possible for a received signal power above -7 dBm.

To further improve the modulation bandwidth, one main improvement would be to increase the relaxation oscillation frequency. This can be done by increasing the differential gain, reducing the threshold current, or reducing the laser cavity volume, as will be discussed in the next section.
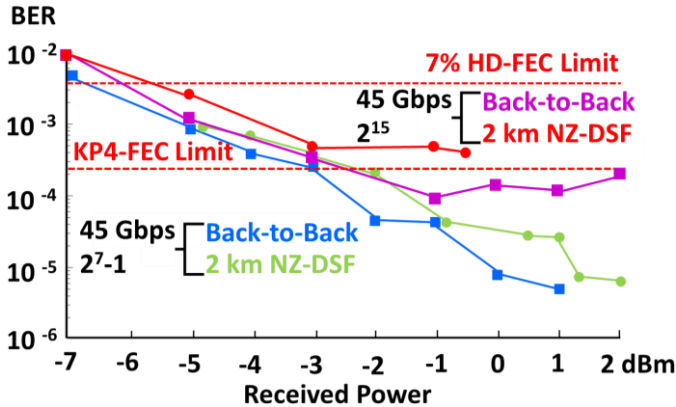

Figure 3.24: bit error rate (BER) versus received power showing sub-HD-FEC operation for a received power as low as -5 dBm.

3.4 Low-threshold DFB laser diodes

To ensure stable performance for the devices in data centers, the temperature needs to be stabilized. Therefore, cooling needs to be applied at all times. The operating costs are very significant, and reports show that more than half of the data centres' cooling systems are inefficient [43]. To improve this, the power efficiency of the single components needs to be improved. The less heat generated by these devices, the less energy needs to be spent on cooling. If achieved, this can massively reduce operational costs.

This section focuses on the design and the fabrication of low-threshold DFB laser diodes. First, we review the state of the art, and the different device configurations used to achieve this goal. Next, we discuss the design and fabrication of the proposed laser structure. Then, we report on the static characteristics and compare the threshold current values to the case of a standard single-section DFB laser. We also compare the current values needed to reach certain output power in both cases. Finally, we show the dynamic characteristics, starting from small-signal modulation and ending with large-signal modulation experiments.

3.4.1 Literature review and state-of-the-art

There were many attempts in the literature to improve the efficiency of laser diodes. The approach used in several works used a reflector on one side of the cavity. For simplicity, let us consider a Fabry-Perot cavity with length L, confinement factor Γ, threshold gain g_{th}, facet reflectivities R_1 and R_2, and a_0 is the cavity losses. The lasing condition is given by:

$$R_1 R_2 \, e^{(\Gamma g_{th} - a_0)2L} = 1 \tag{3.5}$$

(3.5) shows that if R_1 or R_2 increased, the threshold gain would decrease. The threshold gain is the gain for which all losses are compensated. In this case, the number of photons lost in one roundtrip is equal to the number of photons generated. At that point, the lasing action starts. There are two sources of loss: mirror loss, and internal loss.

Reflecting light back into the cavity reduces the lost photons, which reduces the threshold gain. In a laser diode, this means less current needs to be injected to achieve lasing. Moreover, increasing the reflectivity on one side can also decrease the required cavity length L. Decreasing the cavity length is not only interesting because of the smaller footprint, but also to increase the modulation bandwidth. The modulation bandwidth in a laser diode is given by:

$$(2\pi f_r)^2 = \frac{dG}{dN} \; \frac{(I - I_{th})}{qdwL} \tag{3.6}$$

where f_r is the relaxation oscillation frequency, dG/dN is the differential gain, I and I_{th} are the injected and threshold current, respectively, q is the elementary charge, d, w, and L are the thickness, width, and length of the active region. The gain G is given by (3.7), where Γ is the optical confinement factor, g is the material gain, and v_g is the group velocity.

$$G = \Gamma \, g \, v_g \tag{3.7}$$

Reducing the length is not always desired. First, because for a very short cavity, the reflection or the gain should be very high to satisfy (3.5). Second, reducing the cavity length in a laser diode increases the electrical resistance and the thermal resistance. The electrical resistance depends mainly on the dimensions of the device and the doping. For example, the electrical resistance increases when the length or width of the cavity decrease, when the thickness increases, or when the doping decreases. The thermal resistance R_{th} also depends on the device dimensions, and is given by:

$$R_{th} = \frac{\Delta T}{P_{diss}} = \frac{\Delta T}{VI} = \frac{\Delta T}{VJwL} \tag{3.8}$$

where ΔT is the change in temperature in the active region with respect to the stage temperature, with and without forward bias, and P_{diss} is the dissipated electrical power. We know that $P_{diss} = IV$, where I is the injected electrical current (given by $I = JwL$), and V is the voltage. In the context of a two-section laser, the thermal resistance does not increase very much if only one section was biased, as the second section would act as a heat sink.

To sum up, the aim is to create a reflection section, such that the gain and threshold current are decreased, and less electrical power is needed to have a certain optical power. This allows a device with a shorter length, which increases the bandwidth, however, this increases the electrical and thermal resistance. Keeping low electrical and thermal resistance is essential to maintain high optical output power.

There were a few attempts to achieve such an operation using different approaches. A monolithic InP-based distributed reflector (DR) laser, which consists of an active DFB laser, and a passive DBR, was used in [44]. This allowed a threshold current of 15.4 mA, and a single mode operation around 1.55 μm. Another approach was discussed in [45–46], in which a monolithic InP-based two-section DFB laser was used. In this case, one section was used as a reflector. It was shown that in comparison to a standard DFB with anti-reflective (AR) coated facets at both ends (AR-AR), a distributed reflector on one side could reduce the threshold current, and produce equally high optical output power levels at lower injected current values. The reported threshold current was 10 mA, compared to 15 mA for the AR-AR laser, or 15.4 mA in [44], which is around 34% improvement. Reducing the threshold current can help in reducing the power consumption of the lasers, by being able to obtain a certain output power but at lower injected current, as will be discussed throughout the section.

Reducing the threshold current can also be achieved by making a very short laser. Recently, a threshold current of 0.39 mA was demonstrated in [47], using a 20 μm long DR (DFB/DBR) laser. A bit rate of 25 Gbps was verified. However, due to the small footprint, the resistance is as high as 900 Ω. Also, this laser had a maximum output power in the fiber of 77 μW, roughly two orders of magnitude less than in [45].

Regarding III-V-on-silicon lasers, one of the first demonstrations was reported in [48]. This was a standard single-section DFB laser with a threshold current of 25 mA, 3 dB modulation bandwidth of 2.5 GHz, and a maximum output power of 3.5 mW at bias current of 100 mA. An improvement has been reported in [28], in which a threshold current of 17 mA, 3 dB modulation bandwidth of 15 GHz, and a maximum output power of 6.5 mW at bias current of 100 mA has been demonstrated. Similar work using a distributed Bragg reflector laser was reported in [49], with a threshold current of 20 mA, 3 dB modulation bandwidth of 7 GHz, and a maximum output power of 15 mW at bias current of 160 mA. The reported results are for cooled operation at room temperature.

In this section, we report on the performance of an integrated III-V-on-Si DFB laser with a distributed reflector at one end, like the one in [45–46]. We aim to

reduce the threshold current values, and consequently obtain similar output power, 3 dB modulation bandwidth, and data transmission with smaller injected current values. This is all attempted in the context of heterogeneously integrated III-V-on-silicon two-section DFB laser diodes.

3.4.2 Design

The top and 3D view of the proposed two-section laser structure are shown in Fig. 3.25 (a, b). The laser is 500 μm long (excluding the tapers) and is cut in two sections with unequal length. The lengths of the left and the right section are 340 μm and 140 μm. To maximize the achieved relaxation oscillation frequency f_r, it is desired to design a narrow and short laser, as shown in (3.6).

Therefore, the short (right) laser section of 140 μm is chosen to be pumped and modulated, in comparison to the 340 μm long laser in [28]. Moreover, the laser is 1.5 μm wide, as opposed to the 3.4 μm wide laser in [28]. However, due to the V-shaped mesa structure (discussed in chapter 2), the width at the bottom of the p-InP is around 500 nm compared to 1.5 μm at the top of the p-InGaAs. Therefore, the fabrication of narrower structures can be challenging.
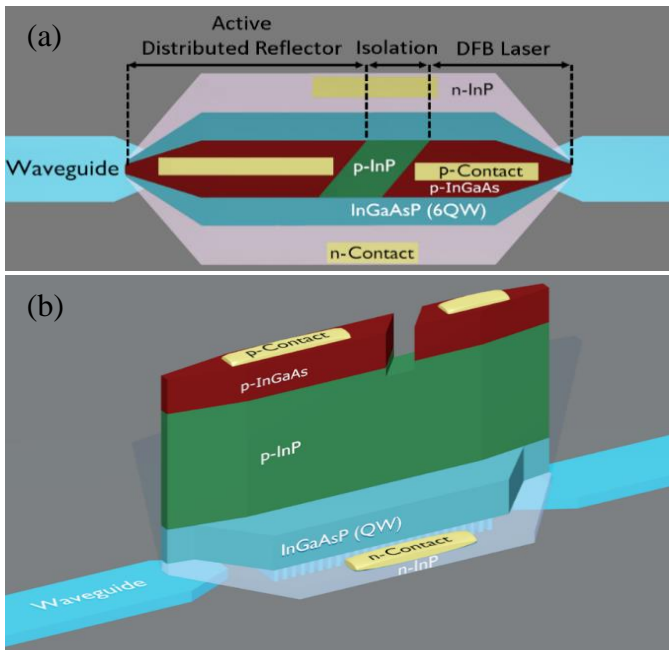

Figure 3.25: (a) Top and **(b)** 3D view of the proposed device. The right section is pumped and acts as a laser diode, while the left one is not pumped and acts as a distributed reflector.

The tapers are electrically connected to the laser sections, each of them being 230 μm long. This suggests that the threshold current associated with the active

section is less than the threshold current measured for both the active section and the taper. To measure the exact threshold current of the active section, the tapers should be electrically isolated, and only the active section should be pumped. Finally, the silicon DFB grating has a period of 246 nm, with a duty cycle of 50%.

3.4.3 Static laser characteristics

Grating couplers are used to couple the light out of the chip, with a coupling loss of 6 dB. Fig. 3.26 shows a comparison between the output optical power in the waveguide as a function of injected current. This is done for a few cases: (1) Injected current I_R in the right section (while $I_L=0$), and (4) Injected current while short circuiting both sections and pumping them with a single current I_{Single} (i.e. identical to a standard single-section DFB laser). In between these two cases, the effect of slightly tuning I_L was also investigated. The results show a shift in I_{th} for (2, 3) $I_L = 2, 4$ mA, which indicates that the lowest value of I_{th} was achieved at $I_L = 0$ mA. However, at higher current, we can see that the output power is slightly higher, as the left section now has less absorption. In the measurements reported below, the light is extracted from the side of the biased laser section, since the other section is a reflector/absorber.

The measured series resistance is around 10 Ω for each of the laser sections. The threshold currents for each case are shown in Fig. 3.26: (1) $I_{th (I_L = 0)} = 9$ mA and (2) $I_{th, Single} = 17$ mA. As shown, $I_{th, (I_L = 0)}$ is less than $I_{th, Single}$ by 47%. $I_{th (I_L = 0)}$ is also 47% less than the 17 mA reported in [28].
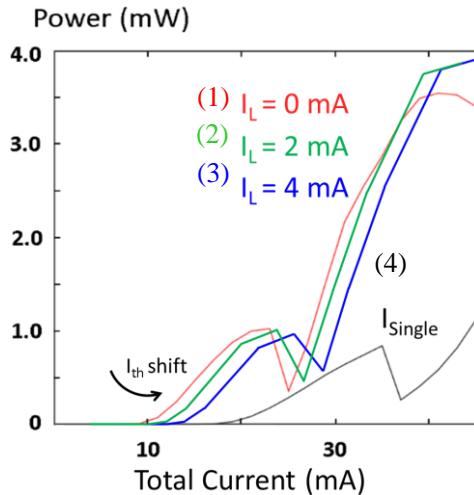
Figure 3.26: Optical output power P_{opt} in the waveguide versus the total current injected $I_R + I_L$ for (1, 2, 3) $I_L = 0, 2, 4$ mA, and (4) the total uniform current injected in the complete laser length by short circuiting both sections I_{Single}.

The optical output power in the waveguide (averaged between 30 and 50 mA) for the first case is higher than the value reported in [28], and 3 times higher than

for the second case, as shown in Fig. 3.26. Fig. 3.27 (a, b) show the single mode behavior of the laser with I_R = 15 and 45 mA, with wavelengths of 1544.5 nm and 1540.5 nm. Normally, a higher injected current would redshift the wavelength of operation. However, the wavelength of operation blueshifts instead. This indicates that mode hopping occurred, which explains the kink in the optical power around I_R = 20 mA in Fig. 3.26.
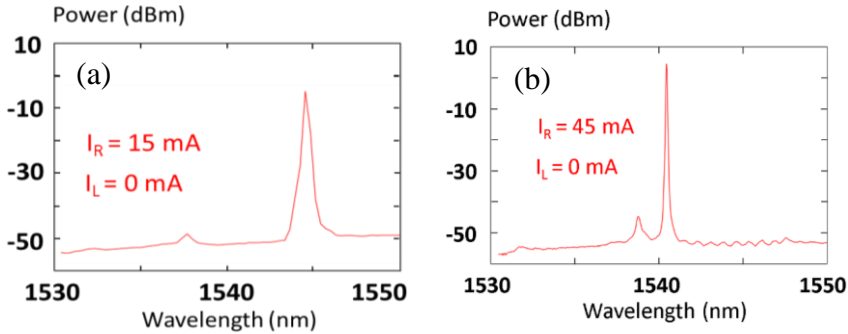
Figure 3.27: The spectrum of the laser showing mode hopping from (**a**) 1544.5 nm (at I_R = 15 mA) to (**b**) 1540.5 nm (at I_R = 45 mA), instead of a redshift.

In addition to the increased power efficiency, the threshold current of these lasers is a key factor in reducing power consumption. This configuration has resulted in devices with a very low threshold current of 7 and 6 mA, as shown in Fig. 3.28 (a, b), for laser sections that are (140 μm, 140 μm) and (100 μm, 100 μm) long. From the three previously reported lasers, it can be concluded that smaller laser sections have lower threshold current. Moreover, it can be observed that with a smaller section, the maximum output power is less, and the output optical power drop is faster (i.e. at a lower current). This is because shorter sections have higher series and thermal resistance. Finally, the width of the laser was decreased (1.5 μm as opposed to 3.4 μm in [28]), which also increases the series and thermal resistance.
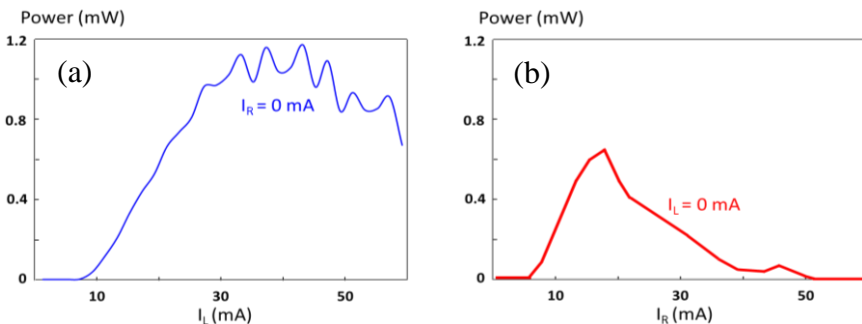
Figure 3.28: Optical output power P_{opt} in the waveguide as a function of the current in one of the sections. The length of each section is (**a**) 140 μm and (**b**) 100 μm.

We wanted to see if we can further push down the threshold current in the laser shown in Fig. 3.28 (b). Since the taper is also pumped, it is predicted that the actual threshold current for only the right active section is around half of the measured threshold current value. To investigate that, the taper is electrically isolated from the laser section by etching the gold using FIB. After etching, the resistance increased from 10 to 13 Ω. Knowing that the threshold current before etching was 6 mA, we can expect the threshold current after etching to decrease to 4.2 mA. This is in agreement with the measurement results shown in Fig. 3.29 (a, b), in which a threshold current of around 4.5 mA is shown. It is also noticed that the output optical power reduces, since the 230 μm long taper is acting as an absorber (as it could not be pumped in this specific chip).
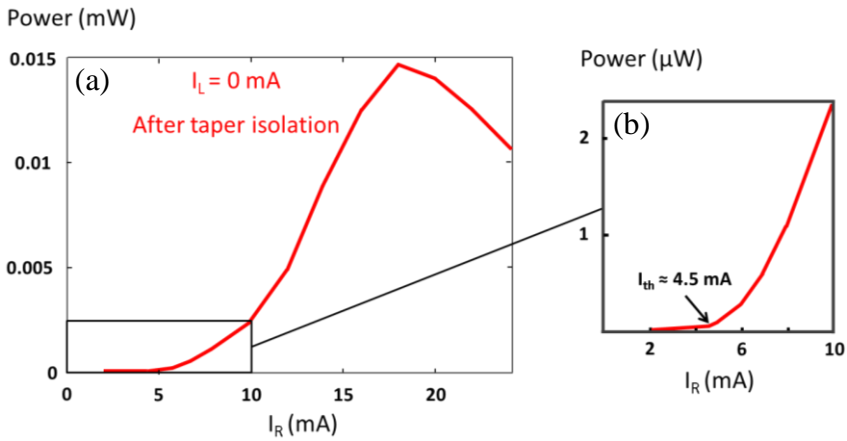

Figure 3.29: (**a**) After taper isolation, the threshold current has dropped, along with the optical power. A closer look in (**b**) shows that the threshold current was reduced to 4.5 mA.

3.4.4 Dynamic laser characteristics

We investigate the laser shown in Fig. 3.26 further, due to its superior performance compared to the ones in Fig. 3.28 (a, b). The S_{21} response was obtained using an Agilent N5247A VNA, after constructing the setup shown in Fig. 3.30. The right section is modulated at two different bias currents, while the current in the left section $I_L = 0$ mA. The measured 3 dB modulation bandwidth is nearly 15 GHz, as shown in Fig. 3.31. This is obtained at $I_R = 45$ mA, a 55% lower bias current than used in [28] to obtain about the same bandwidth.

The drop in the S_{21} at low frequencies was also observed in previous devices and is attributed to the extra modulation of the taper at low frequencies. This is because the taper acts as an amplifier, and is limited by the carrier life time [2]. It was also shown that the impact on data transmission can be minimized by electrically isolating the tapers.

The setup in Fig. 3.32 is constructed for the large-signal modulation experiment. This was done using a Keysight M8195A AWG. After amplifying

the signal using a 50 GHz RF electrical amplifier (SHF-S807), the RF electrical signal generated by the AWG is applied to the right laser section using a Cascade Ground-Signal (GS) probe with a 100 μm pitch. To boost the output optical signal, an EDFA is used. The amplified spontaneous emission is filtered out using an optical tunable filter (Santec OTF-350). Finally, a photodetector converts the signal back to an electrical signal, which is fed to a Keysight DSAZ634A real-time oscilloscope.

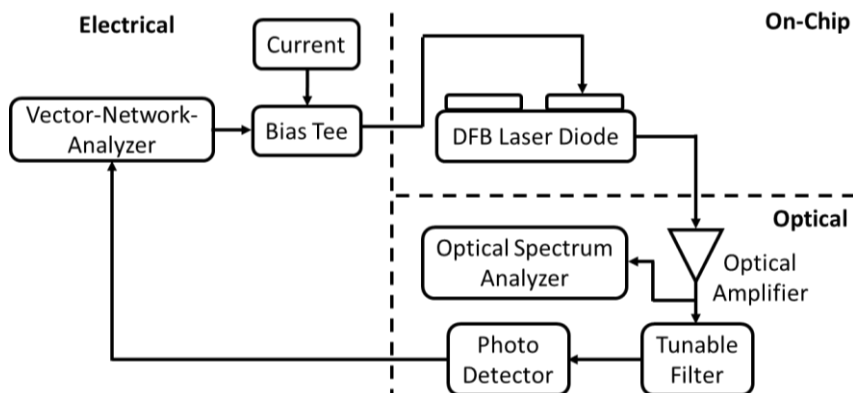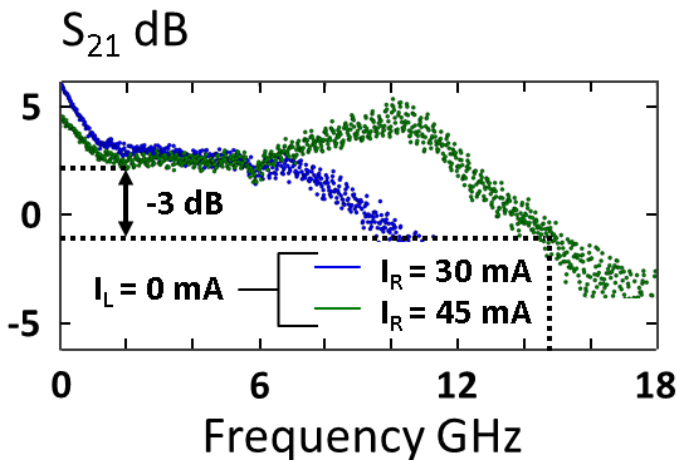**Figure 3.30:** Block diagram of the small-signal modulation experiment setup

Figure 3.31: The S_{21} response for two injected currents into the right section I_R while I_L = 0 mA. The 3 dB modulation bandwidth is 15 GHz for I_R = 45 mA.
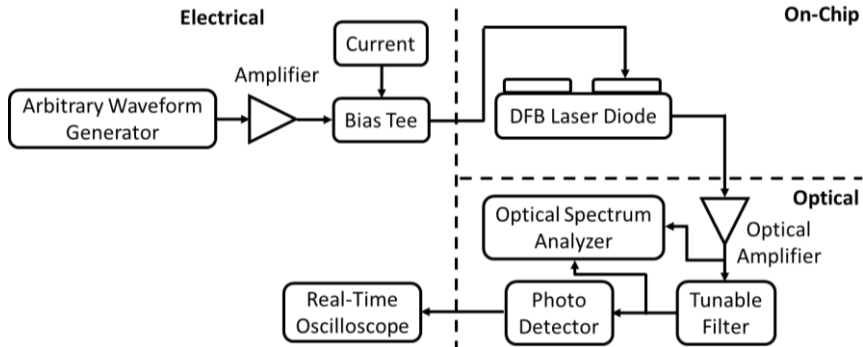
Figure 3.32: Block diagram of the large-signal modulation setup

Transmission of a 28 Gbps NRZ-OOK signal using a PRBS with a word length of 2^7-1 was verified. The output of the RF amplifier is a voltage swing with 1.13 V_{pp}, and is then applied to the device, at a bias current I_R = 45 mA. Fig. 3.33 (a, b) shows the eye diagrams for back-to-back configuration and after transmission over a 2 km long NZ-DSF Corning fiber. The recorded BER with the 2 km long NZ-DSF is less than $1.0 \cdot 10^{-6}$. With longer word lengths, the device performance degrades, and the eye diagram closes. This is because longer word lengths contain more low frequency components. This is in agreement with the S_{21} response in Fig. 3.31, which shows a low frequency roll-off. This roll-off makes the device performance poor for longer word lengths.

The results suggest a drastic improvement in bandwidth compared to the one obtained in [28], achieving the same bandwidth with 59% less power consumption, and obtaining a 47% lower threshold current.
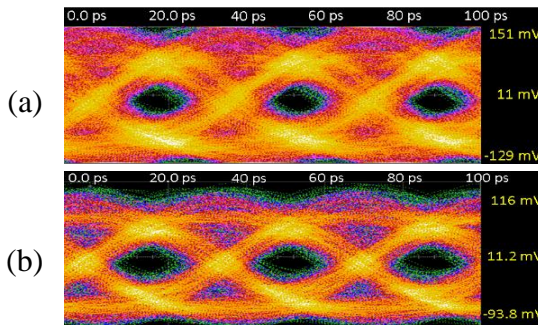

Figure 3.33: (**a**, **b**) Eye diagrams for transmission at 28 Gbps in the back-to-back configuration and with a 2 km NZ-DSF link for a pattern length of 2^7-1

3.5 Conclusion

We have demonstrated III-V-on-silicon two-section DFB laser diodes, for three different functions. Hereunder, we conclude for each one.

Self-pulsating DFB laser diodes:

The first function was self-pulsation. All of the previous demonstrations were on monolithic III-V DFB lasers. The demonstrations showed pulsating frequencies as high as 40 GHz [9]. This is the first time a non-mode-locked self-pulsating laser is demonstrated on the III-V-on-silicon platform. We have shown that by varying the currents and the temperature, the repetition frequency can be tuned over a wide range between 12–40 GHz. The tuning of the repetition frequency gives this laser an advantage over mode-locked lasers. The self-pulsations can be locked to an RF signal with a minimum power of −17 dBm, substantially lower than the −2 dBm given in [13]. This results in a narrow RF spectral linewidth of less than 10 Hz, which is expected to be the same as that of the RF signal generator [31]. This is useful, for instance, in the generation of an optical microwave carrier, which is desired for radio-over-fiber applications.

Bandwidth-enhanced DFB laser diodes:

The second function was using the two-section laser structure for the enhancement of the modulation bandwidth, compared to that of a standard single-section laser. This was done by introducing a second resonance peak in the S_{21} response. This allowed to push the maximum achievable modulation bandwidth up to 25 GHz. Data transmission at 45 Gbps was shown.

The performance was enhanced compared to that of a similar standard single-section laser in [28]. However, the performance fails to surpass the modulation bandwidth of (1) 34 GHz in [35] caused by PPR due to an external cavity, and (2) 55 GHz in [32], caused by PPR due to the interaction between DFB-DBR modes. This is summarized in Table 3.2.

Table 3.2: Comparison between the device performance in [32, 35, 50] and in this work

	[35]	**[32]**	**[50]**	**This work**
Platform	III-V/Si	III-V	III-V/SiC	III-V/Si
Number of sections	1	2	2	2
Laser type	DFB	DFB/DBR	DFB/DBR	DFB/DFB
Small-signal modulation bandwidth (GHz)	34	55	>100	25

In comparison to [35], the power levels drop in between the resonance and the enhancement frequencies for bandwidths more than 25 GHz, which prevents the device from outperforming the one in [35].

Another reason the device could not outperform the ones in [32, 35] is because of the relaxation oscillation frequency. The relaxation oscillation frequency is 25 GHz in [32], while 8 GHz in this work. As previously mentioned, the relaxation oscillation frequency is defined by the parameters given in (3.6), which depends on many factors. For a second resonance peak to enhance the bandwidth, the gap between the two frequency peaks (the relaxation and the enhancement peaks) should be minimal, for the response not to drop significantly between them. Further study is required to improve the relaxation frequency.

There are a few ways to increase the relaxation oscillation frequency, as suggested by (3.6). For example, using a material with a higher differential gain, or by increasing the number of quantum wells. Reducing the threshold current, or the volume, are alternative ways to increase the relaxation oscillation frequency, as attempted in section 3.4.

It is worth mentioning a recent work that reported a high bandwidth of >100 GHz using a distributed reflector (DFB/DBR) [50]. In this work, a Silicon Carbide (SiC) substrate is used, which has a thermal conductivity of 490 W/m/K, in comparison to 68 and 149 W/m/K for InP and silicon, respectively. This significantly improves the performances by eliminating any thermal issues. Additionally, a high confinement factor was achieved, by forming a thin III-V layer on a low refractive index material.

Low-threshold DFB laser diodes:

Thirdly, and finally, two-section lasers were used to reduce the power consumption compared to the equivalent standard single-section lasers. Table 3.3 summarizes the research findings, and compares them to similar monolithic InP devices in the literature. Table 3.4 has the same comparison, but to III-V-on-silicon devices.

In our devices, we concluded that the threshold current can be reduced when reducing the laser section length. Threshold currents of 9, 7, and 6 mA were demonstrated for lasers with length 250, 150 and 100 μm, respectively. It was also observed that the power levels dropped for shorter device lengths, which indicated that the heating of the device becomes more dominant. By isolating the tapers from the laser section, the threshold current was reduced from 6 to 4.5 mA. Since the taper is not pumped, it starts to absorb the light, instead of acting as a semiconductor optical amplifier. This results in a further reduction in optical output power.

In comparison to monolithic InP devices, the threshold current value reported in this work is slightly better than the one reported in [45] (9 versus 10 mA). Both of them have around 30% smaller threshold current than the one reported in [44]. However, the power consumption remains lower in [45]. This can be justified by examining Fig. 3.26, in which the optical output power goes down drastically after I = 40 mA. As previously discussed, heating is one of the problems that our III-V-on-silicon lasers suffer from. This is mainly due to the 2 μm thick buried oxide, the 100 nm bonding layer consisting of both BCB and oxide, and finally, it could be partially attributed to the planarizing side BCB, as shown in Fig. 3.34.

Table 3.3: Comparison between this work and the monolithic InP devices in the literature

	[44]	[45]	[47]	This work
Platform	III-V	III-V	III-V/Si	III-V/Si
Laser type	DFB/DBR	DFB/DFB	DFB/DBR	DFB/DFB
Number of sections	2	2	2	2
I_{th} (mA)	15.4	10	0.39	9
Maximum output power (mW) @ bias current (mA)	4 @ 45	17 @ 50	0.08 @ 1.8	3.5 @ 45
Small-signal modulation bandwidth (GHz)	-	23	-	15
I (mA) for Maximum $BW_{3\,dB}$	-	20	-	45
Power consumption (mW) for maximum $BW_{3\,dB}$	-	28	-	83
Efficiency % for maximum output power	-	34%	2.7%	4.3%

Table 3.4: Comparison between this work and the III-V/silicon devices in the literature

	[48]	[49]	[28]	This work
Platform	III-V/Si	III-V/Si	III-V/Si	III-V/Si
Laser type	DFB	DBR	DFB	DFB/DFB
Number of sections	1	1	1	2
I_{th} (mA)	25	20	17	9
Maximum output power (mW) @ bias current (mA)	3.5 @ 100	15 @ 160	6.5 @ 100	3.5 @ 45
Small-signal modulation bandwidth (GHz)	2.5	7	15	15
I (mA) for maximum $BW_{3\,dB}$	105	131	100	45
Power consumption (mW) for maximum $BW_{3\,dB}$	210	235	200	83
Efficiency % for maximum output power	1.6%	2.4%	3.4%	4.3%

The thermal conductivities of BCB and silicon oxide are 0.29 and 1.38 W/m·K at room temperature, respectively. On the other hand, the thermal conductivities of the silicon and InP substrates are 149 and 68 W/m·K at room temperature, respectively. The poor thermal conductivity of BCB and oxide prevents good heat sinking into the silicon substrate. InP-based lasers, such as the one in [45] can easily sink the heat through the InP substrate. Moreover, since the device dimensions were shrunk compared to [28], the heating effect was more pronounced at high currents.

If the heating effect is not dominant, shrinking the device further can reduce the power consumption and threshold current. This is shown in [47], in which a record low threshold current of 0.39 mA was reported using a DR (DFB/DBR) InP laser fabricated on a silicon substrate. This was due to a few reasons. First, this device had a much larger coupling coefficient $\kappa \approx 1000 \text{ cm}^{-1}$ compared to $\kappa \approx 150 \text{ cm}^{-1}$ in our devices. This resulted in the optical output power to be limited to 77 µW. Second, the heat can sink into the InP but also to the underlying silicon substrate.

In comparison to III-V-on-silicon devices, the results suggests a drastic improvement in the performance of the laser diode compared to the very similar device in [28], which already outperforms [48–49]. Achieving the same bandwidth with 59% less power consumption was demonstrated, with a 47% lower threshold current.
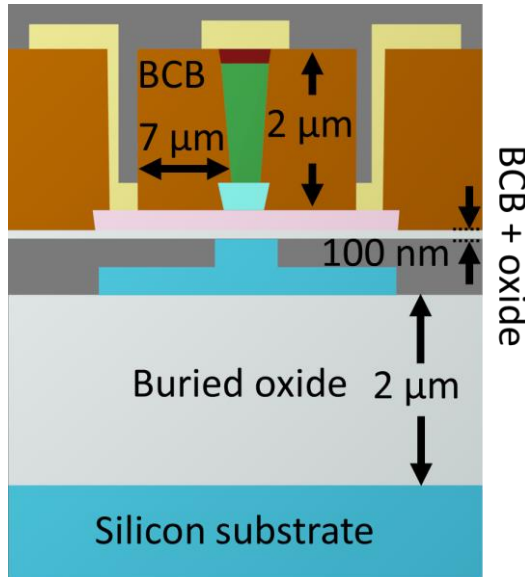

Figure 3.34: Cross section of the laser structure showing possible heat sink challenges

References

[1] G. Roelkens, A. Abbasi, P. Cardile, U.D. Dave, A. De Groote, Y. De Koninck, S. Dhoore, X. Fu, A. Gassenq, N. Hattasan, Q. Huang, S. Kumari, S. Keyvaninia, B. Kuyken, L. Li, P. Mechet, M. Muneeb, D. Sanchez, H. Shao, T. Spuesens, A. Subramanian, S. Uvin, M. Tassaert, K. Van Gasse, J. Verbist, R. Wang, Z. Wang, J. Zhang, J. Van Campenhout, Y. Xin, J. Bauwelinck, G. Morthier, R. Baets, D. Van Thourhout, "III-V-on-silicon photonic devices for optical communication and sensing," Photonics (invited), 2(3), pp. 969–1004, (2015).

[2] A. Abbasi, "High speed directly modulated III-V-on-Silicon DFB lasers," Doctoral Thesis, Ghent University, (2016).

[3] S. Dhoore, "Heterogeneously Integrated III-V-on-Silicon Wavelength-Tunable DFB and DBR Lasers," Doctoral Thesis, Ghent University, (2018).

[4] X. Qi and J. Liu, "Photonic Microwave Applications of the Dynamics of Semiconductor Lasers," IEEE Journal of Selected Topics in Quantum Electronics, 17(2), pp. 1198–1211, (2011).

[5] J. Capmany, I. Gasulla, and D. Perez, "Microwave photonics: The programmable processor," Nature Photonics, 10(1), pp. 6–8, (2016).

[6] P. Barsnley, H.-J. Wickes, G. E. Wickens, and D. M. Spirit, "All-Optical Clock Recovery from 5 Gb/s RZ Data Using a Self-Pulsating 1.56 μm Laser Diode," IEEE Photonics Technology Letters, 3(10), pp. 942–945, (1991).

[7] B. Sartorius, C. Bornholdt, O. Brox, H. J. Ehrke, D. Hoffmann, R. Ludwig, and M. Möhrle, "All optical clock recovery module based on a self-pulsating DFB-laser," Electronic Letters, 34(17), pp. 1664–1665, (1998).

[8] B. Sartorius, C. Bornholdt, O. Brox, H. J. Ehrke, D. Hoffmann, R. Ludwig, and M. Möhrle, "Bit-Rate Flexible All-Optical Clock Recovery," Optical Fiber Communication (OFC), , pp. 24–26 (FB1-1), (1999).

[9] C. Bornholdt, B. Sartorius, S. Schelbase, M. Mohrle, and S. Bauer, "Self-pulsating DFB laser for all-optical clock recovery at 40Gbit/s," Electronic Letters, 36(4), pp. 327–328 (2000).

[10] H.-J. Wünsche, U. Bandelow, H. Wenzel, and D. Marcenac, "Self pulsations by mode degeneracy in two-section DFB lasers," SPIE Proceedings Series, vol. 2399, pp. 195–206, (1995).

[11] S. Latkowski, V. Moskalenko, S. Tahvili, L. Augustin, M. Smit, K. Williams, and E. Bente, "Monolithically integrated 2.5 GHz extended cavity mode-locked ring laser with intracavity phase modulators," Optics Letters, 40(1), pp. 77–80, (2015).

[12] Z. Wang, K. Van Gasse,V. Moskalenko, S. Latkowski, E. Bente, B. Kuyken, and G. Roelkens, "A III-V-on-Si ultra-dense comb laser," Light Science and Applications, 6(5), (2017).

[13] W. Wei, P. Lin, S. Ke, and X. Zeng, "Realizing 60 GHz narrow-linewidth photonic microwaves with very low RF driving power," Laser Physics Letters, 13(12), p. 126202, (2016).

[14] R. Schatz, "Longitudinal Spatial Instability in Symmetric Semiconductor Lasers due to Spatial Hole Burning," IEEE Journal of Quantum Electronics, 28(6), pp. 1443–1449, (1992).

[15] M. Mohrle, U. Feiste, J. Horer, R. Molt, and B. Sartorius, "Gigahertz self-pulsation in 1.5 μm wavelength multisection DFB lasers," IEEE Photonics Technology Letters, 4(9), pp. 976–979, (1992).

[16] B. Sartorius, M. Mohrle, S. Malchow, S. Reichenbacher et al., "Wavelength and polarisation independent all optical synchronisation of high frequency DFB type self-pulsations," Electronic Letters, 32(11), pp. 1026–1028, (1996).

[17] B. Sartorius, M. Mohrle, S. Reichenbacher, H. Preier, H.-J. Wunsche, and U. Bandelow, "Dispersive self Q-switching in self-pulsating DFB lasers," IEEE Journal of Quantum Electronics, 33(2), pp. 211–218, (1997).

[18] H. Wenzel, U. Bandelow, H.-J. Wunsche, and J. Rehberg, "Mechanisms of fast self pulsations in two-section DFB lasers," IEEE Journal of Quantum Electronics, 32(1), pp. 69–78, (1996).

[19] D. D. Marcenac, and J. E. Carroll, "Distinction between multimoded and singlemoded self-pulsations in DFB lasers," Electronics Letters, 30(14), pp. 1137–1138, (1994).

[20] P. Phelan, D. McDonald, A. Egan, J. Hegarty, R. O'Dowd, G. Farrell, and S. Lindgren, "Comparison of self-pulsation in multisection lasers with distributed feedback and intracavity saturable absorbers," Proceedings of the IEEE, (141), pp. 114–118, (1994).

[21] A.-J. Lowery and P. C. R. Gurney, "Improving pulses from 2-contact self-pulsating DFB semiconductor lasers," Semiconductor Laser Conference, paper P-11, pp. 103–104, (1994).

[22] A.J. Lowery, "Dynamics of SHB-induced mode instabilities in uniform DFB semiconductor lasers," Electronics Letters, 29(21), pp. 1852–1854, (1993).

[23] M. Mohrle, B. Sartorius, C. Bornholdt, S. Bauer, O. Brox, A. Sigmund, R. Steingruber, H. Radziunas, H.-J. Wunsche,, "Detuned Grating Multisection-RW-DFB Lasers for High-Speed Optical Signal Processing," IEEE Journal of Selected Topics in Quantum Electronics, 7(2), pp. 217–223, (2001).

[24] U. Bandelow, H.-J. Wunsche, B. Sartorius, and M. Mohrle, "Dispersive Self- Q-Switching in DFB Lasers—Theory Versus Experiment," IEEE Journal of Selected Topics in Quantum Electronics, 3(2), (1997).

[25] B. Sartorius, C. Bornholdt, O. Brox, H.-J. Ehrke, D. Hoffmann, R. Ludwig, and M. Mohrle, "All-optical clock recovery module based on self-pulsating DFB laser," Electronics Letters, 34(17), pp. 1664–1665, (1998).

[26] D. Chen, H. Zhu, S. Liang, H. Wang, Y. Zhang, "Self-pulsation in a two-section DFB laser with varied ridge width," Semiconductor Science and Technology, 23(1), pp. 015008, (2008).

[27] A. Abbasi, C. Spatharakis, G. Kanakis, N. Sequeira Andre, H. Louchet, A. Katumba, J. Verbist, H. Avramopoulos, P. Bienstman, X. Yin, J. Bauwelinck, G. Roelkens, G. Morthier, "High speed direct modulation of a heterogeneously integrated InP/SOI DFB laser," Journal of Lightwave Technology, 34(8), pp. 1683–1687, (2016).

[28] A. Abbasi, J. Verbist, J. Van kerrebrouck, F. Lelarge, G. H. Duan, x. Yin, J. Bauwelinck, G. Roelkens, G. Morthier, "28 Gb/s direct modulation heterogeneously integrated C-band InP/SOI DFB laser," Optics Express, 23(20), pp. 26479–26485, (2015).

[29] G. Dolfo et al., "Damping of coupled harmonic oscillators," European journal of physics 39, 025005, (2018).

[30] Rohde & Schwarz SMR40 datasheet

[31] G.-H. Duan, and G. Pham "Injection-locking properties of self pulsation in semiconductor lasers," IEE Proceedings – Optoelectronics, 144(4), pp. 228–234, (1997).

[32] Y. Matsui, R. Schatz, T. Pham, W. A. Ling, G. Carey, H. M. Daghighian, D. Adams, T. Sudo, and C. Roxlo, "55 GHz Bandwidth Distributed Reflector Laser," Journal of Lightwave Technology, 35(3), pp. 397–403, (2017).

[33] P. Bardella, W. W. Chow, and I. Montrosset, "Design and Analysis of Enhanced Modulation Response in Integrated Coupled Cavities DBR Lasers Using Photon-Photon Resonance," Photonics, 3(1), (2016).

[34] T. Numai, "High Resonance Frequency in a Coupled Cavity DFB-LD with Phase-Shifted/Uniform Gratings by Photon-Photon Resonance," proceedings in International Conference of Numerical Simulation of Optoelectronic Devices (NUSOD), pp. 35–36, (2017).

[35] A. Abbasi, B. Moeneclaey, J. Verbist, X. Yin, J. Bauwelinck, G.-H. Duan, G. Roelkens, G. Morthier, "Direct and electro-absorption modulation of a III-V-on-silicon DFB laser at 56 Gbps," IEEE Journal of Selected Topics in Quantum Electronics, 23(6), p. 1501307, (2017).

[36] T. Kitano, M. N. Uddin, B. Hong, A. Tajima, H. Jiang, K. Hamamoto, "Demonstration of photon–photon resonance peak enhancement by waveguide configuration modification on active multimode interferometer laser diode," Japanese Journal of Applied Physics, p. 55(8S3), (2016).

[37] K. Utaka, S. Akiba, K. Sakai, Y. Matsushima, "Analysis of quarter-wave-shifted DFB laser," Electronics Letters, 20(8), pp. 326–327, (1984).

[38] J.E.A. Whiteaway, G.H.B. Thompson, A.J. Collar, C.J. Armistead, "The design assessment of lambda /4 phase-shifted DFB laser structures," IEEE Journal of Quantum Electronics, 25(6), pp. 1261–1279, (1989).

[39] M. Okai, S. Tsuji, N. Chinone, "Stability of the longitudinal mode in lambda /4-shifted InGaAsP/InP DFB lasers," IEEE Journal of Quantum Electronics, 25(6), pp. 1314–1319, (1989).

[40] G. P. Agrawal, J. E. Geusic, and P. J. Anthony, "Distributed feedback lasers with multiple phase-shift regions," Applied Physics Letters, 53(3), pp. 178–179 (1988).

[41] Y. Shi, X. Chen, Y. Zhou, S. Li, L. Li, and Y. Feng, "Experimental demonstration of the three phase shifted DFB semiconductor laser based on Reconstruction-Equivalent-Chirp technique," Optics Express, 20(16), pp. 17374–17379, (2012).

[42] G. Agrawal, "Fiber-optic communication systems" Third edition, Wiley-Interscience, (2002).

[43] J. Ni, X. Bai, "A review of air conditioning energy performance in data centers," Renewable and Sustainable Energy Reviews, 67, pp. 625–640, (2017).

[44] K. Ohira, T. Murayama, H. Yagi, S. Tamura, and S. Arai, "Distributed Reflector Laser Integrated with Active and Passive Grating Sections Using Lateral Quantum Confinement Effect," Japanese Journal of Applied Physics, 42(2), p. 8A, (2003).

[45] G. Liu, G. Zhao, J. Sun, D. Gao, Q. Lu, and W. Guo, "Experimental demonstration of DFB lasers with active distributed reflector," Optics Express, 26(23), pp. 29784–29795, (2018).

[46] G. Zhao, J. Sun, Y. Xi, D. Gao, Q. Lu, and W. Guo, "Design and simulation of two-section DFB lasers with short active-section lengths," Optics Express, 24(10), pp. 10590–10598, (2016).

[47] E. Kanno, K. Takeda, T. Fujii, K. Hasebe, H. Nishi, T. Yamamoto, and Shinji Matsuo, "Twin-mirror membrane distributed-reflector lasers using 20-μm-long active region on Si substrates," Optics Express, 26(2), pp. 1268–1277, (2018).

[48] A. W. Fang, M. N. Sysak, B. R. Koch, R. Jones, E. Lively, Y.-H. Kuo, D. Liang, O. Raday, and John E. Bowers "Single-Wavelength Silicon Evanescent Lasers," IEEE Journal of Selected Topics in Quantum Electronics, 15(3), pp. 535–544, (2009).

[49] G.-H. Duan, C. Jany, A. Le Liepvre, A. Accard, M. Lamponi, D. Make, P. Kaspar, G. Levaufre, N. Girard, F. Lelarge, J.-M. Fedeli, A. Descos, B. Ben Bakir, S. Messaoudene, D. Bordel, S. Menezo, G. de Valicourt, S. Keyvaninia, G. Roelkens, D. Van Thourhout, D. J. Thomson, F. Y. Gardes, and G. T. Reed, "Hybrid III–V on Silicon Lasers for Photonic Integrated Circuits on Silicon," IEEE Journal of Selected Topics in Quantum Electronics, 20(4), p. 6100213, (2014).

[50] S. Yamaoka, N.-P. Diamantopoulos, H. Nishi, R. Nakao, T. Fujii, K. Takeda, T. Hiraki, S. Kanazawa, H. Tanobe, T. Kakitsuka, T. Tsuchizawa, F. Koyama, and S. Matsuo, "239.3-Gbit/s Net rate PAM-4 transmission using directly modulated membrane lasers on high-thermal-conductivity SiC," ECOC post deadline paper, (2019).

4

Electro-absorption modulated DFB laser diodes

In this chapter, we discuss electro-absorption modulation of a heterogeneously integrated III-V-on-Si DFB laser diode to achieve transmission of an 80 Gbps NRZ-OOK signal. The design, static characteristics, small and large signal modulation experiments of the proposed device are reported.

Contents

4.1   Introduction

As data traffic in data centers has reached astronomical proportions, there is undoubtedly a need for efficient and high bandwidth systems [1]. Increasing data rates up to 100 or even 400 Gbps per wavelength are expected in the near future [2]. To achieve that speed, a lot of work has been done on directly and externally modulated laser diodes, on different platforms. In this chapter, we focus on one type of external modulation: electro-absorption modulation (EAM). There have been many demonstrations on different material platforms to achieve high-speed EAMs, as will be outlined throughout the chapter.

In this work, the design and experimental verification of high-speed electro-absorption modulation of a III-V-on-silicon DFB laser diode is shown. This type of laser is sometimes referred to as externally-modulated laser (EML). This modulation technique is only limited by the RC-constant of the modulator, compared to a few factors that limit direct modulation, as previously discussed.

The device under study consists of a standard single-section DFB laser diode, followed by an adiabatic taper [3], which is used as an electro-absorption modulator [4]. These tapers are separated from the main laser section in the same way that the two laser sections were electrically isolated in chapter 3.

In this work, we try to improve the performance of the device reported in [4], by optimizing the structure. This chapter is organized as follows. First, we review the literature, and discuss the state of the art. Next, we discuss the EML structure design. Then, we present the static measurement results of the EML. After that, we show the small signal and large signal modulation results. As mentioned in chapter 2, the device presented in this chapter is based on an InAlGaAs/InP epitaxial layer structure. The SOI was fabricated using e-beam lithography in the cleanroom facilities at Ghent University.

4.2   Literature review and state-of-the-art

There has been much work on high-speed EAMs on different material platforms. For example, a 100 Gbps NRZ GeSi lumped electro-absorption modulator implemented on a silicon photonic platform was shown in [5–6]. The EAM operated at 1600 nm, since it is challenging to have operation at C and O bands, due to bandgap wavelength of Germanium. Also, Germanium is an indirect bandgap material, so it doesn't serve well as an efficient light source.

InP is a good alternative, since it is a direct bandgap material, with many demonstrations at C and O bands. For example, C-band InP-based double-side lumped EML DFB laser shown in 4.1 (a) was demonstrated in [7]. This was used for 2×56 Gbps NRZ signal transmission, as illustrated in Fig. 4.1 (b).

With regards to the III-V-on-silicon platform, some EAMs have been reported for O and C bands [8–9]. These were used to successfully demonstrate 50 Gbps operation on both of them [10]. Fig. 4.2 shows a 100 µm long travelling-wave EAM. The MQW material used in [8–9] is InAlGaAs, which is also the material of choice in this work. As previously mentioned, the reason why this material is superior to InGaAsP is due to the higher conduction band offset. Using InAlGaAs, other demonstrations showing transmission of 56 Gbps NRZ-OOK and 100 Gbps duobinary signals using a lumped EAM were reported in [4, 11].
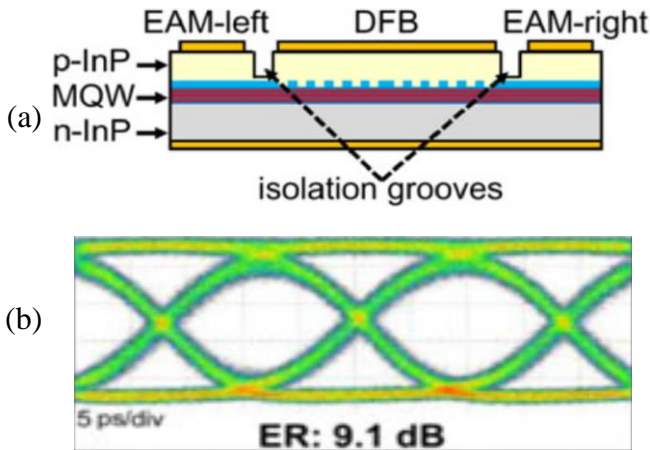
Figure 4.1: (a) Cross section showing a monolithic InP DFB laser with one electro-absorption modulator on each end. **(b)** Eye diagrams at 56 Gbps NRZ signal [7].
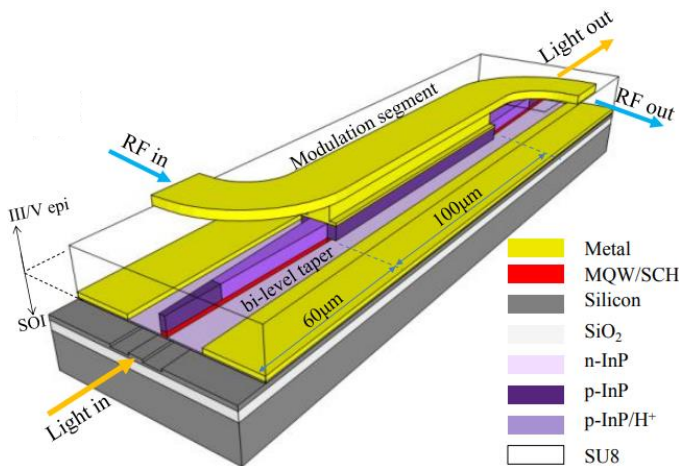

Figure 4.2: 3D view of the hybrid III-V-on-silicon travelling-wave EAM [9].

We have spoken about two different types of EAMs: lumped and travelling-wave (TW) EAMs. The difference lies in the electrode configuration. In a TW modulator, the RF electrical signal travels through a long electrode of a few millimeters (transmission line), in the same direction as the optical signal. The impedance of the modulator should be matched to the impedance of the transmission line (50 Ω) such that there would be maximum power transmission and no reflections. The disadvantage is then the higher power consumption due to the load resistance (50 Ω instead of e.g. 10 Ω), as well as the larger footprint due to the long transmission lines.

On the other hand, lumped modulators have smaller electrodes, and are typically limited by their RC constant. This translates to a bandwidth dependence on the resistance of the modulator and the driver, and on the area of the modulator, as will be explained later in the section. Two advantages of these modulators are the lower power consumption (impedance matching can in principle be done by controlling the driver's impedance), and smaller footprint compared to travelling-wave modulators. This work discusses lumped EAMs, unless stated otherwise.

High modulation bandwidths are also possible using directly modulated DFB laser diodes [12]. However, direct modulation at high frequencies often comes with a large chirp. Electro-absorption modulation suffers less from this problem and its bandwidth is limited only by the RC constant of the modulator. As the junction capacitance decreases with decreasing width and length of the EAM, a shorter and narrower EAM will result in a higher modulation bandwidth. However, a small EAM area would limit the extinction ratio, so a compromise must be sought. Although EAMs are advantageous, they have higher insertion loss compared to directly modulated laser diodes.
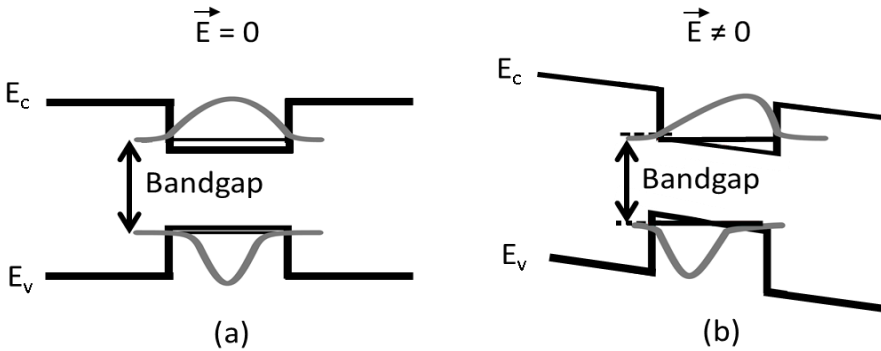

Figure 4.3: (**a**) Applying an electric field to the quantum well results in (**b**) reducing the effective bandgap and shifting the wave function due to the Quantum-confined Stark effect.
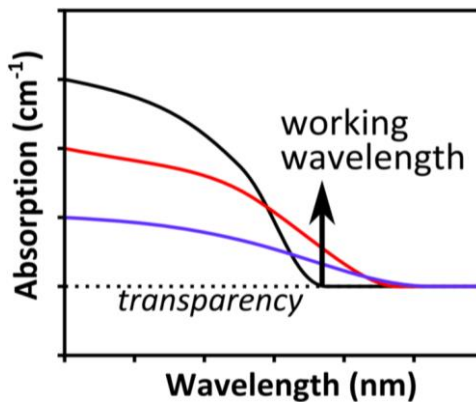

Figure 4.4: The absorption spectrum without applying an electric field (black), and with small and large applied electric fields (blue, red) [13].

The operation of the device can be understood through the quantum-confined Stark effect (QCSE). By applying an electric field, the effective bandgap of the material is reduced, and the wave function is shifted, as illustrated in Fig. 4.3. Reducing the effective bandgap means that electrons in the valence band can absorb photons with a lower energy (higher wavelength) than the bandgap energy, resulting in a shift of the absorption spectrum to higher wavelengths. This is also illustrated in Fig. 4.4, in which the absorption spectrum is shown for different applied electric fields [13]. The black curve shows the absorption spectrum with no applied electric field. The absorption at the working wavelength increases with increasing applied electric field. This is shown in the blue and red curves (small and large applied electric fields), respectively.

The QCSE is intrinsically very fast. What limits the speed of an EAM is the RC constant, where C_{EAM} is the junction capacitance and R_{EAM} is determined by the modulator's series resistance R_{series} and the output impedance of the driver R_{driver}. For example, a shorter modulator has the potential to increase the bandwidth due to the reduced modulator area, and as a result reduced capacitance. The resistance R_{EAM}, capacitance C_{EAM} and 3 dB modulation bandwidth f_{3dB} are given by:

$$R_{EAM} = (R_{driver} + R_{series}) \qquad (4.1)$$

$$f_{3\,dB}^{RC} = \frac{1}{2\,\pi\,R_{EAM}\,C_{EAM}} \qquad (4.2)$$

$$C_{EAM} = \frac{\varepsilon\,A}{d} \qquad (4.3)$$

where ε is the dielectric constant, A is the area of the modulator, and d is the thickness of the active region.

4.3 Design

The 3D, top and side views of the proposed device are shown in Fig. 4.5 (a–c). The adiabatic taper used for light coupling from the III-V waveguide to the silicon waveguide [14] is used as an EAM [4]. The dimensions of the taper are shown in Fig. 4.5 (d). The proposed device is based on that of [4], but with each 180 µm long taper cut in two parts, and modulating only one of them. This is because a shorter modulator would result in a higher bandwidth. As electro-absorption modulation is only limited by the RC constant, structure optimization has the potential to obtain very high modulation bandwidths. To sum up, the proposed device consists of five sections: an active section in the middle, and two EAM sections (EAM$_1$, EAM$_2$) on each side of the cavity.

Since the performance can be affected by the electrical resistance of the imperfect isolation, we decided to increase the length of the isolation etch from 14 µm in the two-section laser diodes and in [3], to 30 µm. Making the isolation

region longer reduces the etching depth required to achieve a certain isolation resistance. As p-InP etching is much faster than p-InGaAs, deep etching to electrically isolate the layers can risk to introduce losses to the optical mode, and consequently runs a risk of low optical output power. To understand more about the benefit of a high electrical isolation resistance, it is useful to examine the equivalent electrical circuit of the proposed device shown in Fig. 4.6. First, the laser diode in series with the laser's series resistance R_{DFB} is the electrical equivalent of the gain section. Second, the electrical isolation resistance $R_{Isolation}$ is the electrical equivalent of the resistance due to p-InGaAs and p-InP etching. Finally, the modulator's capacitance C_{EAM} in series with the modulator's resistance R_{Series} is the electrical equivalent of the modulated taper. The higher $R_{Isolation}$, the lower the leakage current is between the two sections. Low $R_{Isolation}$ leads to modulating the active region along with the EAM, which is not desired. In our case, the resistance between EAM_1 and the active section is 6 kΩ. The isolation resistance of 6 kΩ is less than the one reported in chapter 3 of 13 kΩ because the etching was not at the same depth.

The active laser section is 500 µm long and 2 µm wide. The EAM sections are each 50 µm long. The isolation sections are 30 µm each, with half of the first isolation section being in the taper. This makes the full taper length around 150 µm long. The width of the taper goes from 2 µm down to 0.7 µm. In principle, either of the EAM sections can be used to modulate the light. However, in the first EAM section, the light is confined more to the III-V waveguide, while in the second EAM section the light is confined more to the silicon waveguide. Therefore, more light will be absorbed when reverse biasing the first EAM section, and a higher extinction ratio is expected.

An advantage of this configuration is that when one section is used as an EAM, the other section can be used as an SOA to increase the optical power. Moreover, this configuration allows to perform PAM-4 experiments by modulating both taper sections (EAM_1, EAM_2) if they have similar extinction ratio and modulation bandwidth. Since that is not the case as will be thoroughly explained in the next section, we were unable to perform a PAM-4 experiment.

The InAlGaAs/InP epitaxial layer structure is bonded on a 400 nm thick SOI that has a 500 µm long and 3.5 µm wide DFB grating etched 190 nm deep, with a period of 248 nm and duty cycle of 50%. A quarter-wave phase shift is located in the center of the grating. The silicon chip is made using electron beam lithography at Ghent University. The fabrication procedure used is the standard procedure discussed in chapter 2. However, since the InAlGaAs quantum wells contain aluminum, the surface on the sidewalls oxidizes. This creates trap states and surface recombination. The oxidation is removed by repeated immersion in H_2SO_4:H_2O_2:H_2O (1:1:20) and BHF:H_2O (1:10). After that, the lasers are immediately passivated using low temperature Si_3N_4, high temperature Si_3N_4, and finally BCB. The rest of the fabrication process follows the standard procedure summarized in chapter 2, and detailed in [15–17].
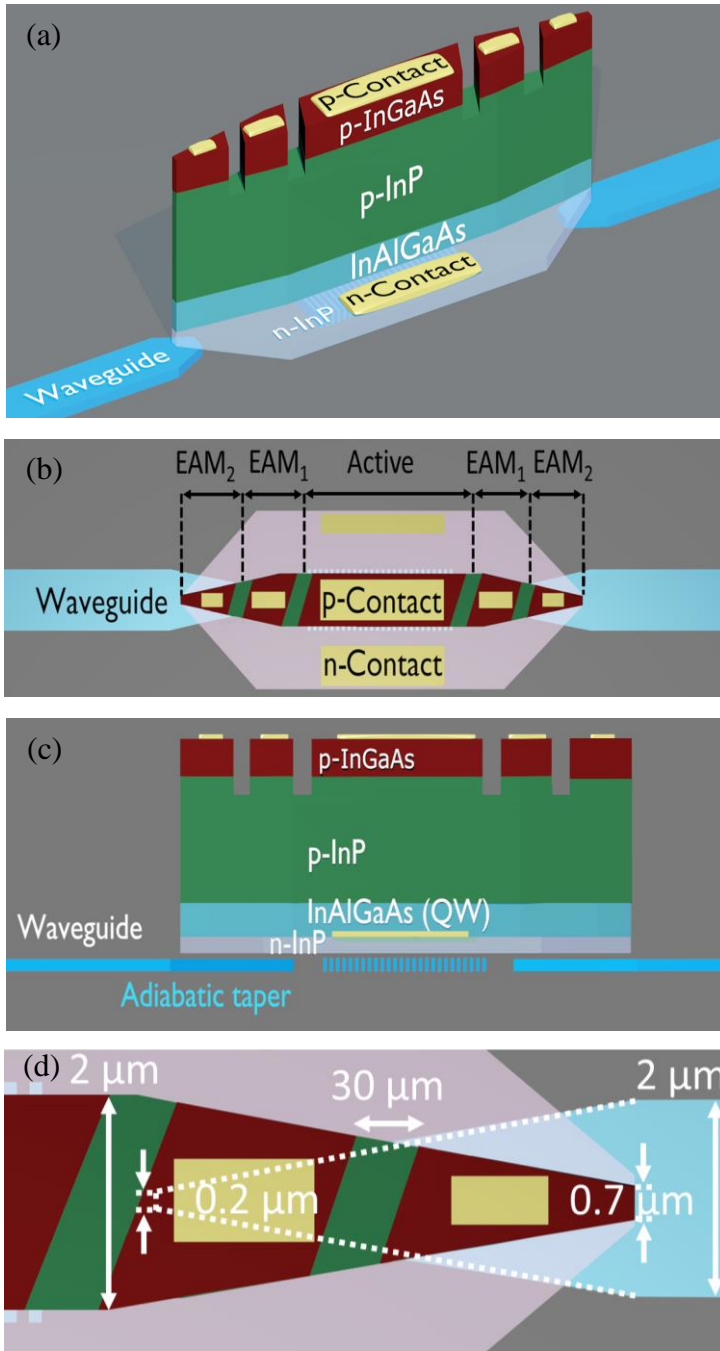
Figure 4.5: (**a**) 3D, (**b**) top and (**c**) side views of the proposed externally-modulated DFB laser diode. Two adiabatic tapers like the one in (**d**) are placed on each end, and cut in two sections to be used as electro-absorption modulators.
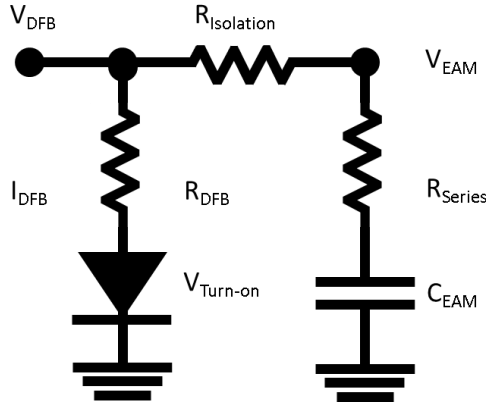
Figure 4.6: The equivalent electrical circuit of the DFB laser and the modulated taper

4.4   Characterization

4.4.1   Static characteristics

The stage temperature (assumed to be close to the sample temperature) is fixed at 15°C. The output light is coupled out of the chip by means of a grating coupler, of which the coupling loss is 6 dB. The grating coupler loss is determined by sending an optical signal at the desired wavelength over a straight waveguide with two grating couplers (input and output grating couplers). The reported optical power P_{out} throughout the chapter is the power in the Si waveguide (i.e. excluding the losses in the grating coupler). The threshold current I_{th} is around 30 mA. The series resistance R_{DFB} of the active section is 7.6 Ω. Fig. 4.7 shows the spectrum for $I_{DFB} = 50$ mA and $V_{EAM} = 0$ V. The lasing peak is at 1570.6 nm with $P_{out} = -4.4$ dBm. To characterize the EAM, I_{DFB} is fixed at 50 mA, and P_{out} is measured at different V_{EAM} of the first taper section as shown in Fig. 4.8 (a, b).
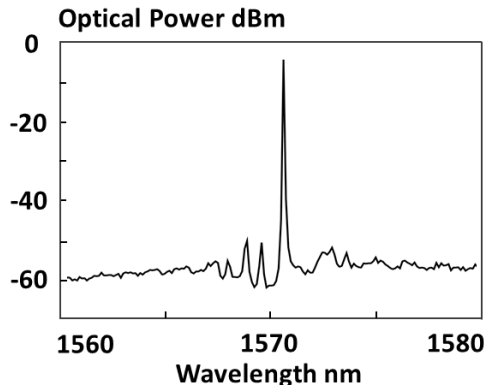

Figure 4.7: The optical spectrum of the laser showing single-mode operation at 1570.6 nm for 50 mA laser bias current (without biasing the modulator).
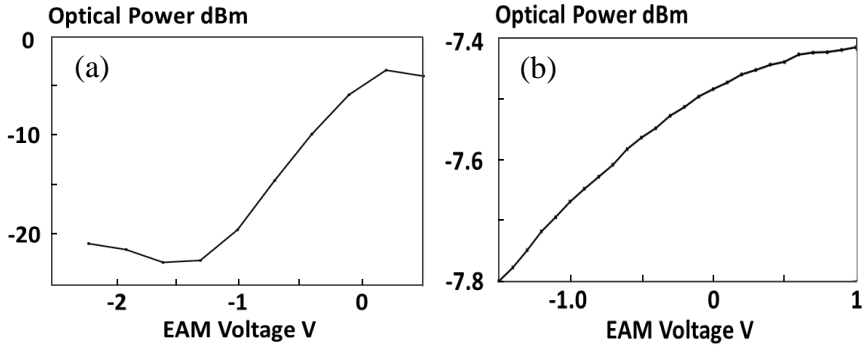
Figure 4.8: Optical output power versus bias voltage of (**a**) the first taper section and (**b**) the second taper section, while the current in the active region is fixed at 50 mA.
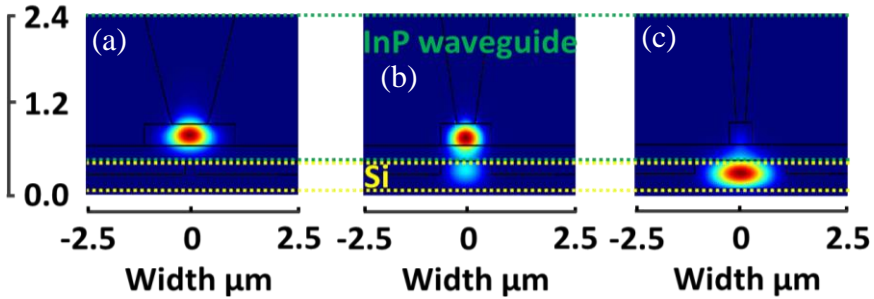

Figure 4.9: The optical mode profiles at (a) the beginning of the taper, (b) middle of the taper, and (c) end of the taper.

One of the reasons to fabricate two taper sections was to perform a PAM-4 experiment, by modulating both tapers. For such an experiment, a similar extinction ratio in both tapers is required. The measured extinction ratio for the first and second section are shown in Fig. 4.8 (a, b). It is around 15 dB for the first taper section, while it is less than 1 dB for the second taper section, when biased between $V_{EAM} = 0$ V and -1 V. This is because the current length of each taper section is around 50% of the total taper length. However, since the optical mode is mostly in the III-V waveguide in the first taper section, and mostly in the silicon waveguide in the second taper section, the extinction ratio is higher for the first section. Fig. 4.9 (a, b, c) show the optical mode profiles at the beginning of the taper (mostly in the III-V waveguide), at the middle of the taper (hybrid mode between the III-V and the silicon waveguides), and at the end of the taper (mostly in the silicon waveguide).

To obtain similar extinction ratios for both sections for the PAM-4 experiment, the first taper section (with high optical confinement in the quantum wells) should be shorter than the second taper section (with low optical confinement in the quantum wells). Based on these findings, the focus in this experiment is on modulating the first EAM section, while not pumping the second EAM section.

4.4.2   Small signal modulation

A small signal modulation experiment is performed using the setup shown in Fig. 4.10. An Agilent N5247A VNA is used to provide electrical signals up to 67 GHz. The signal is superimposed on a negative bias, for reverse biasing the EAM, using a 45 GHz bias tee. The signal is then used to modulate the EAM, while biasing the DFB laser diode at $I_{DFB} = 50$ mA using a Keithley current source. The RF signal is applied using a Cascade Infinity Ground-Signal-Ground (GSG) RF probe with 100 μm pitch. Due to the losses in the optical link (e.g. from the grating couplers), and to accommodate the fact that no transimpedance amplifier was used in the experiment, the signal is boosted using an Optolink L-band EDFA. The output is fed to a Discovery DSC-10H photodetector with a bandwidth of 43 GHz. Finally, the output electrical signal is fed back to the VNA.

Fig. 4.11 shows the small signal modulation response S_{21} of the device. The measured 3 dB modulation bandwidth of the device is around 33 GHz at $I_{DFB} = 55$ mA and $V_{EAM} = -0.8$ V. This is an improvement of around 30% compared to the 25 GHz bandwidth reported in [4]. This improvement is in agreement with what we expected theoretically based on the reduced modulated area of 25% and thus the reduced capacitance as given in (4.2–3).

After the light is modulated in the first taper section, the modulated light passes to the second taper section, which modulates the carriers in the section. We believe the 2 dB low frequency roll-off is due to the limited modulation response of the second taper section. This poor low frequency response is not taken into account in the calculation of the 3 dB bandwidth of the device, as it is straightforward to minimize the spectral content at these low frequencies by reducing the word length. Another solution is to apply 8b/10b line coding. This coding maps 8-bits words to 10-bits symbols, to remove long sequences of 1's and 0's, and to reduce low frequency bandwidth components.
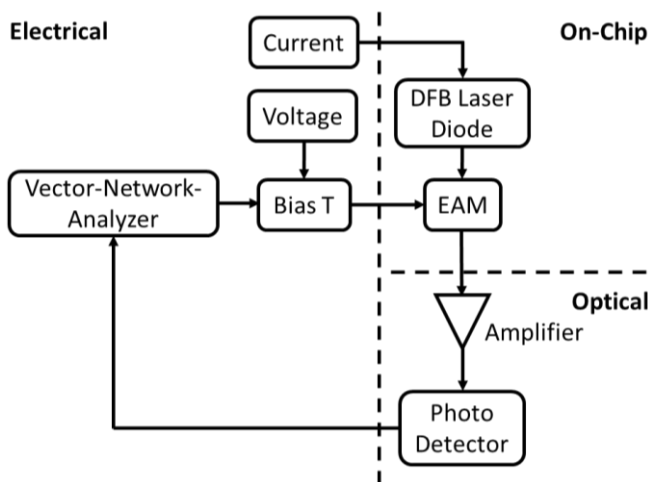

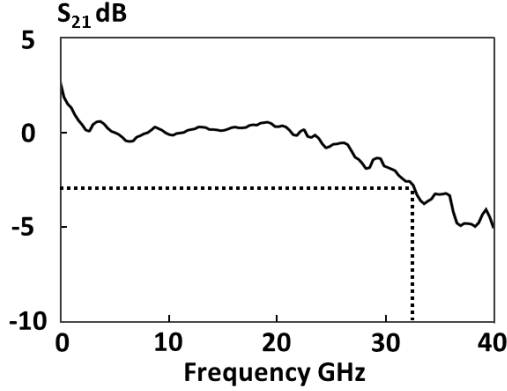**Figure 4.10:** Block diagram of the measurement setup used for small signal modulation

Figure 4.11: Small signal modulation response S_{21} showing nearly 33 GHz 3 dB modulation bandwidth at current of 55 mA and bias voltage of −0.8 V.

The 3 dB modulation bandwidth can be estimated by measuring the input impedance and fitting it to the theoretical one. This is done by first measuring the reflection parameter S_{11} given by (4.4). The modulator is modelled by the electrical equivalent circuit in Fig. 4.12, similar to the models reported in [19–22]. In this model, R_{Series} is the series resistance, C_{EAM} is the junction capacitance, C_P is the parasitic capacitance, L_s and R_s are the inductance and resistance of the metal wires, and G_{EAM} is the conductance that represents the leakage of the junction. Other parameters such the resistance and capacitance of the substrate, or the generated photocurrent in the EAM, are not taken into account. The input impedance Zin is given by (4.5). By fitting the measured impedance to the theoretical one in Fig. 4.13, the following values are obtained: $R_{Series} = 10$ Ω, $C_{EAM} = 46.5$ fF, $C_p = 74.5$ fF, $L_s = 1.43$ nH, $R_s = 66.5$ Ω, $G_{EAM} = 1.4$ mS.

$$S_{11} = \frac{Zin - 50}{Zin + 50} \tag{4.4}$$

$$Z_{in} = \frac{(\frac{G_{EAM}}{j\omega C_{EAM}} + R_{series} + R_s + jwL_s)\,\frac{1}{j\omega C_P}}{\frac{G_{EAM}}{j\omega C_{EAM}} + R_{series} + R_s + jwL_s + \frac{1}{j\omega C_P}} \tag{4.5}$$
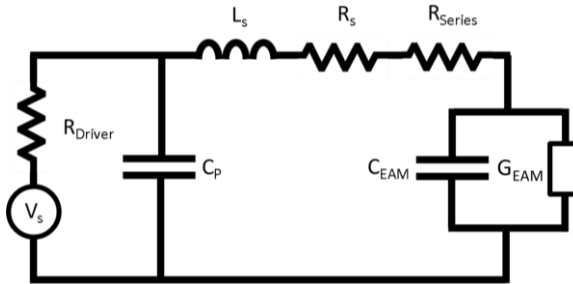

Figure 4.12: The electrical equivalent circuit of the electro-absorption modulator
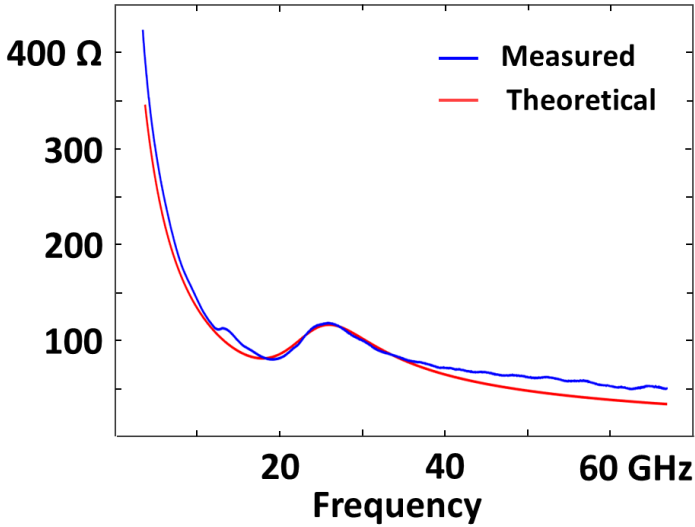
|Input impedance|

Figure 4.13: Fitting the measured input impedance of the electro-absorption modulator to the theoretical one of the electrical equivalent circuit

4.4.3   Large signal modulation

Data transmission experiments were performed on the EML using the setup in Fig. 4.14. An electrical signal is generated with a Keysight M8196A AWG. This electrical signal is amplified by a 50 GHz RF electrical amplifier (SHF-S807). Similarly to the small signal measurement, the data signal is superimposed on a negative bias voltage.
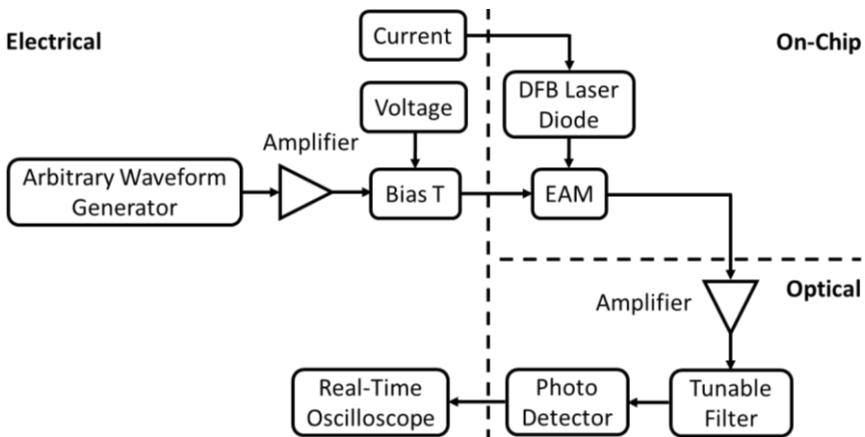

Figure 4.14: Block diagram of the measurement setup used for large signal modulation

An L-band EDFA is used to boost the optical signal. The amplified spontaneous emission is filtered out using a variable-bandwidth optical tunable filter (Santec OTF-350). The bandwidth of the filter was set to 1 nm. The resulting optical signal is fed to the photodetector, and finally, the output electrical signal is fed to a Keysight DSAZ634A Real-Time Oscilloscope.

A raised-cosine filter with a roll-off factor $\alpha = 0.1$ is used to shape the transmitted pulse of the AWG. Using the built-in channel de-embedding function of the AWG, transmission of 50 and 80 Gbps NRZ PRBS with a word length of $2^7 - 1$ was demonstrated, as shown in Fig. 4.15. The eye diagrams for back-to-back configuration, and after transmission over a 2 km long NZ-DSF link are shown in Fig. 4.15 (a, c) and Fig. 4.15 (b, d), respectively. The used Corning fiber had a 5 ps/nm·km dispersion.

The voltage swing applied to the EAM is about 1.8 V_{pp}. The device was operating at $I_{DFB} = 49$ mA and $V_{EAM} = -0.7$ V. The optical bandwidth of the optical tunable filter was 1 nm. The received optical power was 5 dBm (note that no transimpedance amplifier was present at the receiver). The recorded BER was around $1.5 \cdot 10^{-4}$, which is below the KP4-FEC limit of $2.2 \cdot 10^{-4}$.
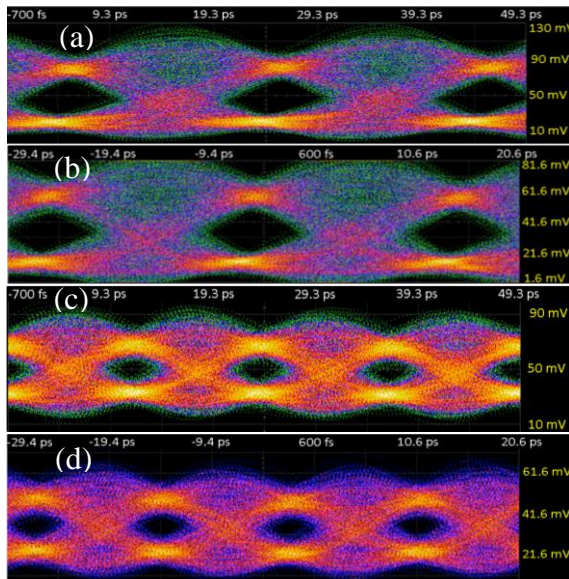

Figure 4.15: Sub-HD-FEC transmission at 50 Gbps and 80 Gbps (**a**, **c**) in the back-to-back configuration, and (**b**, **d**) with a 2 km NZ-DSF link, for a pattern length of $2^7 - 1$.

The measured BER versus received power for this transmitter is shown in Fig. 4.16. To obtain different power levels at the receiver side and their BER, an optical attenuator is placed before the photodetector. 80 Gbps PRBS transmission with a word length of ($2^7 - 1$) and a BER lower than the 7% HD-FEC limit of 3.8 $\cdot 10^{-3}$ is possible for a received power less than 0 dBm. It is observed that

increasing the word length to 2^{15} increases the BER. This can be explained by looking back at the small signal modulation response in Fig. 4.11, in which the low frequency response has a 2 dB roll-off. This low frequency part becomes significant when bit combinations with low frequencies (many consecutive 1's or 0's) become more probable.
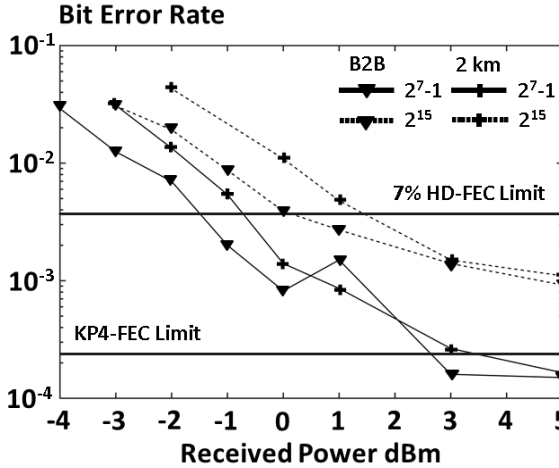

Figure 4.16: Bit-error-rate vs. received power showing sub-HD-FEC operation for 80 Gbps for a received power below 0 dBm.

4.5   Conclusion

We have demonstrated data transmission of an 80 Gbps NRZ-OOK signal, with a 33 GHz modulation bandwidth electro-absorption modulation of III-V-on-Si DFB laser diodes. Both back-to-back configuration and transmission over a 2 km long NZ-DSF link was investigated. BERs below the 7% HD-FEC threshold using feed-forward equalization were demonstrated. Table 4.1 summarizes the performance of the device, compared to other demonstrated electro-absorption modulated laser diodes.

Table 4.1: Comparison between some demonstrations in the literature and this work

	[4]	[5]	[7]	[9]	**This work**
Platform	III-V/Si	GeSi	III-V	III-V/Si	III-V/Si
Modulator type	Lumped	Lumped	Lumped	TW	Lumped
Modulation speed (Gbps)	2×56	100	2×56	50	80
Small signal bandwidth (GHz)	25	>50	35	42	33

In comparison to the other III-V-on-silicon lasers, our lasers had a 3 dB modulation bandwidth of 33 GHz, which is around 30% improvement compared to the 25 GHz bandwidth reported in [4]. The modulation bandwidth is less than the travelling-wave modulator in [9], which is normally longer than a lumped modulator. However, transmission experiment shows that a modulation speed of 80 Gbps is possible.

The performance is similar to the 35 GHz modulation bandwidth reported for the monolithic III-V laser [7], with similar device dimensions. However, the bandwidth of our device falls behind in comparison to the bandwidth of the 50 GHz GeSi EAM demonstrated in [5–6]. On the other hand, the GeSi EAM has a lower static extinction ratio compared to our device (4.8 versus 15 dB).

In general, there is still room for improvement and to obtain a higher modulation bandwidth. This can be done by further optimization of the device dimensions, i.e. attempting to design shorter and/or narrower EAMs. Also, PAM-4 experiments using both tapers can be part of future work.

References

[1] C. Kachris, K. Kanonakis, and I. Tomkos, "Optical Interconnection Networks in Data Centers: Recent Trends and Future Challenges", IEEE Communications Magazine, 51(9), (2013).

[2] D. Cunningham, "Trends in Data Rate and Link Length in Evolving Optical Standards", European conference on optical communication (ECOC), WS4 - Technologies for Short Reach Optical Interconnects, (2013).

[3] A. Abbasi, B. Moeneclaey, J. Verbist, X. Yin, J. Bauwelinck, G.-H. Duan, G. Roelkens, G. Morthier, "Direct and electro-absorption modulation of a III-V-on-silicon DFB laser at 56 Gbps," IEEE Journal of Selected Topics in Quantum Electronics, 23(6), p. 1501307, (2017).

[4] A. Abbasi, L. Abdollahi Shiramin, B. Moeneclaey, J. Verbist, X. Yin, J. Bauwelinck, D. Van Thourhout, G. Roelkens, G. Morthier, "III-V-on-Silicon C-band High-Speed Electro-Absorption Modulated DFB Laser," Journal of Lightwave Technology, 36(2), pp.252–257, (2018).

[5] J. Verbist, M. Verplaetse, A. Srinivasan, J. Van Kerrebroeck, P. De Heyn, P. Absil, T. De Keulenaer, R. Pierco, A. Vyncke, G. Torfs, X. Yin, G. Roelkens, J. Van Campenhout, J. Bauwelinck, "Real-time 100 Gb/s NRZ and EDB transmission with a GeSi electro-absorption modulator for short-reach optical interconnects," Journal of Lightwave Technology, 36(1), p.90–96, (2018).

[6] A. Srinivasan, M. Pantouvaki, S. Gupta, H. Chen, P. Verheyen, G. lepage, G. Roelkens, K. Saraswat, D. Van Thourhout, P. Absil, J. Van Campenhout, "56Gb/s Germanium Waveguide Electro-Absorption Modulator," Journal of Lightwave Technology, 34(2), pp.419–424, (2016).

[7] M. Theurer, H. Zhang, Y. Wang, W. Chen, L. Chen, Zeng, U. Troppenz, G. Przyrembel, A. Sigmund, M. Moehrle, and M. Schell, "2 × 56 GB/s From a Double Side Electroabsorption Modulated DFB Laser and Application in Novel Optical PAM4 Generation," Journal of lightwave technology, 35(4), pp. 706–710, (2017).

[8] Y. Tang, J. D. Peters, and J. E. Bowers, "Over 67 GHz bandwidth hybrid silicon electroabsorption modulator with asymmetric segmented electrode for 1.3 µm transmission," Optics Express, 20(10), pp. 11529–11535, (2012).

[9] Y. Tang, H.-W. Chen, S. Jain, J. D. Peters, U. Westergren, and J. E. Bowers, "50 Gb/s hybrid silicon traveling-wave electroabsorption modulator," Opt. Express, 19(7), pp. 5811–5816, (2011).

[10] T. Ferrotti, "Design, fabrication and characterization of a hybrid III-V on silicon transmitter for high-speed communications," PhD thesis, (2016).

[11] A. Abbasi, J. Verbist, L. Abdollahi Shiramin, M. Verplaetse, T. De Keulenaer, R. Vaernewyck, R. Pierco, A. Vyncke, X. Yin, G. Torfs, G. Morthier, J. Bauwelinck, G. Roelkens, "100-Gb/s Electro-Absorptive Duobinary Modulation of an InP-on-Si DFB Laser," IEEE Photonics Technology Letters, 30(12), pp. 1095–1098, (2018).

[12] Y. Matsui, R. Schatz, T. Pham, W. A. Ling, G. Carey, H. M. Daghighian, D. Adams, T. Sudo, and C. Roxlo, "55 GHz Bandwidth Distributed Reflector Laser," Journal of Lightwave Technology, 35(3), pp. 397–403, (2017).

[13] M. Tassaert, "Leveraging High Index Contrast in the III-V Waveguide Platform on Silicon-on-Insulator for Optical Signal Processing Applications," PhD thesis, (2014).

[14] M. Lamponi, S. Keyvaninia, C. Jany, F. Poingt, F. Lelarge, G. de Valicourt, G. Roelkens, D. Van Thourhout, S. Messaoudene, J. –M. Fedeli, and G. H. Duan, "Low-Threshold Heterogeneously Integrated InP/SOI Lasers With a Double Adiabatic Taper Coupler," IEEE Photonics Technology Letters, 24(1), pp. 76–78, (2012).

[15] G. Roelkens, A. Abbasi, P. Cardile, U.D. Dave, A. De Groote, Y. De Koninck, S. Dhoore, X. Fu, A. Gassenq, N. Hattasan, Q. Huang, S. Kumari, S. Keyvaninia, B. Kuyken, L. Li, P. Mechet, M. Muneeb, D. Sanchez, H. Shao, T. Spuesens, A. Subramanian, S. Uvin, M. Tassaert, K. Van Gasse, J. Verbist, R. Wang, Z. Wang, J. Zhang, J. Van Campenhout, Y. Xin, J. Bauwelinck, G. Morthier, R. Baets, D. Van Thourhout, "III-V-on-Silicon Photonic Devices for Optical Communication and Sensing," Photonics (3), pp. 969–1004, (2015).

[16] A. Abbasi, "High speed directly modulated III-V-on-Silicon DFB lasers," PhD thesis, (2016).

[17] S. Dhoore, "Heterogeneously Integrated III-V-on-Silicon Wavelength-Tunable DFB and DBR Lasers," PhD thesis, (2018).

[18] M. Lamponi, "Hybrid III-V on silicon lasers for telecommunication applications," PhD thesis, (2012).

[19] G. L. Li, P. K. L. Yu, W. S. C. Chang, K. K. Loi, C. K. Sun, and S. A. Pappert, "Concise RF equivalent circuit model for electroabsorption modulators," Electronics Letters, 36(9), pp. 818–820, (2000).

[20] Y. Chiu, S. Z. Zhang, V. Kaman, J. Piprek, J. Edward Bowers, "High-speed traveling-wave electro-absorption modulators," Proceedings SPIE 4490, Multifrequency Electronic/Photonic Devices and Systems for Dual-Use Applications, (2001).

[21] H. Wang, R. Zhang, D. Lu, C. Ji, "Simulation and experiment of 1310nm high speed InGaAsP/InP EAM," Proceedings SPIE 9270, Optoelectronic Devices and Integration V, 927005 (2014).

[22] H. Ramon, J. Lambrecht, J. Verbist, M. Vanhoecke, S. A. Srinivasan, P. De Heyn, J. Van Campenhout, P. Ossieur, X. Yin, J. Bauwelinck, "70 Gb/s Low-Power DC-Coupled NRZ Differential Electro-Absorption Modulator Driver in 55 nm SiGe BiCMOS," Journal of lightwave technology, 37(5), (2019).

5

Compact DFB laser diodes

Contents

5.1 Introduction

A lot of work has been done, including the devices demonstrated throughout this work, to enhance the bandwidth and modulation speed of InP-on-silicon DFB laser diodes. In some recent work, the modulation speed demonstrated was 56 Gbps for direct modulation [1], and 2 x 56 Gbps using electro-absorption modulation of both tapers individually [2]. The tapers demonstrated are adiabatic, and are typically 230 μm long. In chapter 4, we separated the tapers into two sections, and modulated only one section, in comparison to modulating the full section in [2]. Since the section was shorter, the capacitance was decreased, leading to an increase of the modulation bandwidth and speed.

To improve the results further, the modulated section should be as short as possible. However, these tapers must be long enough to ensure efficient light coupling from the III-V to the silicon waveguide. One can think of making one of the two taper sections very short to improve the modulation bandwidth further. The issue then is that the extinction ratio would drop. To solve these issues, a new taper design must be considered.

Other than improving the modulation bandwidth and speed, it is important to design lasers with a small footprint and low power consumption. In the current lasers, the DFB grating length is typically 300 μm, with a taper length of 230 μm on each end. This makes the total length of the device around 800 μm. In this chapter, we aim to minimize the footprint to reduce the power consumption and to demonstrate compact laser diodes. This is done by a one-stage taper of both the III-V and the silicon waveguides, as shown in [3]. This allows shrinking the length of the taper to less than 60 μm, which is around 4 times shorter than the current design. As a result, the footprint of the device is around 2 times smaller. Since the tapers are short, using them for electro-absorption modulation could result in higher modulation bandwidth than the one demonstrated in chapter 4. The epitaxial structure used for this device is based on an InAlGaAs active region. It has 10 quantum wells instead of 8 quantum wells in chapter 4, since it was optimized for high speed performance. However, the focus in this chapter is rather on the taper design, fabrication and characterization, as we do not cover the high speed performance.

In this chapter, we demonstrate compact InP-on-silicon DFB laser diodes. First, we will show the design parameters used to achieve good coupling. Then, we will show simulations for different taper lengths. Finally, we will show the static characteristics of the fabricated laser devices.

5.2   Design and fabrication

The design of the taper is based on [3], in which a taper as short as 40 μm shows around 95% of the light coupling from the III-V to the silicon waveguide. The design shows a silicon taper with a waveguide width varying between 4 μm and 500 nm, sitting below a III-V taper with a width varying between 3 μm and 150 nm, as shown in Fig. 5.1 [3]. Fig. 5.2 shows the coupling efficiency versus taper length, for three different silicon waveguide thicknesses: 400, 300 and 220 nm. This shows that a taper length of 40 μm should be sufficient to couple the light for all the different waveguide thicknesses.
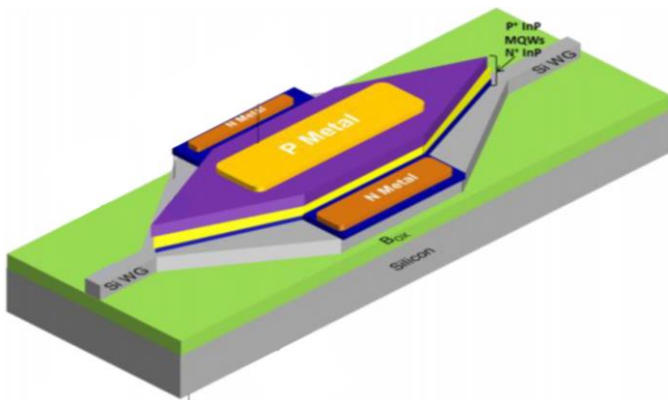

Figure 5.1: 3D schematic of the III-V-on-silicon laser with single-stage taper structure [3]
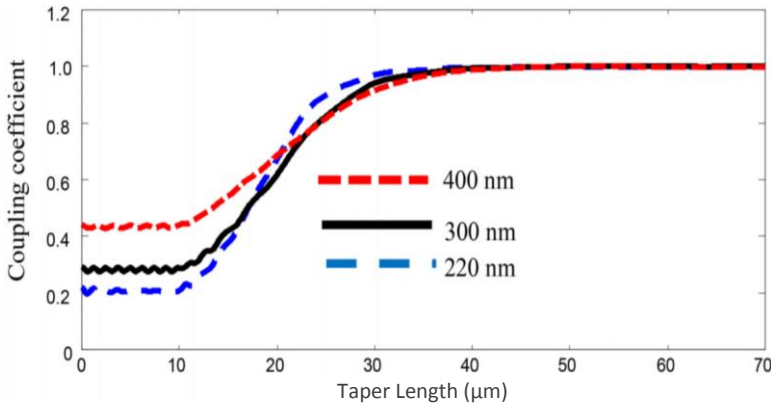
Figure 5.2: Coupling efficiency versus taper length from the III-V to the silicon waveguide for different waveguide thicknesses [3]

The challenging part in the design in [3] is to make a III-V taper tip of 150 nm since this requires e-beam lithography. To relax this requirement, and to make the fabrication possible with UV lithography tools, we designed the III-V taper tip to be 550 nm wide. As discussed earlier, the V-shape of the mesa causes the mesa width at the bottom to be smaller than on the top. In the case of the 500 nm wide tip on the top, the mesa width at the bottom would be around 150 nm, which is already challenging to fabricate.

The 3D view of the laser structure with the single-stage taper design is shown in Fig. 5.3. The laser cavity consists of a DFB grating of 300 μm and two single-stage taper structures at both ends.
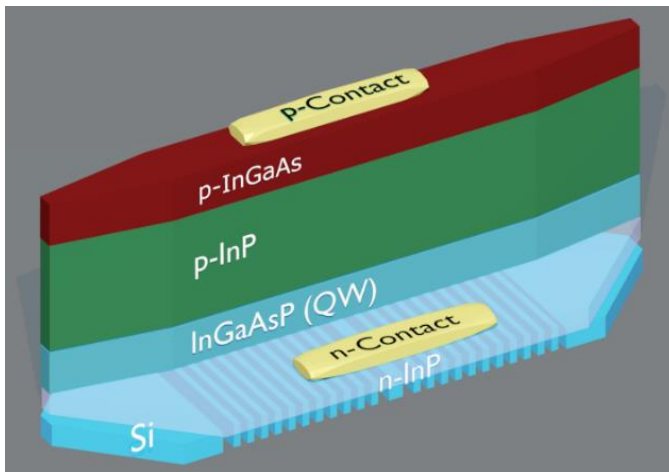

Figure 5.3: 3D schematic of the fabricated compact DFB laser diode

A 3D FDTD simulation using Lumerical showing a sweep of different taper lengths (20, 40, 60 µm) versus the power transmission from the III-V waveguide to the underlying silicon waveguide is shown in Fig. 5.4. In the same figure, the reflection back into the III-V waveguide is also shown. A taper tip with a width of 500 nm is assumed during the simulation, as well as a V-shape mesa. The performance of the 150 µm long traditional adiabatic taper used in chapter 4 is also compared. The simulations are done for two cases: (1) perfect alignment (i.e. the III-V mesa sits exactly in the center of the silicon waveguide below), and (2) assuming a 300 nm misalignment.
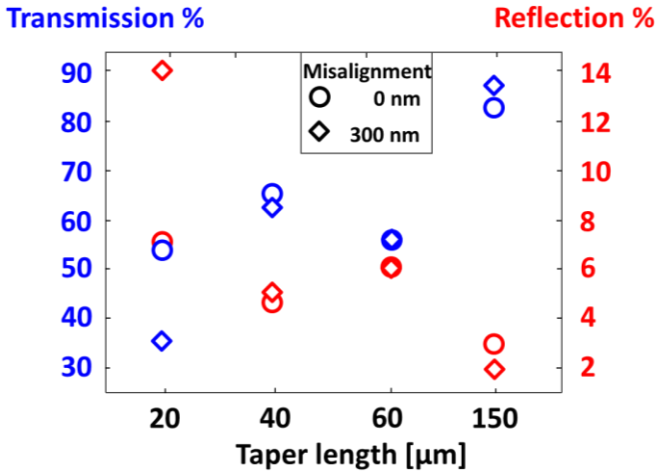

Figure 5.4: 3D FDTD simulations showing the transmission to the silicon waveguide and the reflection back into the III-V waveguide, with different taper lengths (20, 40, and 60 µm), in comparison to the traditional 150 µm long adiabatic taper, with perfect alignment and with 300 nm misalignment

It is shown in the simulations that the traditional 150 µm long taper has a significantly higher transmission (nearly 80% versus 60%) and lower reflection (nearly 3% versus 6%) than the shorter taper structure.

Ideally, a perfect alignment of the III-V mesa structure on top of the silicon is desired. However, during the mesa definition lithography, a misalignment of 200 – 300 nm is expected. Fig. 5.5 (a–b) show how the mesa would be located with respect to the silicon waveguide in case of (a) perfect alignment versus (b) with a 300 nm misalignment. Since the taper tip width is comparable to the silicon waveguide width, around half of the taper's tip will not be on top of the silicon waveguide. Since the coupling region is very short, misalignment is expected to decrease the coupling. This is also predicted by the simulation in Fig. 5.4.

Finally, Fig. 5.6 (a, b) shows a comparison between the dimensions of both the previous (long) taper design used in chapter 3, chapter 4, and in [1], and the proposed (short) taper design.
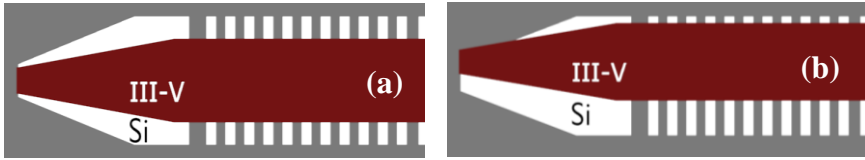
Figure 5.5: Top view with (**a**) a perfect alignment versus (**b**) a 300 nm misalignment illustrating the criticality of misalignment
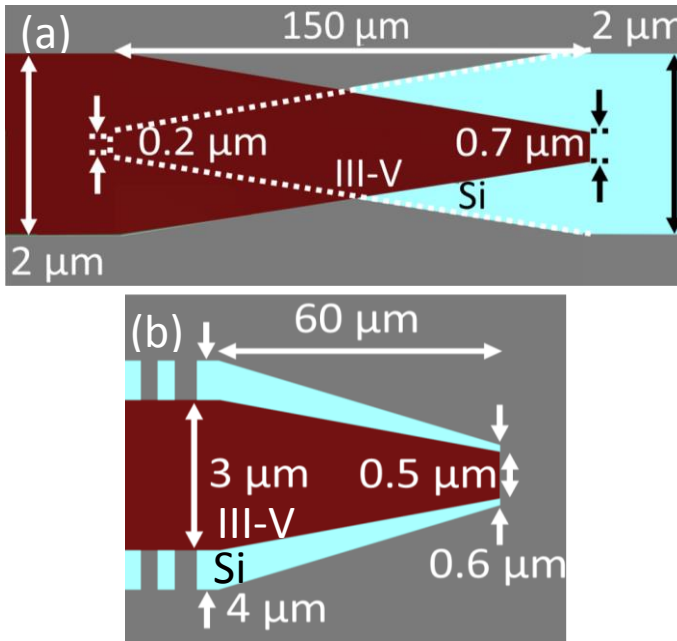

Figure 5.6: A comparison between (**a**) the previous (long) taper design in [1] and (**b**) the proposed (short) taper design.

5.3   Static laser characteristics

The optical output power in the waveguide versus the bias current for different taper lengths (60, 40, and 20 µm) is shown in Fig. 5.7. Initially, we expect the laser with a long taper to have higher power levels than the laser with a short taper. However, we notice that the lasers with a 60 µm long taper have a lower optical output power than the lasers with a 20 µm long taper. The optical output power can also change depending on the quality of the tapers and the fabrication variations from one device to another. A misalignment of around 100 nm for the device with a 60 µm long taper is shown in SEM image in Fig. 5.8, which is better than the typical misalignment for our devices (200 − 300 nm). As suggested earlier by the simulations, even with a considerably good misalignment of 100 nm, the device still have a poor optical output power.
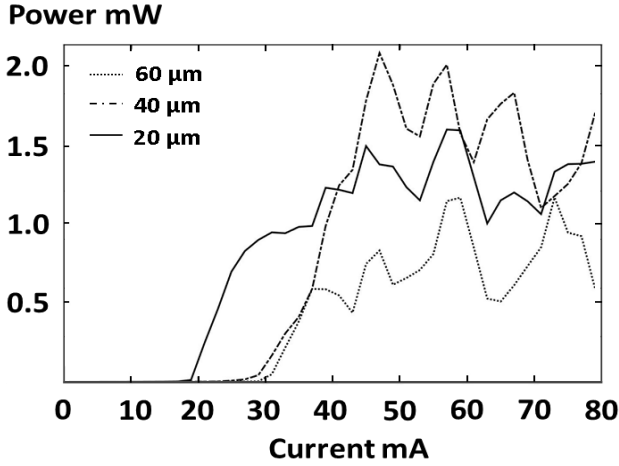
Power mW

Figure 5.7: Optical output power (in the waveguide) versus bias current for the fabricated lasers with 60, 40 and 20 µm taper lengths
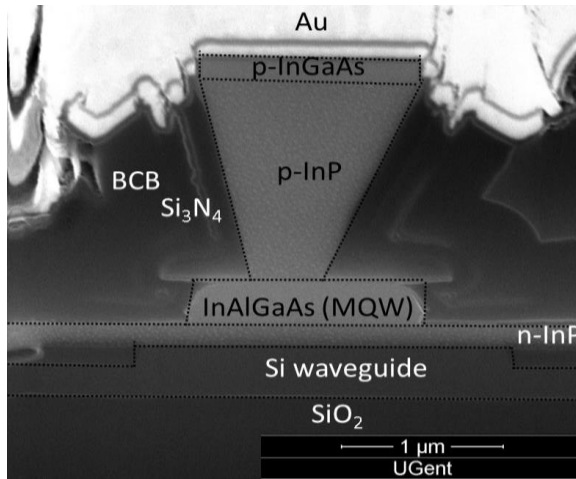

Figure 5.8: SEM image of the cross section of the fabricated device obtained using FIB, showing a misalignment of around 100 nm between the III-V and the silicon waveguide.

The maximum optical output power in the waveguide is around 2 mW as shown in Fig. 5.7, compared to e.g. 6 mW reported in [1] for a standard single-section DFB laser with a 230 µm long taper. The lower optical output power was anticipated in the simulation results in Fig. 5.4. It can also be attributed to the high series resistance of around 25 Ω, compared to e.g. 10 Ω in chapter 3 or 8 Ω in chapter 4. This is suspected to create more heating, which reduces the optical output power. There are two reasons for the higher series resistance: (1) the lower p-InP doping concentration (here $1.0 \cdot 10^{18}$ cm^{-3} -> $1.5 \cdot 10^{18}$ cm^{-3} versus $0.5 \cdot 10^{18}$ cm^{-3} -> $1.0 \cdot 10^{18}$ cm^{-3} in the one of chapter 4), and (2) the thinner n-type InP (150 nm versus 200 nm in the one of chapter 4).

It appears that the lower optical output power is not the only concern. The device also exhibits a multi-mode behavior as shown in Fig. 5.9, which can be a result of the reflections, as anticipated by Fig. 5.4, on top of the 4% reflections from the grating couplers [1].
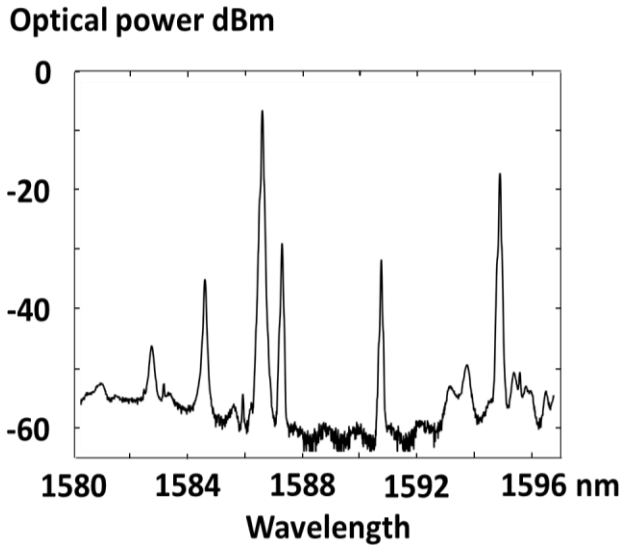

Figure 5.9: Optical spectrum showing a multimode behavior, likely due to the reflections caused by the taper structure, in addition to the reflections from the grating couplers.

5.4   Conclusion

Compact InP-on-Si DFB laser diodes were demonstrated. The lasers are around 400 μm long, which is half the footprint of the previously demonstrated lasers. This is achieved by a single-stage taper which is 60 μm long. The optical output power in the silicon waveguide is 1 mW, which is lower than in the previously demonstrated lasers. Using e-beam for the patterning of the laser structure could allow smaller width of the taper tip, which could improve the optical output power.

References

[1] A. Abbasi, B. Moeneclaey, J. Verbist, X. Yin, J. Bauwelinck, G.-H. Duan, G. Roelkens, G. Morthier, "Direct and electro-absorption modulation of a III-V-on-silicon DFB laser at 56 Gbps," IEEE Journal of Selected Topics in Quantum Electronics, 23(6), p. 1501307, (2017).

[2] A. Abbasi, L. Abdollahi Shiramin, B. Moeneclaey, J. Verbist, X. Yin, J. Bauwelinck, D. Van Thourhout, G. Roelkens, G. Morthier, "2x56 Gbps Electroabsorption Modulated III-V-on-silicon DFB Laser," European Conference on Optical Communication (ECOC), p. M.2.C.3, (2017).

[3] J. Pu, V. Krishnamurthy, D. K. Ting Ng, K. P. Lim, C-W Lee, K. Tang, A. Y. S. Kay, T-H Loh, F. Tjiptoharsono, and Q. Wang, "Heterogeneous Integrated III–V Laser on Thin SOI With Single-Stage Adiabatic Coupler: Device Realization and Performance Analysis," IEEE Journal of Selected Topics in Quantum Electronic 21(6), p. 1501808 (2015).

6

Conclusion and prospects

6.1 Conclusion

Throughout this thesis, we have demonstrated novel heterogeneously integrated III-V-on-silicon DFB lasers. We started by putting this work in context, and showing the advantages of optical interconnects over electrical interconnects. We showed the significance of silicon photonics and consequently heterogeneous III-V-on-silicon integration. We also introduced modulation schemes and techniques.

Next, we provided an overview of the theory of lasers, focusing on DFB laser diodes. Advantages and disadvantages of monolithic III-V and heterogeneous III-V-on-silicon integration were outlined. The fabrication process was briefly introduced, with mentioning the fabrication challenges. The adiabatic taper structure used for all the devices for coupling light from the III-V to the silicon waveguide was introduced.

After that, two-section DFB laser diodes were used for three different purposes. These were self-pulsating DFB lasers, bandwidth-enhanced lasers, and power-efficient lasers. Firstly, self-pulsating DFB lasers with tunable repetition frequencies between 12 and 40 GHz, and narrow RF spectral linewidth of 0.1 Hz under locking were reported. These are useful for the generation of optical microwave carriers for radio-over-fiber applications. Secondly, the same structure with different bias currents was also used to enhance the bandwidth, in comparison to that of an equivalent standard single-section DFB laser. A modulation bandwidth of 25 GHz was achieved, which led to a modulation speed of 45 Gbps NRZ-OOK. Thirdly, a similar two-section laser configuration was used for DFB lasers with record low threshold current of 4.5 mA.

Next, an externally modulated single-section DFB laser was demonstrated. The adiabatic tapers were cut into two sections, and only one section was used as an electro-absorption modulator. This results in a smaller modulator area than the

previous design, which increases the modulation bandwidth and speed. A modulation bandwidth of 33 GHz and a speed of 80 Gbps NRZ-OOK were demonstrated.

Finally, a compact DFB laser structure was demonstrated, using an alternative short taper design. The tapers was shrunk from 230 to 60 μm each. Since the DFB section is typically around 300 μm, the total device length was reduced from 760 to 420 μm. In addition to the small footprint, this taper helps to reduce the power consumption in the laser diode. Finally, fabrication challenges and limitations were discussed.

6.2 Prospects

In this section, suggestions to improve the performance of the different reported devices are given as follows.

6.2.1   Self-heating

As mentioned in chapter 2, the effect of heating is evident in our laser diodes at high bias currents, especially in short lasers. Heating gives the electrons the energy to escape the quantum wells and it also broadens the gain spectrum and reduces therefore the peak gain, which limits the maximum output optical power. This is attributed to the 2 μm thick buried oxide layer which traps the heat and prevents efficient heat sinking to the substrate. A solution could be to optimize the MQW to have a higher conduction band offset, such that the temperature stability is higher. Improving the laser efficiency would also reduce the heating effect. Finally, bonding the entire InP-on-silicon laser p-side down on a heat spreader could also help in heat sinking.

6.2.2   III-V-on-silicon laser / photodetector (transceiver)

In chapter 4, we demonstrated an EML with modulation speed of 80 Gbps NRZ-OOK by using one of the taper sections as an EAM. In principle, the taper could also be used as a photodetector. Therefore it is possible to fabricate a transceiver, by using, e.g. the right taper as a modulator, while at the same time using the left taper as a detector [1].

6.2.3   Ultra-high modulation speed beyond 80 Gbps

The modulation bandwidth can be increased by fabricating a shorter modulator. However, the extinction ratio would decrease. Therefore a compromise must be sought. Moreover, performing a PAM-4 experiment on the EML in chapter 4 would double the achieved bitrate of the laser. For that, the extinction ratio of both taper sections should be similar. This was not the case here, because the optical mode was mainly in the III-V waveguide in the first taper section, and in the silicon waveguide in the second taper section. An improvement would be to decrease the length of the first taper section, and increase the length of the second taper section. This would decrease the extinction ratio in the first taper section,

and increase it in the second. However, this will also decrease the bandwidth of the second taper section. Therefore, a compromise must be sought.

Reference

[1] B. Schrenk, and F. Karinou, "Simple laser transmitter pair as polarization independent coherent homodyne detector," Optics Express, 27(10), pp. 13942–13950, (2019).